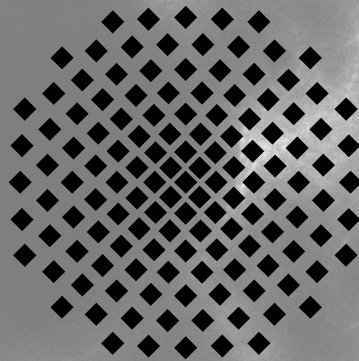


University of Stuttgart
Physics Department
1. Physikalisches Institut

Master's Thesis

**Size and temporal distributions in
nanoscale magnetic materials via
advanced extraction methods**



Udo Höfel

9th April 2015

1st supervisor: Professor Doctor Dressel
2nd supervisor: Professor Doctor Michler
advisor: Doctor Bogani

*Now to other things!
And I'll begin to treat by what decree
Of nature it came to pass that iron can be
By that Stone drawn which Greeks the magnet call
After the country's name (its origin
Being in country of Magnesian folk).
This Stone men marvel at; and sure it oft
Maketh a chain of rings, depending, lo,
From off itself! Nay, thou mayest see at times
Five or yet more in order dangling down
And swaying in the delicate winds, whilst one
Depends from other, cleaving to under-side,
And ilk one feels the Stone's own power and bonds—
So over-masteringly its power flows down.*

Lucretius, De Rerum Natura, Book VI



Zusammenfassung

MAGNETISCHE NANOPARTIKEL besitzen einen Durchmesser, welcher unter 100 nm liegt und die Fabrikation entsprechend anspruchsvoll gestaltet. Trotz der damit einhergehenden Herausforderungen gelang es in den letzten Jahren die Herstellungsmethoden soweit zu verbessern, dass sich die magnetischen Eigenschaften wie auch die chemische Zusammensetzung anwendungsspezifisch maßschneidern lassen.

Für einen effektiven Einsatz in einer Vielzahl von Anwendungsgebieten sind magnetische Nanopartikel ideal geeignet, beispielsweise in der Hyperthermiekrebsbehandlung, die bei Mäusen eine Überlebensrate von bis zu 90 % erzielt, oder als magnetisch leicht trennbare Katalysatoren, die aufgrund des hohen Oberflächen-Volumen-Verhältnisses sehr effizient sind. Des Weiteren wird erwartet, dass die Datenspeicherdichte mittels magnetischer Nanopartikel auf einige Terabit pro Quadratmeter erhöht werden kann. Ein weiterer Bereich in dem magnetische Nanopartikel von eminenter Bedeutung sind, ist die Grundlagenforschung, in welcher sie zum Verständnis magnetischer Mechanismen beitragen. Ferner können Phänomene, wie beispielsweise Superparamagnetismus, die erst unterhalb einer bestimmten Maximalgröße auftreten, ihrerseits wieder technologischen Nutzen besitzen. Aus diesen Gründen wurden und werden weltweit zahlreiche Herstellungsmethoden für Nanopartikel untersucht und die Produktionsparameter, die eine feinere Justage der Eigenschaften der resultierenden Nanopartikel ermöglichen, analysiert.

Eine ökonomische wie auch ökologische Herstellungsmethode ist durch die Laserablationssynthese in Lösung (LASiS) gegeben. Mit dieser Verfahrensweise erzeugte Nitinolnanopartikel sind von hohem Interesse, da Nitinol (NiTi) über etliche außergewöhnliche Eigenschaften, wie zum Beispiel ein Formgedächtnis, einen hohen Widerstand gegen Materialermüdung und eine gewisse Biokompatibilität verfügt. Darum wird in der vorliegenden Arbeit eine ausführliche magnetische Charakterisierung (die feldabhängige Magnetisierungs-, zero field cooling - field cooling- und ac-Messungen umfasst) dieser Nanopartikel vorgenommen, die es erleichtern soll entsprechende Nanopartikel mit aufgabenspezifischen Eigenschaften



zu produzieren. Des Weiteren wurde analysiert, wie sich der Einfluss der eingesetzten Mutterlösung und die eingestellte Laserleistung während des Herstellungsprozesses auf die magnetischen Eigenschaften von Nitinolnanopartikeln auswirken. Der Einfluss der Laserleistung wurde zusätzlich an Eisennanopartikeln untersucht. Dadurch wurden einige der Einstellmöglichkeiten mit deren Hilfe sich die Eigenschaften der Nanopartikel regulieren lassen, besser verstanden und somit eine gezieltere Parameterwahl bei der Herstellung ermöglicht wird, wodurch das Optimierungspotential besser ausgeschöpft werden kann.

Unter den mannigfaltigen weiteren Herstellungsmethoden, welche heutzutage die Produktion von Nanopartikeln mit anwendungsspezifischen magnetischen Eigenschaften beziehungsweise chemischer Zusammensetzung erlauben, findet sich auch der Sol-Gel-Tauchbeschichtungsprozess, mit welchem sich in Siliciumdioxid eingebettete CoNi-Nanopartikel herstellen lassen. Diese weisen bei Bestrahlung mit Laserlicht eine wellenlängenabhängige Koerzitivität auf [1]. Um dieses besondere Phänomen zu beschreiben und zu simulieren, wurde ein erweitertes, einzeldomänenferromagnetisches STONER-WOHLFARTH-Modell in *Mathematica* implementiert. Dabei wird die Möglichkeit genutzt, nicht alle möglichen Winkel θ zwischen der leichten Richtung und dem extern angelegten Feld zuzulassen. Darüber hinaus wird ein teilchengrößenverteilungsabhängiges Modell für superparamagnetische, feldabhängige Magnetisierungsmessungen diskutiert und seine Implementation in *Mathematica* dokumentiert.

In den gebräuchlichen Magnetismusmodellen sind anspruchsvolle Parameter die den Magnetismus beeinflussen, wie beispielsweise die Form der Nanopartikel, noch nicht implementiert. Da es einen Mangel an frei und online verfügbaren Implementierungen von Magnetismusmodellen gibt, vermögen die während dieser Arbeit entwickelten Modelle als Ausgangspunkt für weitere Entwicklungen zu dienen.

Preface

*T*O SUPPORT the open data movement raw data is embedded in the pdf whenever possible and can be saved to a location of your choice by clicking on the  symbol. The embedded data is licensed under the Creative Commons Attribution 4.0 International Public License¹. Be aware that this may not work with old pdf readers, Adobe reader XI or SumatraPDF 2.5.2 or newer should be sufficient. Note that all lines in graphs in this thesis serve merely as guide to the eyes, except otherwise stated.

All graphics have been generated using `gnuplot` and/or `TikZ`. The bibliographic data has been tried to be as extensive as possible. Variables have been defined in the list of symbols. This file has been compiled with `LuaTeX`.

Rommelshausen, 9th April 2015

UDO HÖFEL

¹ Full text of the license can be found at the Creative Commons website.



Contents

List of symbols	11
List of abbreviations	21
1. Introduction and motivation	23
2. Fundamentals of nanoparticles	27
2.1. Fabrication methods	27
2.1.1. Laser ablation synthesis in solution	27
2.1.2. Sol-gel dip-coating	31
2.2. Structural and magnetic properties	33
2.3. Magnetic characterization methods	36
2.4. Applications	39
3. Measurement techniques	41
3.1. Transmission Electron Microscopy	41
3.2. energy dispersive X-ray spectroscopy (EDX)	42
3.3. Superconducting Quantum Interference Device (SQUID)	43
3.4. X-ray powder diffractometer	45
3.5. X band Electron spin resonance (ESR) spectrometer	46
4. Analysis and computer-based implementation of various magnetism models	49
4.1. LANGEVIN-model and other approaches towards superparamagnetism	49
4.1.1. Theoretical background	50
4.1.2. <i>Mathematica</i> implementation and challenges	51
4.2. STONER-WOHLFARTH-model	55
4.2.1. Theoretical background	55
4.2.2. Extended critical field	60
4.2.3. <i>Mathematica</i> implementation	62

4.2.4.	Co _x Ni _{1-x} nanoparticles and fits	64
4.3.	JILES-ATHERTON-model	69
4.3.1.	Theoretical background	69
4.3.2.	<i>Mathematica</i> implementation	71
4.4.	Conclusions	71
5.	NiTi and Ni nanoparticles	73
5.1.	TEM measurements on NiTi nanoparticles	73
5.2.	Sample preparation for SQUID measurements	76
5.3.	Influence of the LASiS liquid on the magnetic behaviour	77
5.3.1.	EDX measurements	78
5.3.2.	Hysteresis measurements	80
5.3.3.	ZFC-FC measurements	82
5.3.4.	AC measurements	86
5.4.	Exchange bias in Ni nanoparticles	97
5.5.	Conclusions	99
6.	Fe₃O₄ and Fe nanoparticles	101
6.1.	Influence of laser power on the magnetic behaviour of Fe nanoparticles	101
7.	Conclusions and perspectives	107
8.	Acknowledgements	109
	Bibliography	111
	List of Figures	125
	List of Tables	127
A.	Statutory declaration	129
B.	Superparamagnetism model related <i>Mathematica</i> code	131
B.1.	Initialisation and Formulæ	131
B.2.	Fitting routines	133

C. Stoner-Wohlfarth <i>Mathematica</i> code	135
C.1. Simulation of STONER-WOHLFARTH hysteresses	135
C.1.1. Initialisation	135
C.1.2. Required Formulæ	138
C.1.3. Loops and calculations	140
C.2. Fit of a STONER-WOHLFARTH hysteresis to experimental data . .	150
C.2.1. Calculation of the deviation of a simulated hysteresis compared to experimental data	150
C.2.2. Final function / interface	155
C.2.3. Exemplary usage	161
D. Jiles-Atherton <i>Mathematica</i> code	163
D.1. Simulation of JILES-ATHERTON hysteresses	163
D.1.1. Required Formulæ	163
D.1.2. Implementation of the classical RUNGE-KUTTA fourth-order method	165
D.1.3. Final function and example	165

List of symbols

Symbol	Description	Unit
a	Parameter in the JA model that is related to the shape of the anhysteretic magnetisation.	A m^{-1}
$a_{(-)\vec{k}}^{(*)}$, $b_{(-)\vec{k}}^{(*)}$	Prefactor needed for the BLOCH states, * denotes the complex conjugated form that also has the minus sign in front of the momentum.	
α	Represents the strength of the interdomain coupling in the JA model.	
α_d	Empirical parameter in the modified COLE-COLE model. Quantifies the broadness of the relaxation time distribution.	
$\bar{\alpha}_d$	Averaged α_d .	
B	Magnetic induction.	T
$\mathcal{B}(\xi)$	BRILLOUIN function.	
c	Takes the material dependent ease of magnetic reversibility in the JA model into account.	
χ	Complex magnetic susceptibility. The definition reads $\chi = dM/dH$.	
χ_{dia}	Diamagnetic susceptibility.	
χ_{pau}	PAULI paramagnetic susceptibility.	
χ'	In-phase part of the magnetic susceptibility.	
χ''	Out-of-phase part of the magnetic susceptibility.	
C_1	CURIE constant of the CURIE-WEISS law with critical scaling behaviour.	K

Symbol	Description	Unit
C_2	CURIE constant of the CURIE-WEISS law.	K
D_{mag}	Magnetic diameter of the nanoparticles.	
δ	Returns the sign of the temporal derivation of the external field.	
δt	Characteristic time respecting the temperature sweeping rate.	
δ_M	Prefactor that is necessary to rule out the possibility of unphysical behaviour (increasing external field while magnetisation decreases) in the JA model.	
\mathcal{D}, \mathcal{F}	Anisotropy constants.	J
D	Diameter of the nanoparticles.	m
D_m	Median diameter of a log-normal distribution.	
d_{lp}	Length between two parallel lattice planes, not necessarily equivalent to λ_{lat} .	m
$\Delta E_{\text{barrier}}$	Single particle energy barrier that needs to be overcome to get a magnetic reversal in a superparamagnetic nanoparticle.	J
E_F	FERMI energy.	J
$\Delta E_{ \uparrow\rangle- \downarrow\rangle}$	Energy gap between the spin up state and the spin down state of an electron in an external magnetic field.	J
J	Exchange integral.	J
$f(\lambda)$	Optical oscillator strength.	
$f^{\text{LN}}(D)$	Log-normal probability density function, equivalent to equation (4.3).	
f	Represents the ac measurement frequency.	Hz
f_0	»attempt« frequency to overcome the energy barrier in a nanoparticle.	Hz
g	LANDÉ g -factor.	

Symbol	Description	Unit
γ	Ising critical exponent.	
$\gamma_{\uparrow\downarrow}$	Transition rate from one spin half band to the other spin half band.	s^{-1}
γ_{sc}	Total spin reversal rate.	s^{-1}
$ 0\rangle$	Symbolizes the ground state.	
H	Stands for the applied field.	$A\ m^{-1}$
h	PLANCK constant.	J s
H_{eff}	Stands for the effective field that takes the influence of other domains into account.	$A\ m^{-1}$
H_{ac}	Amplitude of the driving field in ac measurements.	$A\ m^{-1}$
$\hat{\mathcal{H}}_{at}$	Additional terms like, for example, dipole-dipole interaction terms in the electrons spin hamiltonian.	J
H_c	Stands for the coercivity, that is the applied field that is necessary to completely remove the materials' remaining magnetisation.	$A\ m^{-1}$
H_{cr}	Embodies the critical field that determines the »jump« in the SW model.	$A\ m^{-1}$
H_{crna}	Stands for the size dependent coercive field without angular dependency in the SW model.	$A\ m^{-1}$
$\hat{\mathcal{H}}_{es}$	Electrons spin hamiltonian, see equation (3.5).	J
H_{EB}	Exchange bias field caused by ferro-/antiferromagnetic contact layers.	$A\ m^{-1}$
H_{ext}	Represents the external applied field.	$A\ m^{-1}$
\dot{H}_{ext}	Represents the temporal change of the external applied field.	$A\ (m\ s)^{-1}$
H_i	Represents the projection of the external applied field H_{ext} onto the i -axis with $i \in \{x, y\}$.	$A\ m^{-1}$
H_K	Anisotropy field.	$A\ m^{-1}$

Symbol	Description	Unit
H_{\max}	Stands for the maximum applied field in the JA model.	A m^{-1}
h_{sl}	Peak-to-valley height of a ferro-/antiferromagnetic surface.	m
i	Imaginary unit.	
i, j	Iterators.	
i'	Upper limit of the sum in equation (4.7).	
J	Total angular momentum quantum number, obtained by combining the orbital angular momentum quantum number with the intrinsic angular momentum quantum number.	
k	Prefactor in the calculation of the the JA model that accounts for the total energy dissipated by moving domain walls.	A m^{-1}
k_{B}	BOLTZMANN constant.	J K^{-1}
\vec{k}	Momentum.	N s
$K_{\alpha}, K_{\beta}, L_{\alpha}$	Denotes the different transitions in an atom. K_{α} stands for a transition between the K and the L shell, K_{β} for a transition between the K and the M shell and L_{α} for a transition between the L and the M shell.	
K	Material dependent anisotropy constant.	J m^{-3}
K_{eff}	Material dependent effective anisotropy constant.	J m^{-3}
λ_{B}	Wavelength of the X-rays utilized for X-ray powder diffractometry, used for example in BRAGGS law.	m
$\lambda_{\text{start}}^{\text{dia}}$	Represents the smallest diameter of the considered nanoparticles that is taken into account by the corresponding <i>Mathematica</i> simulation. Usually one should choose $\lambda_{\text{start}}^{\text{dia}} = \lambda_{\text{spm}}$.	m
λ^{dia}	Represents the diameter of the considered nanoparticles. Equivalent to D .	m

Symbol	Description	Unit
$\lambda_{\text{step}}^{\text{dia}}$	This is the diameter stepsize that is used in the <i>Mathematica</i> simulations using a discretized size distribution.	m
$\lambda_{\text{end}}^{\text{end}}$	Represents the largest diameter of the considered nanoparticles that is taken into account by the corresponding <i>Mathematica</i> simulation. Usually one should choose $\lambda_{\text{end}}^{\text{dia}} = \lambda_{\text{sd}}$.	m
λ_{lat}	Lattice constant of the considered material.	m
λ_{sd}	Critical diameter of a single domain nanoparticle, above which multi domain ferromagnetism occurs.	m
λ_{spm}	Critical diameter of a single domain nanoparticle, below which superparamagnetism occurs.	m
$\mathcal{L}(\xi)$	LANGEVIN function.	
M_{ac}	Symbolizes the ac dependent magnetisation.	A m ⁻¹
M_{an}	Anhysteretic magnetisation. Used in the JA model to distinguish the two types of magnetisation behaviour that are taken into account within this model.	A m ⁻¹
m_{max}	Maximum of the magnetic moment.	A m ²
m	Magnetic moment.	A m ²
m_{FC}	Magnetic moment of the field cooling curve.	A m ²
m_{sat}	Saturation magnetic moment.	A m ²
m_{ZFC}	Magnetic moment of the zero field cooling curve.	A m ²
M	Magnetisation.	A m ⁻¹
M_{dia}	Diamagnetic magnetisation, id est the magnetisation of a diamagnetic material.	A m ⁻¹
M_{rem}	Remanent magnetisation, the magnetisation of the considered material that remains after removing external fields.	A m ⁻¹
M'_0	FC magnetisation at 0 K.	A m ⁻¹
M_{FC}	Magnetisation of the FC curve.	A m ⁻¹

Symbol	Description	Unit
M_{an}	Irreversible magnetisation, due to impurities. Contributes the main part of the hysteretic behaviour in the JA model.	A m^{-1}
M_0	ZFC magnetisation at 0 K.	A m^{-1}
M_{ZFC}	Magnetisation of the ZFC curve.	A m^{-1}
$M_{\text{asc}}^{\text{SW}}$	The magnetisation of the <i>ascending</i> branch of the hysteresis in the SW model.	A m^{-1}
$M_{\text{asc,n}}$	The normalised magnetisation of the <i>ascending</i> branch of the hysteresis in the SW model.	A m^{-1}
$M_{\text{desc}}^{\text{SW}}$	The magnetisation of the <i>descending</i> branch of the hysteresis in the SW model.	A m^{-1}
$M_{\text{desc,n}}$	The normalised magnetisation of the <i>descending</i> branch of the hysteresis in the SW model.	A m^{-1}
M	Metal alcoholate, confer reactions (2.i) and (2.ii).	
M^{JA}	Stands for the magnetisation in the JA model.	A m^{-1}
M_{sat}	The saturation magnetisation.	A m^{-1}
$\vec{M}_{\text{sat,asc}}$	The saturation magnetisation vector of the <i>ascending</i> branch of the hysteresis in the SW model.	A m^{-1}
$\vec{M}_{\text{sat,desc}}$	The saturation magnetisation vector of the <i>descending</i> branch of the hysteresis in the SW model.	A m^{-1}
M^{SW}	Stands for the projection of M_{sat} onto the external field direction in the SW model.	A m^{-1}
μ_{B}	BOHR magneton.	J T^{-1}
μ^{mCC}	Magnetic moment according to a modified COLE-COLE model.	J T^{-1}
μ_{ZFCFC}	Magnetic moment of a paramagnetic ZFC-FC curve.	A m^2
μ'_0	The magnetic constant is defined to have the value of $4\pi \cdot 10^{-7}$, such that it is <i>exact</i> . Also known as vacuum permeability.	N A^{-2}

Symbol	Description	Unit
μ'_0	Magnetic moment at zero frequency.	A m ²
μ^{LN}	One of the parameters that characterize a log-normal distribution, confer equation (5.1).	
μ_∞	Magnetic moment at an infinitely high frequency.	A m ²
μ'	In-phase magnetic moment.	A m ²
μ''	Out-of-phase magnetic moment.	A m ²
μ_r	Remanent magnetic moment.	A m ²
μ_{sat}	Saturation magnetic moment.	A m ²
μ_{satpa}	Saturation magnetic moment per atom. Usually given in units of μ_B .	A m ²
N	Number of magnetic nanoparticle clusters in equation (4.2).	
n_{do}	Symbolizes the diffraction order in equation (3.4).	
N_A	AVOGADRO constant.	mol ⁻¹
\mathbb{N}_+	Natural numbers greater than zero.	
n, n'	Variables used in chemical notation, for example in reaction (2.1) and reaction (2.11).	
ν	Temperature dependent switching frequency.	Hz
ν_0	Switching frequency at $T = \infty$ K.	Hz
ν_{mw}	Microwave frequency needed in an ESR spectrometer to get resonant behaviour.	Hz
ω	Circular frequency needed in the simulation of the extended JILES-ATHERTON model that allows the applied field to be alternating.	s ⁻¹
ω_{ac}	Driving circular frequency of the applied alternating field of the MPMS XL 7 used in ac measurements.	s ⁻¹
pdf(D)	Log-normal probability density function, equivalent to equation (5.1).	

Symbol	Description	Unit
φ_{ac}	Phase of the complex magnetic susceptibility.	°
ϕ	Angle in the SW model between the projection of the external magnetic field onto the xz -plane and the x -axis of the considered particle, confer figure 4.3.	°
ϕ_0	Angle in the SW model between the projection of the saturation magnetisation onto the xz -plane and the x -axis of the considered particle, confer figure 4.3.	°
π	Ratio of a circle's circumference to its diameter, defined as $\pi = 3.141\ 59 \dots$	
$\Psi_{\vec{k},\uparrow}, \Psi_{\vec{k},\downarrow}$	Spin up respectively spin down BLOCH states.	J T^{-1}
\vec{r}	Position vector.	m
R^2	Coefficient of determination.	
σ^{LN}	One of the parameters that characterize a log-normal distribution, confer equation (5.1). It is equivalent to w .	
S_i, S_j	Represents the i th respectively the j th spin.	
\hat{S}_z	Electron spin operator in z direction.	J s
$ \uparrow\rangle, \downarrow\rangle$	Spin up respectively spin down state.	
$S_{x(i)}, S_{y(i)}, S_{z(i)}$	Projection of the i th spin on the $x(i), y(i), z(i)$ axis.	
T_N	NÉEL temperature.	K
τ	Empirical parameter in the modified COLE-COLE model.	s
T	Temperature.	K
T_1	Temperature in the CURIE-WEISS law with critical scaling behaviour.	K
T_2	Temperature in the CURIE-WEISS law, equivalent to the WEISS constant.	K
$\langle T_{\text{block}} \rangle$	Average temperature of system blocking. Corresponds to the maximum of the ZFC curve.	K

Symbol	Description	Unit
T_{block}	Blocking temperature of monodisperse nanoparticles.	K
T_C	The CURIE temperature is the critical temperature, above which ferromagnetism does not occur, due to thermal fluctuations.	K
T_{irr}	Irreversibility temperature. Corresponds to the blocking temperature of the largest particles. Often determined via equation (2.1) or similiar approaches.	K
T_{max}	Temperature of a (local) peak in a temperature dependent measurement of the magnetic moment.	K
θ	Angle between the saturation magnetisation and the easy axis of the considered particle in the SW model.	°
Θ	WEISS constant, equivalent to T_2 .	K
θ_{asc}	Angle in the SW model between the ascending saturation magnetisation vector and the considered particles' easy axis.	°
ϑ	Angle between the X-rays and the lattice plane in BRAGGS law.	°
θ_{co}	Above this angle the so-called »cross-over« occurs in the SW model, in which the ascending hysteresis branch increases to a higher value than the decreasing hysteresis branch.	°
θ_{desc}	Angle in the SW model between the descending saturation magnetisation vector and the considered particles' easy axis.	°
θ_{end}	Ending angle in the extended SW model.	°
θ_{ht}	Angle in the SW model between the tangent of the astroïd in the point where the elongation of the external magnetic field vector intersects the astroïd and the considered particles' easy axis.	°
θ_{res}	Angle that minimizes the total energy density, equation (4.12), in the SW model.	°

Symbol	Description	Unit
θ_{start}	Starting angle in the extended SW model.	°
θ_{step}	Angle stepsize in the extended SW model.	°
θ_{uga}	Represents the angle between the upper green arrow and the easy axis, confer figure 4.5a.	°
θ_0	Angle between the external magnetic field and the easy axis of the considered particle in the SW model.	°
t	Time.	s
t^{JA}	Time in the trick used in the JA model.	s
V_{mag}	Volume of a magnetical cluster.	m^3
$\langle V \rangle$	Average volume of a nanoparticle.	m^3
V_{m}	Molar volume.	m^3
w	Dispersion of the log-normal distribution, equivalent to μ^{LN} .	
W_{mc}	Magnetocrystalline energy density of a SW particle.	J m^{-3}
W_{ms}	Magnetostatic energy density of a SW particle.	J m^{-3}
$W_{\text{ges}}^{\text{SW}}$	Total energy density of a SW particle.	J m^{-3}
W	»Wavelength« of the roughness of a ferro-/antiferromagnetic surface.	m
x	Variable used in chemical notation.	
\bar{X}	Empirical parameter that indicates superparamagnetic or spin glass-like behaviour.	
ξ	Ratio of the magnetic to the thermal energy.	
$\tilde{\xi}$	Ratio of the saturation magnetic to the thermal energy.	

List of abbreviations

ac	Alternating current.
CCD	Charge-coupled device.
dc	Direct current.
DLS	Dynamic light scattering.
EPR	Electron paramagnetic resonance.
ESR	Electron spin resonance.
EDX	Energy dispersive X-ray spectroscopy.
FC	Field cooling.
ISO	International Organization for Standardization.
JA model	JILES-ATHERTON model.
LASiS	Laser ablation synthesis in solution.
MPMS	Magnetic property measurement system.
MRI	Magnetic resonance imaging.
NMR	Nuclear magnetic resonance.
rf	Radio frequency.
SEM	Scanning electron microscope.
SW model	STONER-WOHLFARTH model.
SW particle	Usually a prolate, ellipsoidal particle exhibiting an uniaxial anisotropy.
SQUID	Superconducting quantum interference device.
SI	Système international d'unités, the most widely used metric system.

List of abbreviations

TEOS	tetraethyl orthosilicate, $\text{Si}(\text{OC}_2\text{H}_5)_4$.
TEM	Transmission electron microscope.
ZFC	Zero field cooling.

1. Introduction and motivation

Nanoparticles are particles of below 100 nm in size and can be found in centuries old church windows, modern sun blockers and catalysts. In spite of their small spatial dimensions they have a huge impact in our modern world, as reflected by an expected global market of 4.2 billion dollars in 2019 [2]. One reason for their vast amount of applications in numerous fields is the ability to tailor explicitly their chemical composition as well as their magnetic properties. To advance the fields of application a plethora of production methods and their outcoming nanoparticles have been scrutinized worldwide [3, 4]. Amongst the huge number of technological purposes are magnetically separable nanocomposites functioning as catalysts in many chemical syntheses [5]. Further, they have a huge importance in biotechnology as elucidated by the use of biocompatible nanoparticles as hyperthermia agents to kill tumour cells with an observed convalescence rate between 78 % and 90 % for mice [6]. In addition, they are successfully used as biomarkers in magnetic resonance imaging applications [7]. Furthermore, they are expected to help to increase data storage density to a few terabits per square centimetre [8].

Apart from their impact in technology, nanoparticles, especially magnetic ones, are still of growing significance in basic research [9], as the down-sizing of bulk material has far-reaching consequences on the material properties that eventually lead to new phenomena. This is exemplarily the case with superparamagnetic behaviour that stems from ferromagnetic nanoparticles of such low diameter that the timescale of thermal fluctuations plays a key role in their magnetic behaviour.

Applications of magnetic nanoparticle systems as model systems allow the testing of the multitude of advanced magnetism models. One of the most used models is the extended Langevin model [10] that describes superparamagnetic properties while taking the nanoparticle size distribution into account. Further commonly used models are the extended STONER-WOHLFARTH model, [11] which is appropriate for single domain ferromagnetic nanoparticles and the extended JILES-ATHERTON model [12] for multi domain ferromagnetic nanoparticles. In particular, the STONER-WOHLFARTH model used throughout this thesis offers a wide range of customizable parameters, such as the particle size distribution and

the anisotropy constant, to name a few. Another model worth mentioning used to describe magnetic behaviour is for example the PREISACH model [13], which has not been taken into consideration in this thesis. A combination of all these considered models that successfully describes the variety of occurring magnetic phenomena, such as superparamagnetism, single and multi domain ferromagnetism, which can be present in one nanoparticle species at the same time still remains a computational challenge. One goal of this thesis was to gain more insight on how these different models are applicable to different types of nanoparticles in order to describe their magnetic phenomena in dependence on their production procedure. Irrespectively, all models used throughout this thesis were implemented in *Mathematica* and documented extensively.

In the thesis on hand the following nanoparticles were investigated thoroughly: First, the sol-gel produced $\text{Co}_x\text{Ni}_{1-x}$ nanoparticles provide a link to the models described above, as they serve as a superparamagnetic model system (with $x = 0$) on which the extended LANGEVIN model was tested. Furthermore, magnetic properties of the nanoparticles with $x = 0.5$ can be tuned with a laser, since they show a wavelength dependent coercivity and thus allow the modulation of the magnetisation dynamics [1]. This is why a modified STONER-WOHLFARTH model was implemented to describe this interesting phenomenon. Second, NiTi nanoparticles which show highly interesting features, for example shape memory properties, biocompatibility and high resistance to corrosion and material fatigue, that suggest a use as implant surface and thus integration enhancers [14–16], have been investigated. Consequently, it is of great interest to look at the properties of NiTi nanoparticles and conduct a comprehensive characterisation, especially if they are produced by the »simple« and »green« production method LASiS. Such a characterisation contributes to a better understanding of the fabrication procedure, which is inevitable for optimisations and estimations on their future use in biological systems and possible ways of tailoring the nanoparticle parameters as appropriate for specific tasks. In the same manner Fe nanoparticles that were created via LASiS at different laser powers were used to estimate the impact of laser power on the magnetic behaviour, as the laser power is one of the tunable parameters that should allow a fine configuration of specific properties.

To provide the basis for the needed experiments and applied models, this thesis begins with an overview of the fundamentals of nanoparticles and the relevant measurement techniques. Afterwards the analysis and computer-based implementation of various magnetism models is discussed, followed by a comprehensive magnetic characterisation of NiTi and Fe nanoparticles. Finally, conclusions are drawn and



perspectives on this subject are explained. All the developed programs and codes have been uploaded online as to provide an open source »toolbox« which can be accessed by researchers worldwide.

2. Fundamentals of nanoparticles

Nanoparticles are in most cases – and by the ISO – defined as particles whose length in each of the three spatial dimensions does not exceed 100 nm and does not fall short of 1 nm [17, 18]. Note that if the length in one or two dimensions is by a factor of at least three bigger, it is appropriate to label these objects nanofibres respectively nanoplates.

definition of nanoobjects

There are numerous ways to obtain nanoparticles. Upon some that are relevant for this thesis will be shed light in the subsequent section 2.1.

2.1. Fabrication methods

For a short overview of some of the plethora of available methods see table 2.1. Further information, although exemplary in nature, can be found in the work that is cited for each procedure. A procedure of higher importance for this thesis, as some of the nanoparticles used throughout were produced via this pathway, is explained in more detail in the following section 2.1.1.

2.1.1. Laser ablation synthesis in solution

An advantage of one of the methods chosen in this thesis, laser ablation synthesis in solution, is that the procedure is straightforward as well as easy – from an engineering point of view, as neither long reaction times nor the control of complex chemical multi step reactions is necessary. It has to be noted that although high temperatures *do* occur, they are confined to very small regions and hence experimentally easy to control. No problematic chemicals, as exempli gratia toxic substances, are needed while the method still offers a wide range of products. As a consequence, LASiS is considered to be a »green« nanoparticle synthesis method. The usage of water as liquid allows the synthesis of very pure nanoparticles (although the nanoparticles practically always contain oxidized versions of the substrate metal) which is of great importance for medical in vivo applications, as reaction by-products may be harm-

advantages of laser ablation synthesis in solution (LASiS)

Table 2.1.: Comparison of different (magnetic) nanoparticles production methods (confer [3]). Coprecipitation is a wet chemistry approach that exploits that, upon precipitation of one component, another component gets swept along. Thermal decomposition works, as the name indicates, by a heat-induced chemical decomposition. Hydrothermal synthesis makes use of phase transfer effects taking place at the liquid–solid–solution interfaces of the used materials. Laser ablation synthesis in solution, LASiS, is described in more detail in section 2.1.1. The solid-gel technique (applied to a carrier substrate via dip-coating) is characterized in section 2.1.2. Microemulsion uses inverse micelles, each filled with one of two different reactants, so that upon collision of two inverse micelles of different included reactants precipitation takes place and thus forms the nanoparticles in »nanoreactors«. The cited works in this table are exemplary and not exhaustive.

Method	Synthesis and duration	Solvent	Size distribution and shape control	Yield
coprecipitation [19]	simple, minutes	water	relatively narrow, bad	high, scalable
thermal decomposition [20]	complex, hours up to days	organic compound	very narrow, very good	high, scalable
hydrothermal synthesis [21]	simple, hours up to days	water-ethanol	very narrow, very good	medium
LASiS [22, 23]	simple, minutes	water, organic compounds	relatively narrow, good	medium
Sol-gel [24]	simple, hours	organic compounds	very narrow, good	good, scalable
microemulsion [25]	complex, hours	organic compound	relatively narrow, good	low

ing to living organisms. Functionalisation can be achieved by choosing a pertinent solution in that the ablation takes place or by adding relevant chemicals *after* the ablation. The nanoparticles' properties can be fine-tuned by changing the liquid (respectively the gaseous or evacuated) environment, the substrate (metal or arbitrary metal alloys), the laser wavelength, pulse energy, pulse duration, pulse width and pulse repetition rate. LASiS is a top-down approach to produce nanoparticles, whilst exempli gratia wet chemistry is a bottom-up method.

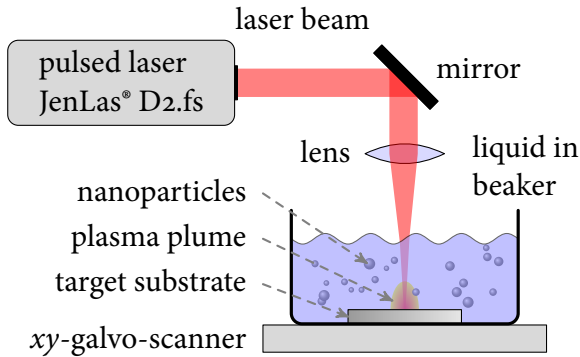


Figure 2.1.: The picture illustrates schematically the experimental LASiS setup. The femtosecond pulsed laser is focused onto the movable target (metal) substrate, where a small plasma plume with ablated material is established, which upon cool down forms the nanoparticles. For further information confer section 2.1.

The experimental setup used to produce the nanoparticles that were measured in this thesis is shown in figure 2.1. The Yb:KYW femtosecond laser system JenLas® *D2.fs* by JENOPTIK AG [26] was used to generate laser pulses with a duration of 300 fs, a peak wavelength of 1.025 μm , a repetition rate of 100 kHz and a maximum used pulse energy of 28.8 μJ . Subsequently the pulses were focused by a lens onto the metal substrate (in this thesis NiTi-alloy respectively Fe) on which the laser's focal spot had an approximate diameter of 37 μm . A *xy*-galvo-scanner was used to move the metal substrate around while ablating. As the metal substrate was located on the bottom of a beaker filled with the chosen solutions one had to let the solution evaporate after the generation of the nanoparticles took place, if pure nanoparticle powder is sought. This has the disadvantage of easier pollution, *exempli gratia* resulting in oxidization.

In contrast to the ease of LASiS from an engineering point of view it is complex in terms of physical processes. As the laser beam hits the target substrate, its energy is transmitted into the electrons of the material. The ratio of the laser pulse duration to the material specific electron-phonon coupling time constant is decisive for the dominating physical effect. For example, a nanosecond pulse would generate, after carrier thermalisation (takes time on the order of 100 fs) and energy transport into the lattice via electron-phonon coupling (takes time on the order of 1 ps), heat, due to the dissipation of the consequently accumulated lattice energy. Thus, even for low fluences, the target substrate locally melts and subsequently vaporizes. If the laser pulse duration is smaller than the electron-phonon coupling time constant the laser beams' energy stays trapped in the irradiated area, such that the sublimation enthalpy is considerably smaller than the surface enthalpy. Hence, the material sublimates directly. The proposed model for these pulses is the fragmentation model,

description of the experimental setup used to obtain the nanoparticles

overview of the physical processes of importance in LASiS

that describes the immediate ejection of substrate material due to photomechanical effects. However, if the fluence of these short pulses exceeds a critical point the solid-liquid-vapour transition is becoming increasingly dominant.

description of the plasma plume created by the laser

The created plasma plume has temperatures above 10^4 K, an expansion speed of circa 10^4 m s⁻¹ and pressures larger than 10 GPa. By expanding adiabatically in a time on the order of nanoseconds the plasma starts to cool down. As a consequence of the expanding high pressure plasma plume the liquid in the beaker gets compressed and strongly heated locally, hence giving rise to an *external* shockwave at the plasma-liquid surface. The locally heated background liquid vaporizes and forms the »liquid plasma« that mixes in the vicinity of the plasma-liquid interface with the substrate plasma. Consequently there are many possible chemical reactions that prevent the formation of ultrapure substrate nanoparticles – at least, with water as background liquid, it is possible to obtain nanoparticles that consist of *oxides* of the initial target substrate. Upon further expansion the plasma at the edge of the plume loses energy to the background liquid, such that the plasma components get decelerated leading to a reverse pressure gradient. Ergo an *internal* shockwave is formed that advances inwards until the shockwave converges and the direction of the shockwaves motion inverts. Thus the internal shockwave cycles between the plasmas' centre and the plasma-liquid interface, thermalising the components of the plasma. The cooling of the plasma plume creates the nanoparticles via condensation, nucleation and clustering (mainly for the temporal long nanosecond laser pulses). As the plasma cools roughly with 10^{10} K s⁻¹ the occurring nonlinearities are the main reason for a comparably broad nanoparticle size distribution (confer table 2.1). Due to the forming concentration gradient the produced nanoparticles are diffusing into the background liquid.

influence of intra- and interpulse interactions

There are two more interactions that may play a key role in the generation of the nanoparticles. First, the nanoparticles can interact with the laser pulse that generated them, thus this would be an *intrapulse* interaction, particular important for nanosecond pulses. Secondly a subsequent laser beam can interact with the nanoparticles generated by the previous pulse, this *interpulse* interaction is important for femtosecond pulses. These interactions usually narrow the nanoparticle size distribution, hence they are a possibility to *tune* the nanoparticles' size distribution.

Two effects are probably responsible for the narrowing. Photochemical bleaching by the laser photons can lead to the ejection of electrons from the nanoparticles. Consequently the remaining nanoparticles are highly charged. Above a critical charge the repulsive COULOMB force is bigger than the attractive cohesive force, immediately leading to the so-called COULOMB explosion that effectively splits the

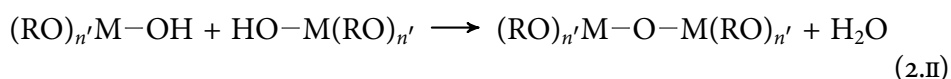
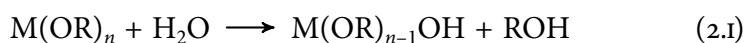
nanoparticles. If the temperature of a nanoparticle gets high enough by absorbing photons the same effects that lead to the initial separation from the target substrate can take place again, also reducing the nanoparticle size distribution.

For further information see [27, 28], upon which this section is based. This technique however does not support the formation of nanoparticles *embedded* in a matrix of another material, which proves useful to minimize possible interactions between the nanoparticles. Consequently, a method covering this requirement is described in section 2.1.2.

2.1.2. Sol-gel dip-coating

In contrast to the approach explained in section 2.1.1 the wet chemistry sol-gel dip-coating method [24] is an option to produce high quality alloy nanocluster doped thin films, with which, *exempli gratia*, many transition metal alloy nanoclusters have been prepared [29, 30]. The principal methodology of this technique consists of three major steps, namely the hydrolysis and condensation to obtain the sol, the drying afterwards leading to the gel and the subsequent heating that allows further polycondensation.

The precursor materials are usually alcoholates, for example tetraethyl orthosilicate (TEOS, $\text{Si}(\text{OC}_2\text{H}_5)_4$) which is often used. Reaction (2.I) shows the partial hydrolysis of a metal alcoholate denoted by »M«. The general condensation reaction is shown in reaction (2.II).



basic chemical reactions of the sol-gel method

Practically reaction (2.II) results in a dimer, that may further condensate and form a trimer, tetramer, ..., oligomer. After the formation of the particles, the production of the *sol* is accomplished.

Subsequently, a clean substrate is »dipped« into the sol and slowly and steadily withdrawn. Therefore, a layer with roughly uniform geometry should be received. It should be noted that for sols with high viscosity the withdrawal speed has to be much smaller to obtain a uniform geometry. Remaining liquids are then removed by either increasing the temperature or waiting until they evaporate. The particles' interconnectedness increases, such that a *gel* is formed.

procedural steps of the sol-gel dip-coating technique

In the last step the dried sample is heated to achieve the final, condensed state. It may be necessary to use specially composited atmospheres as, *exempli gratia*,

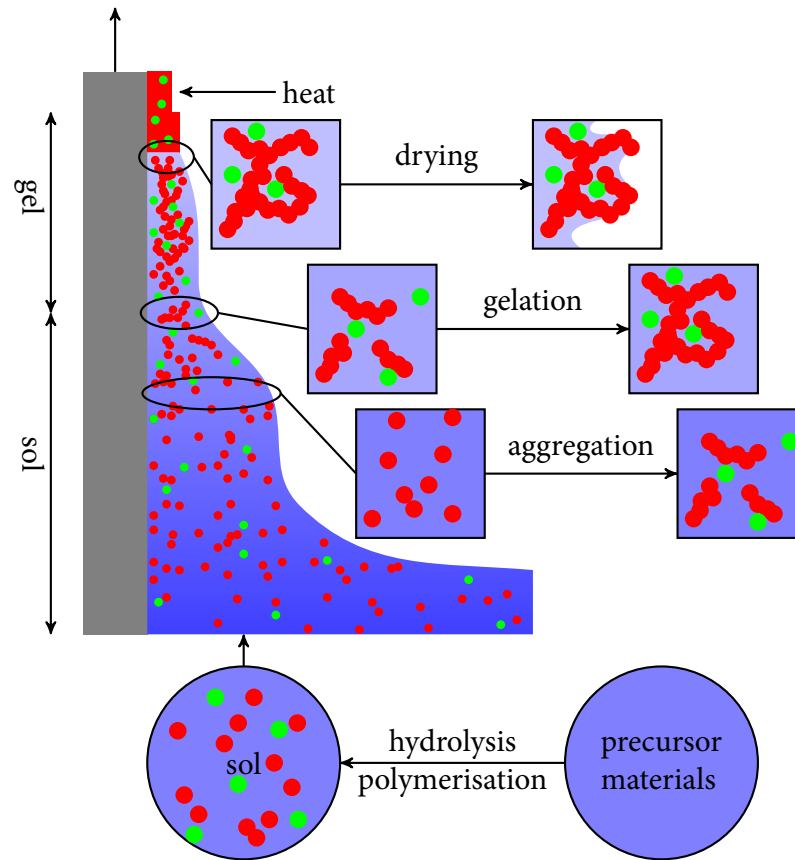


Figure 2.2.: This picture sketches the modus operandi of a sol-gel dip-coating procedure resulting in a silicon (●) matrix with embedded metal nanoclusters (●). Shortly spoken involves this method hydrolysis and polymerisation of the precursor materials, followed by aggregation and gelation taking place at the parts of the substrate that is already lifted above the solutions »baseline«. If these parts get lifted higher, more solvent evaporates, such that, after heating to get rid of remaining liquid as well as to increase the density via polymerisation, a thin matrix film with embedded metal nanoparticles is formed. The idea of the picture is based upon [31, 32].

a H_2-N_2 atmosphere. Sol-gel dip-coating has the advantage of being quite cheap, as the fluid dropping back into the reservoir can be used for further samples. If metal salts are added in the beginning, it is possible to obtain films that contain approximately evenly distributed nanoclusters [24]. Figure 2.2 illustrates the process.

This section is based upon [31, 33], that are also good sources for further reading. Both techniques explained thus far have the advantage of being able to produce *magnetic* nanoparticles. Hence the magnetic effects that may play an important role in magnetic nanoparticles are worthwhile some considerations, what is, in combination with a discussion of the structural properties of the nanoparticles, done in the subsequent section 2.2.

2.2. Structural and magnetic properties

There are a number of magnetic effects that have to be borne in mind if magnetic nanoparticles are investigated, as they are the main source of the corresponding magnetic behaviour. A short overview of the relevant types of magnetism is given subsequently.

- **Diamagnetism** is a phenomenon occurring in all atoms that squeezes an external magnetic field out. Though it can be described classically as an induced circulating current obeying LENZ's law [34], a quantum mechanical ansatz is more appropriate due to its completely quantum mechanical nature [35]. One then can utilize first order perturbation theory to obtain the magnetization M_{dia} that is oriented in the opposite direction of the external applied field. Typically M_{dia} is negative, small, but present in all materials. In most cases holds $-10^{-6} < \chi_{\text{dia}} < -10^{-4}$ true.
- **Paramagnetism**, contrary to diamagnetism, pulls an external field inwards the paramagnetic material. In the absence of an external magnetic field or if a previously applied external magnetic field is turned off, the magnetic dipoles are randomly orientated and interact only weakly, yielding no net magnetic moment. If a magnetic field is applied, a partial alignment of the magnetic moments can be observed. As a consequence a net magnetic moment that increases with decreasing temperature arises. The so-called PAULI-paramagnetism (typical orders of magnitude $10^{-5} < \chi_{\text{pau}} < 10^{-3}$) results from the contribution of the electron spins parallel to the applied field that are not compensated by electron spins with antiparallel orientation. Established is this superiority of parallel aligned electron spins by the spin orientation dependent, applied field driven shift of the density of states [34]. In the case of a ground state $|0\rangle$ total angular momentum of $J = 0$ the first order perturbation theory predicts the absence of paramagnetic effects. Taking second

basic properties of
diamagnetism

basic properties of
paramagnetism

order perturbation theory into account leads to the prediction of a small, temperature independent paramagnetic effect (referred to as VAN VLECK paramagnetism, typical orders of magnitude of the susceptibility are comparable with χ_{pau}), as excited states with $J \neq 0$ mix in [35].

- **Ferromagnetism** occurs in materials (for example in Co, Ni and Fe) in which magnetic moments are collectively aligned in each microscopic magnetic domain [36] even if there is *no* external magnetic field applied. The system tries to minimize the sum of the magnetostatic energy and the energy needed to maintain domain walls (in most cases BLOCH or NÉEL walls). Applying an external field increases the size of favoured domains reversibly, while sufficiently large fields also force the domain walls to »jump« over impurities that prevent reversibility if the field is turned off, thus giving rise to the hysteretic magnetisation behaviour observed experimentally. It is noteworthy that in a demagnetised, »virgin« ferromagnet the magnetisation equals zero, due to the random orientation of the magnetisation direction of each domain. For large external fields it is also possible that magnetic moments switch their direction simultaneously in a domain, resulting in small steps in the magnetisation curve. This phenomenon is named BARKHAUSEN-effect [35]. Ferromagnetism is only stable up to the CURIE temperature T_C , as further increasing the thermal energy will lead to paramagnetic disorder, due to the increasing importance of thermal fluctuations. To this day there is no consistent microscopic theory about ferromagnetism, even though the exchange interaction is known to be the driving force [34]. The exchange integral abbreviated by J , is decisive for the magnetic nature of the material, if $J > 0$ it shows ferromagnetic behaviour, if $J < 0$ it shows antiferromagnetic behaviour explained in the next point.
- **Antiferromagnetism** is observed in materials that typically have two sublattices, each ferromagnetic, but the spins of each sublattice are exactly opposed. This leads to three possible magnetisation curves, depending on the preference of the spins to align and the orientation of the external field. If the external field is perpendicular to the spins of the sublattice, their orientation towards the external field will increase approximately linear with growing field, until all spins are aligned and saturation is reached (confer figure 2.3a). On the conditions that the external field is parallel to one of the sublattices and that $T = 0$ K there are two cases to distinguish: In the first case there is

basic properties of
ferromagnetism

basic properties of
antiferromagnetism

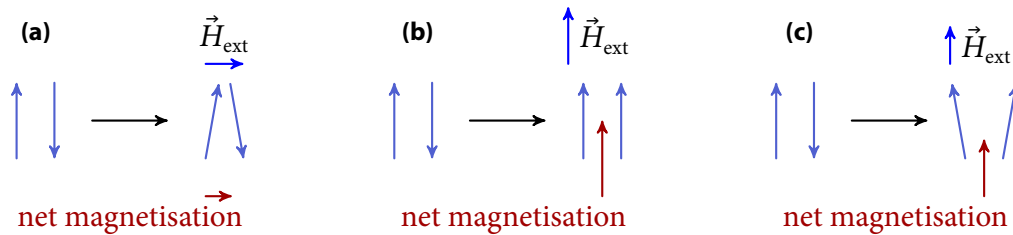


Figure 2.3.: (a) shows the change of the spin orientations if an external field is applied perpendicular to the initial spin orientation. (b) shows the spin-flip-transition, (c) depicts the spin-flop-transition. Further information can be found in section 2.2.

a strong preference for the spins to align parallelly, such that nothing happens if you increase the external field – until a critical field is reached and the spins of the antiparallel sublattice switch their orientation by 180° . This is called *spin-flip-transition*, see figure 2.3b. In the other case there is no such strong preference for the spins to align parallelly, thus the antiparallel sublattice will switch by less than 180° , causing the originally parallelly aligned sublattice to get a small offset. Further increase of the external field reduces the deviation from 180° , until all spins are parallelly aligned and saturation is reached. This effect is called *spin-flop-transition*, see figure 2.3c. If the temperature exceeds the NÉEL temperature T_N antiferromagnetic materials show paramagnetic behaviour, as thermal fluctuations take over.

- **Superparamagnetism** is found in sufficiently small ferromagnetic nanoparticles in which it is energetically favourable to only have *one* domain in a nanoparticle. If the temperature is high enough the thermal fluctuations will be large enough to allow flipping of the magnetic moments. As a consequence the nanoparticles will show paramagnetic properties. It should be noted that the magnetic moments of a whole nanoparticle (»one giant magnetic moment«) correspond to atomic magnetic moments in paramagnetism. This is the reason for calling this phenomenon *superparamagnetism*. In the case of decreasing temperatures the relaxation time increases, such that the magnetic moments appear to be *blocked* if the experimental measuring time is smaller than the relaxation time. One way to detect superparamagnetism is the ZFC-FC measurement procedure described in section 2.3.

basic properties of
superparamagnetism



Sample magnetisation curves for dia-, para-, ferro- and superparamagnetic nanoparticles can be found in figure 2.4a. As, for example, the magnetic properties depend upon the structural properties of the considered nanoparticles it is useful to recall some basic structural aspects that should be kept in mind.

Nanoparticles, especially those produced by LASiS, exhibit in most cases a core-shell structure, id est the core of the nanoparticles is formed by a different material than the surface. LASiS nanoparticles also consist of a mixture of materials that may lead to a superposition of a plethora of magnetic effects, as it is not possible to produce for example pure iron nanoparticles, due to the occurrence of oxygen and hydrogen in the plasma plume (with the assumption that water is used as solution), confer section 2.1.1. Furthermore the three-dimensional shape influences the magnetic behaviour, current theories typically assume spherical or ellipsoidal nanoparticles, neglecting the vast majority of possible forms, exempli gratia cubic and cylindric shapes.

The »toolbox« that allows the magnetic characterization of nanoparticles that exhibit one or more of the magnetic effects mentioned above is quite extensive. Results of these measurements may also allow conclusions about the structural properties of the nanoparticles. Thus some »tools« germane to this thesis are discussed in the succeeding section 2.3.

2.3. Magnetic characterization methods

Amongst the relevant characterization methods mentioned in this section one finds each a measurement depending on the applied field, the temperature and the frequency of the applied field. It has to be noted that in general the history of magnetic systems cannot be neglected and has to be known to be able to predict future behaviour. Exploitation of this incident can be done, for example, with the magnetisation curve measurement described in the following paragraph.

The method used in most cases to determine magnetic properties is the measurement of the field dependent magnetisation curve, exempli gratia via a SQUID-magnetometer (confer section 3.3). It should be kept in mind that a SQUID-magnetometer typically measures *only* the magnetic moment, thus the mass of the sample is necessary to obtain the magnetisation. Usually the curve is measured until saturation is achieved. Example curves can be found in figure 2.4a, depicting schematically the different, material dependent types of magnetisation curves one can measure. M_{rem} represents the *remanent magnetisation*, id est the magnetisation that remains

brief overview of
a typical nanoparticle
structure

if the externally applied field is set to 0. M_{sat} stands for the saturation magnetisation, the maximum value the magnetisation can reach. Thus increasing the external field above $H(M_{\text{sat}})$ does *not* lead to an increasing magnetisation. H_c symbolizes the coercivity of a material. While purely diamagnetic materials (—) exhibit a linear behaviour with a small negative slope, purely paramagnetic materials (—) do show a linear behaviour with a small positive slope. Purely superparamagnetic materials (—) demonstrate a logistic growth alike shaped behaviour, similar to how a purely ferromagnetic material (—) with $H_c = 0$ and thus no visible hysteresis would look like. The net magnetisation of the material is only completely suppressed if the external field is equal to the materials' coercivity and the magnetisation was saturated at an external field of the *opposite* sign. As this characterization method is often used to measure the magnetic behaviour of ferromagnets it is also referred to as *hysteresis* measurement.

explanation of the $m(H)$ hysteresis measurement

Another measurement routine is the zero field cooling - field cooling (ZFC-FC) procedure that allows the detection of temperature dependent, superparamagnetic behaviour. In the first step the sample is heated up to a reasonable temperature, usually approximately 300 K, such that the sample is to be found in the superparamagnetic state. Then the sample is cooled down to a sufficiently low temperature, for example 4 K. It is of vital importance to cool down *without* an externally applied field, as otherwise the magnetic moments are »frozen« while being aligned in direction of the external field. Subsequently, an external field is applied and the sample is heated up to the initial temperature the sample had before cooling down whilst recording the magnetic moment. The resulting data points form a ZFC curve as shown in figure 2.4b. Thereafter, the sample gets cooled down again, but this time the external field is *not* turned off. Meanwhile the magnetic moment is measured. The resulting data points constitute the FC curve¹, see figure 2.4b. Take into account that the speed of the temperature changes should be constant for all steps within the ZFC-FC procedure.

procedural steps of the ZFC-FC protocol

The initial increase in the ZFC curve is due to the temperature supported easier alignment of the particles along the external field. Hence, the system is *blocked* in this temperature region, as the time necessary to get thermal »flipping« of the direction of the magnetic moment of a nanoparticle exceeds the measurement time. The increase stems from the increasing amount of nanoparticles that are capable to switch within the measurement time. After this increase the ZFC magnetisa-

¹For the sake of simplicity called FC, a more precise term for the method used in this thesis would be FCC, field cooled cooling.

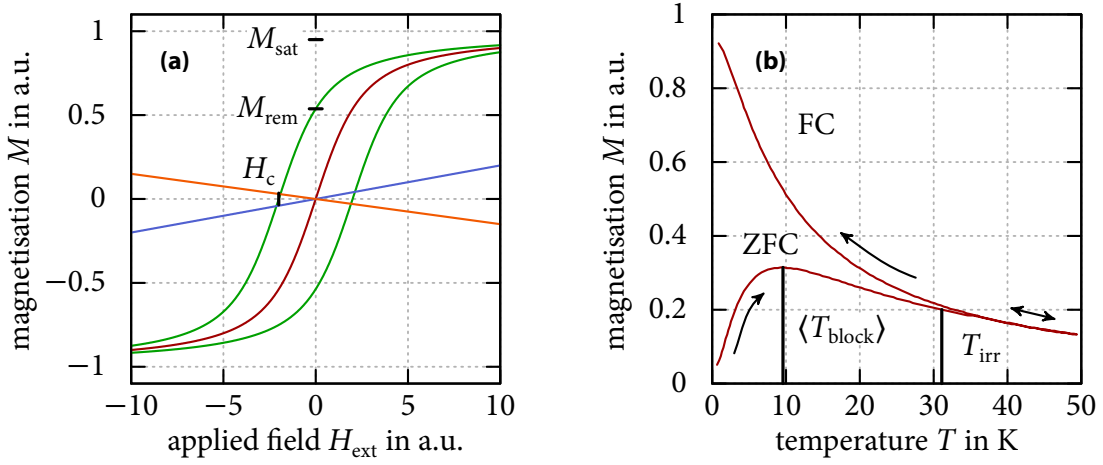


Figure 2.4.: (a) shows magnetisation measurements of ideal ferro- (—), superpara- (—), dia- (—) and paramagnetic (—) materials, leading to hysteretic, linear or logistic growth alike shaped behaviour. The remanent magnetisation M_{rem} , the saturation magnetisation M_{sat} and the coercivity H_c belonging to the ferromagnetic curve are marked in the plot. They are explained in more detail in section 2.3. Picture inspired by [37]. (b) depicts the result of a ZFC-FC simulation performed by [38], confer [39] for background information. A short explanation of the physics behind ZFC-FC measurements, as well as a description of $\langle T_{\text{block}} \rangle$ and T_{irr} can be found in section 2.3.

physical causes of the typical superparamagnetic ZFC-FC curves

tion reaches a maximum at the average temperature of system blocking, $\langle T_{\text{block}} \rangle$. Above $\langle T_{\text{block}} \rangle$ the system is *unblocked*, due to the fact that the thermal fluctuations are in this case large enough to allow switching of the nanoparticles' magnetic moments within the measurement timespan. Thus the nanoparticles exhibit paramagnetic behaviour in this regime. The irreversibility temperature T_{irr} corresponds to the blocking temperature of the largest particles and is consequently higher than $\langle T_{\text{block}} \rangle$ [40]. A common method to determine T_{irr} is to search the temperature for which, *exempli gratia*²,

$$\frac{M_{\text{FC}} - M_{\text{ZFC}}}{M_{\text{FC}}} = 0.05 \quad (2.1)$$

²The numerical value is obviously an arbitrary choice, justified as the lines can be considered converging if the deviation is smaller than 5%. Other measurements may justify different values.

holds true. The FC curve typically decreases monotonically from low temperatures, where all magnetic moments are »frozen« along the direction of the external field, to high temperatures, as the amount of thermal fluctuation induced disorder increases. Near the irreversibility temperature joins the FC curve the ZFC curve. ZFC-FC and hysteresis measurements are also commonly used in palaeogeology, as they are important to obtain a geomagnetic characterization of rock [41].

An additional measurement technique habitually used to characterize, for example, the superparamagnetism of nanoparticles is found within ac susceptibility measurements. There an alternating magnetic field with varying frequency is applied, see also section 3.3. The blocking temperature T_{block} for monodisperse nanoparticles of one species can be written in the NÉEL-ARRHENIUS theory [42] as

$$T_{\text{block}} = \frac{\Delta E_{\text{barrier}}}{\ln(f_0/f)k_B}, \quad (2.2)$$

wherein $\Delta E_{\text{barrier}}$ symbolizes the single particle energy barrier that needs to be overcome to get a magnetic reversal, f_0 is the »attempt« frequency to overcome the energy barrier, f corresponds to the ac measurement frequency and hence can be varied experimentally and k_B is the BOLTZMANN constant. As the out-of-phase susceptibility χ'' should show a peak at the measurement dependent blocking temperature, it is possible to check the validity of the assumed noninteractivity of the nanoparticles. If they do interact there will be a deviation from the measurement dependency of the blocking temperature shown in equation (2.2). Possible interactions include, exempli gratia, interparticle exchange interactions. Note that the SQUID-magnetometer measures the in- and out-of-phase magnetic moment, such that the sample mass is required to calculate the susceptibility.

This chapter is based upon [40, 41, 43, 44], that are also good starting points to delve deeper into the subject. The techniques described in this section are of great importance to be able to tailor the magnetic properties of nanoparticles to the current and future needs, some of which are described in the following section 2.4.

2.4. Applications

Possible applications of magnetic nanoparticles are found in the realms of catalysis and biotechnology. Exempli gratia these nanoparticles can be used to get catalysators that have a large surface while being easily separated from the other chemicals, for example with magnetic decantation.

ac measurement
techniques for mag-
netic nanoparticles

The data storage capacity is expected to increase to several terabit per square centimeter with magnetic nanoparticles [8, 45].

One of the most promising applications of magnetic nanoparticles is as heating agents in the field of hyperthermia. Therein magnetic nanoparticles get injected, sometimes directly in tumors, sometimes intravenously so that the nanoparticles enrich in tumors due to the leakiness of the correspondend blood vessels. Consequently, the nanoparticles have to be nontoxic. This can be achieved by using a biocompatible surface coating of the magnetic core of the nanoparticles. Applying an alternating external field results in heating the magnetic nanoparticles up to 60 °C, killing the tumor cells. This approach cures test mice in 78 % to 90 % of all cases [6]. Biocompatible magnetic nanoparticles, like NiTi nanoparticles, can also be deposited on implants to enhance their surface roughness such that the integration process improves [14, 16]. Another field of interest is the use of magnetic nanoparticles as vectors for targeted drug delivery, as they offer advantages such as guidance by application of a specific magnetic field, release of the attached drugs by heating and visualization in vivo via magnetic resonance imaging [46]. Finally the magnetic nanoparticles are used as »switches« that can thermally activate temperature dependent cation channels in neurons, triggering specific animal responses – with the advantage of removing the penetration depth limit of optically triggered approaches [47].

Further information can be found in [3], upon which this chapter is based. In order to be able to get near these promising prospects it is inevitable to have adequate measuring instruments at hands to utilize the magnetic characterization techniques explained in section 2.3. Furthermore some measuring instruments for non-magnetic measurements, exempli gratia to determine the nanoparticle size distribution, are valuable. Consequently some of the measuring instruments significant to the characterization of nanoparticles are described in chapter 3.

summary of the state
of the art use of mag-
netic nanoparticles
as hyperthermia
agents

3. Measurement techniques

The apparatuses used for magnetic and non-magnetic characterization methods deserve, irrespective of their widespread usage, some attention, as the underlying physical concepts are quite sophisticated. Thus these concepts are subsequently elucidated.

3.1. Transmission Electron Microscopy (TEM)

Invented in 1932 [49] is the TEM an effective method for examining nanoparticles, as the resolution is on the order of Ångström due to the small DE BROGLIE wavelength of electrons achieved by high acceleration voltages. In particular it is feasible to estimate the nanoparticles' size distribution via (manually) counting the size of a sufficient number of nanoparticles. The schematic drawing in figure 3.1 illuminates the functionality.

On top is an thermionic electron source, exempli gratia a lanthanum hexaboride (LaB_6) crystal that, by heating, emits the electrons which later form the electron beam. These electrons are less monochromatic, »whiter«, than electrons obtained via field emission, but can be used reasonably, as thermionic electron sources are generally much cheaper.

Using electromagnetic lenses and electrostatic plates it is possible to manipulate the resulting electron beam to be focused onto the sample, usually with an acceleration voltage of several tens of kilovolts. As the mean free path is otherwise too small, the whole electron beam path is located in vacuum. Due to the acceleration voltage dependent penetration depth of electrons, samples should not be thicker than approximately 100 nm, even though for very high acceleration voltages (up to

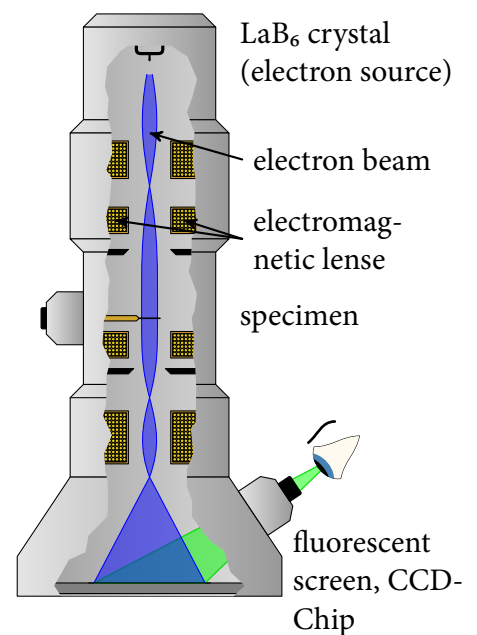


Figure 3.1.: Schematic drawing of the modus operandi of a TEM. Picture based upon [48].

some hundred kilovolts) reasonable sample thickness can reach some micrometer. After passing through the sample, the electron beam is captured by the image recording system below the sample holder, allowing for further digital processing.

sample preparation
for TEM

To acquire samples that can be measured with TEM the nanoparticles are first solved in acetone, subsequently putting a drop of the solution onto a carbon layer, thereupon letting the solvent evaporate, wherefore the nanoparticles remain on the substrate. Carbon is chosen as carrier substrate, as it does not interfere much with the electron beam. A good contrast of the picture is guaranteed, due to the magnetic nanoparticles' high electron density.

The TEM used in this thesis was a FEI Tecnai G² Sphera with an acceleration voltage of 200 kV. Extensive information about TEM can be found in [50].

It should be noted that this measurement instrument estimates the optical radius, other methods like dynamic light scattering (dynamic light scattering (DLS)) and its hydrodynamical size approximation are also usable [51], even though DLS is inaccurate for a broad nanoparticle size distribution, as larger nanoparticles are able to cover smaller nanoparticles, so that they are »invisible« to the measurement procedure [52]. Subsequently a technique that is often used jointly with TEM measurements and allows the determination which chemical substances are present is concisely explained.

3.2. energy dispersive X-ray spectroscopy (EDX)

physical mechan-
isms relevant to EDX

Another powerful tool, especially if combined with a TEM, that was used to gather data shown in this thesis is given by EDX. It is based on the fact that high energy electrons passing through a sample can lose energy by either ionizing atoms or generating continuous Bremsstrahlung. If atoms get ionized by loosing one of their inner electrons, a lower energy electron of outer shells will immediately »fall« into the created »hole« and thereby emit element and shell specific X-ray. The transitions are named K_{α} , K_{β} , ..., L_{α} , ..., whereby the latin letter indicates in which shell the electron was located before it was »kicked out«, while the greek letter specifies the shell the replacing electron initially was in. Thereafter a detector counts the amount of X-rays for each energy in its range. It is also possible that an AUGER electron is created. Note that there are experimental setups in which not an electron beam but an X-ray is used as source of the atoms ionisation. An illustrative picture that may help to clarify the underlying mechanism is shown in figure 3.2.

While the Bremsstrahlung is the source of the inevitable background of each EDX measurement, contribute the characteristic X-rays the peaks in the measured energy spectrum. In the analysis one has to take care if *all* expected peaks of a material are present. If not, some overlapping peaks or peaks close to the considered energy can lead to the impression that a material is there that is not. Note that TEM-EDX measurements allow the investigation of the chemical composition of single nanoparticles. The results of EDX measurements are shown in section 5.3.1. For further reading is [53], upon which this section is based, a good source. Comprehensibly are neither of the instruments mentioned before practically suited for magnetic measurements, hence a SQUID-magnetometer, as described in the following section 3.3, is a more appropriate choice for magnetic characterization tasks.

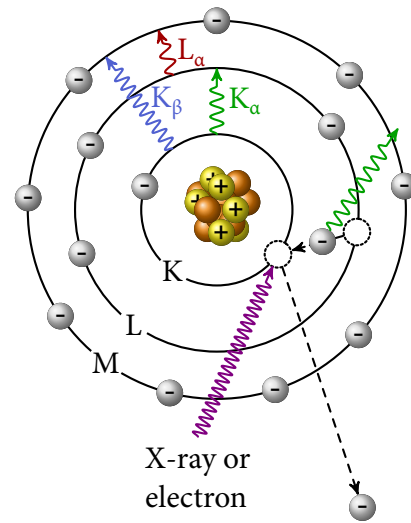


Figure 3.2.: Schematic drawing of the principle exploited for EDX measurements.

3.3. Superconducting Quantum Interference Device magnetometer (SQUID-magnetometer)

After the postulation of the JOSEPHSON effect in 1962 [54] the sensitive SQUID-magnetometer was invented in 1964 [55]. It is widely used to characterize magnetic nanoparticles.

There are problems using two weak JOSEPHSON contacts forming a dc-SQUID, viz a large offset by the applied field and a bad signal-to-noise ratio due to the sensing of first order gradients, exempli gratia introduced by a slightly unstable applied field. Hence the SQUID does not measure the magnetic flux directly, but a four winding, noise reducing second order gradiometer pickup-coil. Thus moving the sample through the pickup-coil induces a current proportional to the samples' magnetic moment. Due to the second order gradiometers structure neither offsets like static applied fields nor linear gradients of external fields contribute to this current. The pickup-coil generated current is compensated by a feedback coupled, »current-nulling« external source, such that the rf-SQUID in the magnetically shielded SQUID detection unit always »sees« the same flux.

data recording with the SQUID

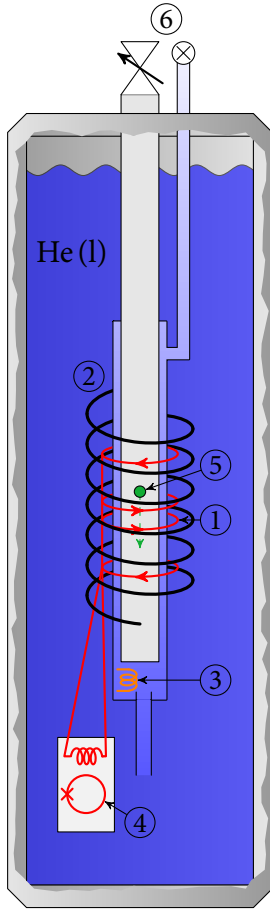


Figure 3.3.: Schematic illustration of the used SQUID-magnetometer. ① shows the pickup coil, ② the superconducting magnet coil, ③ the heater above the vent to the liquid helium reservoir, ④ the shielded rf-SQUID, ⑤ the movable sample and finally ⑥ the valves.

This avoids for example screening currents that occur if a »flux-nulling« approach would have been chosen [56]. When the sample is moving up respectively down an alternating current is induced in the pickup-coil, thus resulting in an alternating SQUID feedback current, allowing for determination of the samples' magnetic moment. It should be noted that this kind of experimental setup only detects the component of the magnetic moment that is *parallel* to the gradiometer axis. Another advantage of the SQUID-magnetometer used is its ability to heat the superconducting circuit of the pick-up coil if the applied field changes, thus eliminating eventually remaining currents. In figure 3.3 the schematic structure of a typical SQUID-magnetometer, as was used in this thesis, is shown. Around the helium reservoir is a vacuum isolated liquid nitrogen bath, that again is isolated via a vacuum chamber from the surrounding environment. Additionally to what is already explained in the caption of figure 3.3 it is noteworthy that the cylinder directly surrounding the sample chamber contains an adjustable helium gas flow that cools the sample to the desired temperature. If this cylinder gets pumped it is possible to achieve temperatures below 2 K.

For measurements that include an alternating magnetic field superimposed on a static, constant magnetic field (that in some cases can be chosen to be zero) the movement of the sample is unnecessary, as the time-dependency of the induced magnetic moment in the sample causes the induction of a current in the pickup-coil. If the frequency of the applied alternating magnetic field is low enough, one finds that, for the induced mo-

$$M_{ac} = \frac{dM}{dH} H_{ac} \sin(\omega_{ac} t) \quad (3.1)$$

holds true. Note that the susceptibility $\chi = dM/dH$ is the most relevant quantity in typical alternating magnetic field measurements. For higher frequencies however,

equation (3.1) is no longer valid, as dynamic processes prevent the samples' induced ac moment to follow the dc magnetisation. Consequently one can introduce the magnitude of the susceptibility $|\chi|$ and the correlated phase shift φ_{ac} , or an in-phase, real part of the susceptibility denoted by χ' and an imaginary, out-of-phase part denoted by χ'' . These representations are related by

$$\chi' = |\chi| \cos(\varphi_{ac}) \quad |\chi| = \sqrt{\chi'^2 + \chi''^2} \quad (3.2a), (3.2b)$$

$$\chi'' = |\chi| \sin(\varphi_{ac}) \quad \varphi_{ac} = \arctan\left(\frac{\chi''}{\chi'}\right). \quad (3.3a), (3.3b)$$

For low frequencies $\chi \approx |\chi| \approx \chi'$. For this paragraph see [44].

The used SQUID-magnetometer was a Quantum Design MPMS XL7, see figure 3.3, with an operational temperature range from 1.8 K to 400 K up to a magnetic field of 7 T, frequencies for ac measurements can be varied from 10 mHz to 1.5 kHz. Further information about the physical background can be found in [34, 57–59] and about the utilized SQUID-magnetometer in [60]. As the TEM described in section 3.1 as well as the SQUID described within this section lack the possibility to identify the material species that is present within a sample that should be scrutinized, another gauge that can fulfill this requirement, the X-ray powder diffractometer, is described succeedingly in section 3.4.

background information on the used SQUID

3.4. X-ray powder diffractometer

In 1912 VON LAUE et al. [61] discovered that X-rays »see« crystalline substances as diffraction gratings. To make use of these findings, a diffractometer is necessary. The modus operandi of an X-ray powder diffractometer can be summarized as follows. Initially an electron source, for example a sufficiently heated filament, gets its electrons accelerated towards a target, whereupon the X-rays are generated by the impacting electrons. Some kind of a filter is necessary to get monochromatic X-rays. The monochromatic X-rays are then collimated and hit the sample. Thereafter the X-rays are measured by an X-ray detector.

modus operandi of an X-ray powder diffractometer

Via sample and detector rotation it is possible to find the angles upon which constructive interference – complying to BRAGGS law [62],

$$n_{do}\lambda_B = 2d_{lp} \sin(\vartheta), \quad (3.4) \quad \text{Braggs law}$$

in which $n_{\text{do}} \in \mathbb{N}_+$ is the number specifying the diffraction order, λ_{B} is the wavelength of the X-rays, d_{lp} is the length between parallel lattice planes¹ and ϑ is the angle between the X-rays and the lattice plane – occurs. Consequently the measurement of a randomly oriented nanoparticle powder which is measured for all relevant $2\theta_{\text{B}}$ angles contains the complete information about the occurring diffractions patterns, showing a peak for the angles satisfying equation (3.4).

This measurement tool can thus be used to determine the lattice constant for each measured peak via large available databases [63], such that different crystalline species found within the nanoparticles can be detected. Furthermore it is possible to relate the broadening of the peaks to the size distribution of the crystallites. Keep in mind that the crystallite size does not necessarily match the nanoparticle size. For this section see [64]. While this method is mainly used for the determination of the occurring species respectively the length between parallel lattice planes, it is of no use to scrutinize resonance patterns in the nanoparticles. Therefore the methodology of a X band ESR spectrometer capable of this investigation is summarized in section 3.5.

usecases of X-ray powder diffractometry

3.5. X band ESR spectrometer

The electron spin resonance (ESR, alternatively labeled electron paramagnetic resonance, electron paramagnetic resonance (EPR)) is usually viewed in a scheme involving the electrons spin hamiltonian

Explication of electrons spin hamiltonian

$$\hat{\mathcal{H}}_{\text{es}} = -\mu_{\text{B}}\mu_0 \sum_i g \vec{H}_{\text{ext}} \cdot \vec{S}_i + J \sum_{i < j} \vec{S}_i \cdot \vec{S}_j + \sum_i (\mathcal{D} S_{z(i)}^2 + \mathcal{F}(S_{x(i)}^2 - S_{y(i)}^2)) + \hat{\mathcal{H}}_{\text{at}}, \quad (3.5)$$

wherein g is the LANDÉ factor, \vec{S}_i represents the i th spin, J the isotropic exchange integral, \mathcal{D} and \mathcal{F} the anisotropy constants and $\hat{\mathcal{H}}_{\text{at}}$ subsums additional terms like, for example, dipole-dipole interaction terms. For a rough understanding of the modus operandi of a ESR spectrometer it is sufficient to examine the first term in equation (3.5), that shows the influence of the ZEEEMAN splitting. The ZEEEMAN splitting is caused by the different directions that \vec{S}_i can take, $|\uparrow\rangle$ respectively $|\downarrow\rangle$. Consequently the ESR resonance condition that is met with microwave radiation to obtain a driven transition reads

$$\Delta E_{|\uparrow\rangle-|\downarrow\rangle} = -g \frac{\mu_{\text{B}}}{\mu_0} H \stackrel{!}{=} h\nu_{\text{mw}}, \quad (3.6)$$

¹Not necessarily equivalent to the lattice constant λ_{lat} .

with h being PLANCKS constant and ν_{mw} the (if the condition is met resonant) microwave frequency.

The spectrometer that measures a sample typically applies a constant microwave frequency and varies H , such that an absorption peak is observed if equation (3.6) is fulfilled. Theoretically it would also be possible to keep H constant and vary the frequency. Often a setup is used wherein the microwave frequency is fixed within the X band, that lies at approximately 10 GHz. With these measurement tool it is possible to investigate the electronic structure of nanoparticles.

For this section confer [65, 66]. After the brief discussion of the nanoparticles, the measurement techniques and tools is the next step the consideration of more sophisticated magnetism models and their implementation as described in chapter 4.

modus operandi of
an ESR spectrometer
in practice

4. Analysis and computer-based implementation of various magnetism models

As the main interesting magnetic features expected to be found in the NiTi nanoparticles were superparamagnetism, single and multi domain ferromagnetism, models that are capable to describe the anticipated behaviour were implemented in *Mathematica*. Consequently the theory of each of the corresponding models is explained, as well as a part describing the usage of the *Mathematica* implemented model. Difficulties and the corresponding solutions that were met while coding are mentioned thereafter. The complete commented *Mathematica* code can be found in appendices B to D.

A model based upon the STONER-WOHLFARTH model described in section 4.2 that can be used to describe superparamagnetic behaviour is given by [10] and is described in the following section 4.1.

4.1. Langevin-model and other approaches towards superparamagnetism

The classic paramagnetic theory by LANGEVIN follows from the limit of the quantum theoretical description given by

$$M_{\text{sat}} \lim_{J \rightarrow \infty} \mathcal{B}_J(\xi) = M_{\text{sat}} \mathcal{L}(\xi) = M_{\text{sat}} \left(\coth(\xi) - \frac{1}{\xi} \right), \quad (4.1)$$

superparamagnetic
Langevin equation

with $\mathcal{B}(\xi)$ the BRILLOUIN, $\mathcal{L}(\xi)$ the LANGEVIN function and $\xi = \mu_0 m H / (k_B T)$ as the ratio of magnetic to thermal energy [67]. As superparamagnetic behaviour is similar to paramagnetic behaviour, the LANGEVIN function is often used to model superparamagnetic $m(H)$ curves, that the following subsection will investigate more closely.

4.1.1. Theoretical background

A method often used to refine the accuracy of pure LANGEVIN fits is given by additionally taking the size distribution into account [10]. This leads to

superparamagnetic
integralfunction

$$m(H, T) = N \int_0^{\lambda_{\text{spm}}} \frac{\tilde{\xi} k_B T}{\mu_0 H} \mathcal{L}(\tilde{\xi}) \text{pdf}(D_{\text{mag}}) dD_{\text{mag}}, \quad (4.2)$$

wherein $\tilde{\xi} = \mu_0 M_{\text{sat}} \pi D_{\text{mag}}^3 H / (6k_B T)$ and pdf stands for the probability density function,

lognormal probability
density function

$$\text{pdf}(D) = \frac{1}{wD\sqrt{2\pi}} \exp\left[-\frac{1}{2} \left(\frac{\log(D/D_m)}{w}\right)^2\right]. \quad (4.3)$$

If this fitting routine is used as sole method to determine the particle size distribution, problems arise due to the ambiguity of the fitted nanoparticle size distribution, as there are many distributions that show no considerable deviation in reproducing the $m(H)$ curve. Consequently, it is desirable to find more ways to enhance the unambiguity of the fitting procedure.

Such ways are given by TAMION et al. [10]. They found a semianalytical model based on the STONER-WOHLFARTH theory which is introduced in section 4.2.1. To return to the semianalytical model, the data obtained via ZFC-FC measurements can be compared to the curves predicted by

semianalytical model
for ZFC-FC curves

$$m_{\text{ZFC}}(T) = N \int_0^{\lambda_{\text{spm}}} M_0 V_{\text{mag}} \left[\exp(-\nu(T)\delta t(T)) + \frac{K_{\text{eff}} V_{\text{mag}}}{k_B T} (1 - \exp(-\nu(T)\delta t(T))) \right] \text{pdf}(D_{\text{mag}}) dD_{\text{mag}} \quad (4.4)$$

for the ZFC part of the curve and

$$m_{\text{FC}}(T) = N \int_0^{\lambda_{\text{spm}}} M'_0 V_{\text{mag}} \left[\exp(-\nu(T)\delta t(T)) + \frac{\mu_0 m_{\text{sat}}^2 H}{3k_B T} (1 - \exp(-\nu(T)\delta t(T))) \right] \text{pdf}(D_{\text{mag}}) dD_{\text{mag}} \quad (4.5)$$

for the FC curve. Note that $\delta t(T) = k_B T (K_{\text{eff}} \partial T / \partial t)^{-1}$ represents a characteristic time respecting the temperature sweeping rate and the switching frequency is given by $\nu(T) = \nu_0 \exp(-K_{\text{eff}} V_{\text{mag}} / (k_B T))$. If equations (4.2), (4.4) and (4.5) are fitted simultaneously the error in the nanoparticle size distribution is greatly reduced and thus allows a unambiguous determination of the particle size distribution.

It is of great importance that the nanoparticles do not interact, as a small influence of interparticle interactions suffices to prevent a successful fit [10], even for a single fit to equation (4.2). As none of the NiTi nanoparticles exhibited pure superparamagnetic behaviour¹ the fitting procedure did not succeed in finding a decent fit. Therefore pure Ni nanoparticles produced via the sol-gel dip-coating method that are separated enough to minimize interparticle interactions were used to demonstrate the feasibility of this model. Consequently, equation (4.2) was implemented in *Mathematica* and is briefly explained in the next subsection, as it is useful to test for interparticle interactions and may be of use in further research in this area.

problems of the semi-analytical model

4.1.2. Mathematica implementation and challenges

The code of the *Mathematica* implementation of equation (4.1) and equation (4.2) can be found in appendix B and allows the fitting of superparamagnetic behaviour. It can be easily modified to simulate superparamagnetic behaviour. Figure 4.1 shows some simulation examples. In figure 4.1a the influence of the median diameter on the superparamagnetic behaviour is elucidated. As one can see increases the magnetic moment with an increasing median of the nanoparticles. This is expected as the amount of nanoparticles was kept constant, such that an increasing median diameter of the nanoparticles relates to more atoms that consequently contribute to the overall magnetic moment.

variation of the median

Basically the same argument explains figure 4.1b, in that the dispersion w was varied. The amount of nanoparticles is again kept constant, as well as the median diameter, consequently a larger dispersion leads to more »big« nanoparticles that contain more atoms contributing to the magnetic moment.

variation of the dispersion

In figure 4.1c the saturation magnetisation was varied. As a larger saturation magnetisation is equivalent to a larger magnetic moment per volume, a constant volume, as here, thus inevitably leads to a larger total magnetic moment.

variation of the saturation magnetization

¹All showed at least a small hysteresis opening and thus partly ferromagnetic behaviour. Furthermore are the nanoparticles embedded in eicosane probably clustered together and hence not far enough from each other to completely suppress interparticle interactions, see section 5.2.

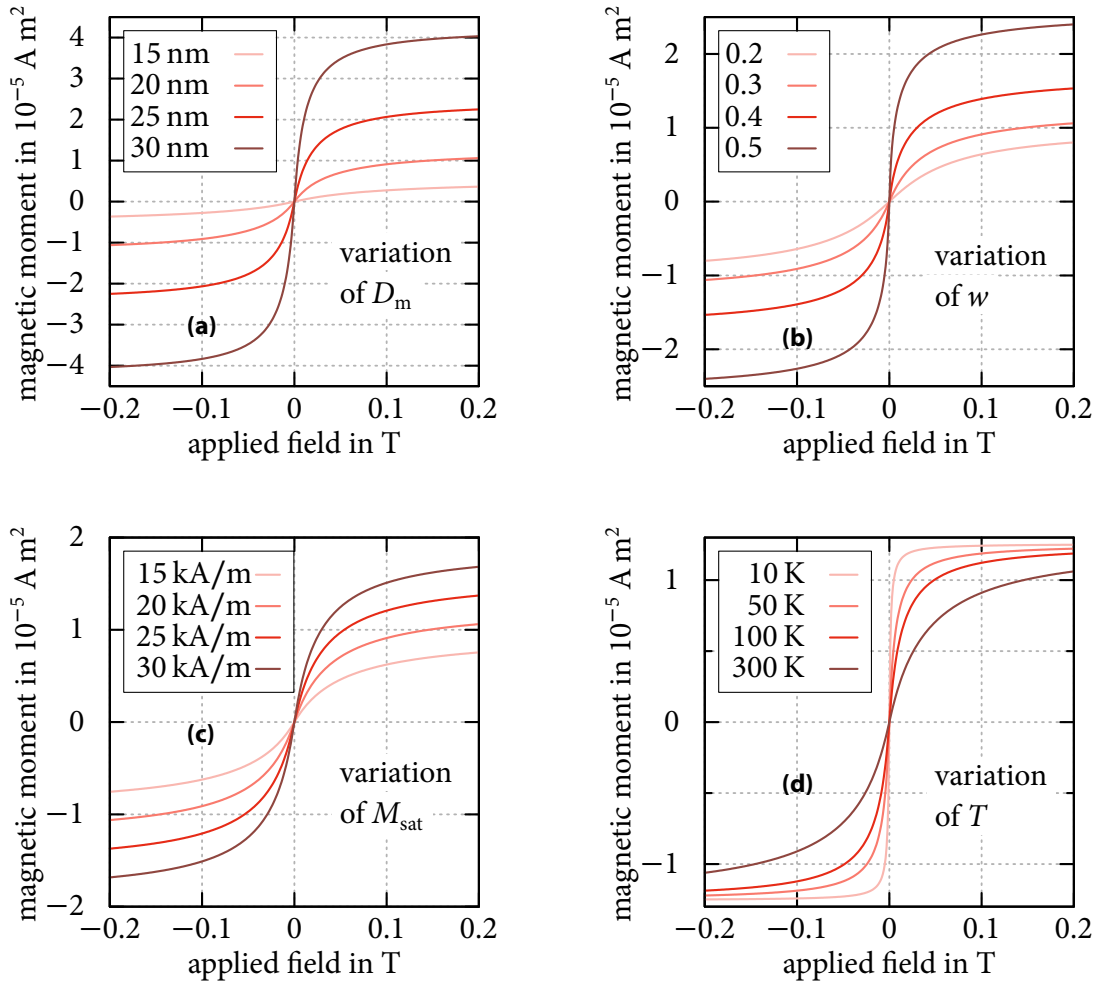


Figure 4.1.: Simulations of equation (4.2) with a variation of **(a)** D_m (raw data: \square), **(b)** w (raw data: \square), **(c)** M_{sat} (raw data: \square) and **(d)** T (raw data: \square). As one can see, lead the increasing amounts of available atomic magnetic moments in **(a)** and **(b)** to a larger total magnetic moment. The increase in the total magnetic moment with increasing magnetisation seen in **(c)** is due to the increased magnetic moment density at a constant volume, while in **(d)** the thermal fluctuations that grow with temperature cause a shift towards larger field of the field necessary for saturation of the total magnetic moment.

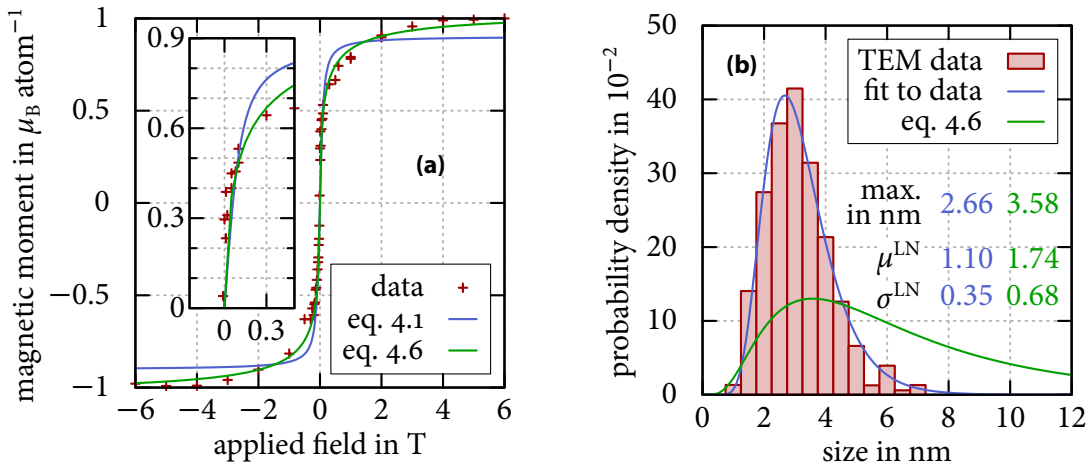


Figure 4.2.: The measurement of the magnetic moment per atom shown in (a) was done on pure Ni nanoparticles produced with the sol-gel dip-coating technique. The blue respectively green line represent fits to the simple LANGEVIN fit, equation (4.1), and to the extended LANGEVIN equation, equation (4.6). While the extended LANGEVIN equation clearly »fits« better to the data (see inset), it still seems to systematically underestimate the magnetic moment below 0.3 T, which may be due to time restrictions on the fitting procedure. The nanoparticle size distribution illustrated in (b) was obtained with a TEM, with both the lognormal fit (for the meaning of μ^{LN} and σ^{LN} see equation (5.1)) to the TEM data as well as the size distribution obtained from the extended fit in (a). Although the maxima of the size distributions are close to each other, the width varies considerably, which shows the limitedness of such an attempt to extract the size distribution from $m(H)$ measurements.

Figure 4.1d shows that for larger temperatures the saturation magnetic moment is reached at higher applied fields. This can be accounted to growing thermal fluctuations that prohibit alignment of spins at lower fields.

variation of the temperature

A variation of N was omitted as N works solely as a scaling factor and thus grants no further insights in the physics.

Exemplarily, the fit of purely superparamagnetic, noninteracting Ni nanoparticles produced with the sol-gel method is shown in figure 4.2a. In figure 4.2b the measured particle size distribution as well as the theoretical particle size distribution obtained from the extended LANGEVIN fit are shown. Table 4.1 shows a comparison

Table 4.1.: Comparison of the measured values specifying the lognormal particle size distribution of Ni nanoparticles produced by the sol-gel method as described in section 2.1.2 to the values obtained by fitting the size distribution dependent $m(H)$ curve. See equation (5.1) for the meaning of μ^{LN} and σ^{LN} .

	Measured	simple LANGEVIN fit	extended LANGEVIN fit
μ^{LN}	1.10	—	1.74
σ^{LN}	0.35	—	0.68
adj. R^2	—	0.971	0.981

of measured values and values from the fitting procedure respecting the nanoparticle size distribution via an extended LANGEVIN fit. As one can see there is quite a discrepancy between the actually measured particle size distribution and the data obtained via fitting, although the maximum of the particle size distribution obtained by a fit to the $m(H)$ curve is less than 1 nm bigger than the one of the fit to the TEM data (3.58 nm to 2.66 nm). This probably could have been accounted by the combined triple fit of equations (4.2), (4.4) and (4.5), but no ZFC-FC curves were available for these nanoparticles. Nonetheless, the fit that takes the size distribution into account is clearly better than the simple LANGEVIN fit, as can also be seen via the coefficient of determination R^2 . As an increasing amount of fitting variables *always* increases R^2 , a good comparison of R^2 for different fit functions needs to adjust for the influence contributed by the number of fitting variables. Therefore the corresponding adjusted R^2 values were calculated for the simple and the extended LANGEVIN fit, as can be seen in table 4.1. This indicates that the better fitting of the extended LANGEVIN fit is indeed theoretically better and R^2 increases not due to »overfitting«.

However, it should be noted that below 0.3 T the extended fit seems to systematically underestimate the magnetic moment per atom. A possible cause may be that not the global, but rather a local minimum was found and the fitting algorithm got stalled there. Note that the large computational power necessary for this fit limits the amount of iterations that could be taken². Note further that due to the nonlinear nature of the fitting procedure parallelization of this task is not possible.

Notably one problem was encountered while the computation was running –

²Over 10 h are necessary for a single fit with higher resolution.

comparison of the fit results of equation (4.6) to TEM measurements of Ni nanoparticles

discussion of the shortcomings of the model respectively the implementation

the occurrence of under-/overflows. This problem was circumvented by renorming D_m , such that it was roughly on the order of 1. Furthermore, as the available data was given in BOHR magnetons per atom, the prefactor N was used as a scaling factor, as the more naïve and intuitive approach to get rid of N and replace it with $V_m/(N_A \langle V \rangle \mu_B)$ does not yield sensible results. Additionally, the external field had to be scaled down by 10^4 , but this does not influence the particle size distributions outcome, as this prefactor is irrelevant if M_{sat} gets scaled up by a factor of 10^4 and N down by a factor of 10^4 . Consequently, equation (4.2) was renormed to

$$m(H, T) = \frac{Nk_B^{4/3} M_{\text{sat}} \pi}{6} \int_0^{\lambda_{\text{spm}}} \frac{\hat{\xi} k_B T}{\mu_0 H} \mathcal{L}(\hat{\xi}) \text{pdf}(D_{\text{mag}}) dD_{\text{mag}} \quad (4.6) \quad \text{fitting function}$$

with $\hat{\xi} = 10^{-4} B M_{\text{sat}} \pi D_{\text{mag}}^3 / (6T)$. Equation (4.6) is the equation that was finally used in the *Mathematica* program. As a next step the STONER-WOHLFARTH model is explicated, as it is able to further shed light on single domain ferromagnetism.

4.2. Stoner-Wohlfarth-model

As the extended LANGEVIN model presented in the previous section is solely capable of describing superparamagnetic behaviour, a model that allows the description of small, ferromagnetic nanoparticles – as they are often encountered if metallic nanoparticles at low diameters are studied – is given subsequently.

4.2.1. Theoretical background

The STONER-WOHLFARTH-model (SW model) [11], also called the coherent rotation model, treats a ferromagnet as a lone magnetic moment, assuming an infinite exchange interaction between all spins resulting in them being parallel at any given time (for this subsection confer [68–72]). It is a simple model of single domain ferromagnetism, inherently not taking into account influences of other domains and inhomogeneities. Thus it is only relevant to nanoparticles at length scales below a critical diameter λ_{sd} , above which multi domains are energetically favoured over single domains, and above another critical diameter λ_{spm} , below which superparamagnetic behaviour is observed. The theory is typically applied to prolate, ellipsoidal particles exhibiting an uniaxial anisotropy (also called STONER-WOHLFARTH-particles, SW particles).

brief introduction to the SW model

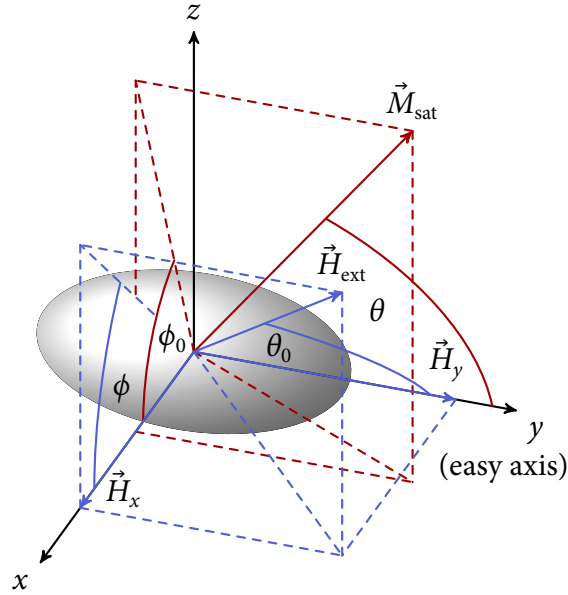


Figure 4.3.: Schematic drawing of an ellipsoidal, grey SW particle depicting the relevant angles for magnetic calculations. Herein the y -axis is the easy axis of the SW particle, \vec{H}_{ext} represents an external applied field and \vec{M}_{sat} stands for the saturation magnetisation. θ is hereby the angle between the easy axis and the saturation polarization moment, θ_0 the angle between the easy axis and the applied external field \vec{H}_{ext} . ϕ stands for the angle between the projection of \vec{M}_{sat} onto the xz -plane and the x -axis, ϕ_0 symbolizes the angle between the projection of \vec{H}_{ext} onto the xz -plane and the x -axis. \vec{H}_i is the projection of \vec{H}_{ext} onto the i -axis with $i \in \{x, y\}$.

The magnetocrystalline energy density (if higher orders shall be taken into account, choose $i' > 0$) of a SW particle originating from spin-orbit coupling and crystal-field interaction or the interatomic dipole-dipole interaction can be written as

$$\text{magnetocrystal-} \quad W_{\text{mc}} = K \sum_{i=0}^{i'} \frac{\sin(\theta)^{2(i+1)}}{2^i} \quad (4.7)$$

$$\text{line energy density} \quad = -K \cos^2(\theta) + \mathcal{O}(\cos^4(\theta)). \quad (4.8)$$

In it the influence of the different crystallographic axes on the magnetisation processes – depending on the direction of the external field – is manifested [67]. Note that the offset K that would arise in equation (4.8) as a consequence of the 1 =

$\sin^2(x) + \cos^2(x)$ identity used to obtain this equation can be neglected due to its constant nature. Furthermore, the magnetostatic energy density is defined as

$$W_{\text{ms}} = -\vec{M}_{\text{sat}} \cdot \vec{H}_{\text{ext}} \quad (4.9)$$

magnetostatic energy density

$$= -M_{\text{sat}} H_{\text{ext}} \left(\sin(\theta_0) \sin(\theta) \cos(\phi_0) \cos(\phi) + \sin(\theta_0) \sin(\theta) \sin(\phi_0) \sin(\phi) + \cos(\theta_0) \cos(\theta) \right). \quad (4.10)$$

Thus adding equation (4.8) and equation (4.10) and substituting $K = 0.5M_{\text{sat}}H_K$ with H_K the anisotropy field yields the total energy density, that in spherical coordinates reads

$$W_{\text{ges}}^{\text{SW}} = 0.5M_{\text{sat}} \left[-H_K \cos^2(\theta) - 2H_{\text{ext}} \left(\sin(\theta_0) \sin(\theta) \cos(\phi_0) \cos(\phi) + \sin(\theta_0) \sin(\theta) \sin(\phi_0) \sin(\phi) + \cos(\theta_0) \cos(\theta) \right) \right]. \quad (4.11)$$

total energy density

As the condition $\partial_\phi W_{\text{ges}}^{\text{SW}} = 0$ arising from energy minimization considerations yields $\phi = \phi_0$ equation (4.11) can be simplified without loss of generality to the angular two-dimensional equation

$$W_{\text{ges}}^{\text{SW}} = 0.5M_{\text{sat}} \left(H_K \cos^2(\theta) + 2H_{\text{ext}} \cos(\theta_0 - \theta) \right). \quad (4.12)$$

simplification of the total energy density

For an illustration of the angles see figure 4.3. Finding the minimum of equation (4.12) for θ results in the angle θ_{res} which the system will approach in equilibrium, as a repercussion of the antagonistic preferences of the nanoparticle to minimize the magnetostatic respectively the magnetocrystalline energy, correspond to their tendency to align along the easy axis respectively the external applied field.

The equations for finding the minima of equation (4.12), $\partial_\phi W_{\text{ges}}^{\text{SW}} = 0$ as well as $\partial_\phi^2 W_{\text{ges}}^{\text{SW}} > 0$, can be rewritten resulting in the parametric equations

$$H_x = -H_K \sin^3(\theta) \quad (4.13)$$

$$H_y = H_K \cos^3(\theta). \quad (4.14)$$

It has to be noted that in equations (4.13) and (4.14) the *bigger as* sign was converted into an *equal* sign, to be able to display the border between the two solution area and the one solution area. Further it should be taken into account that by finding

Stoner-Wohlfarth astroid

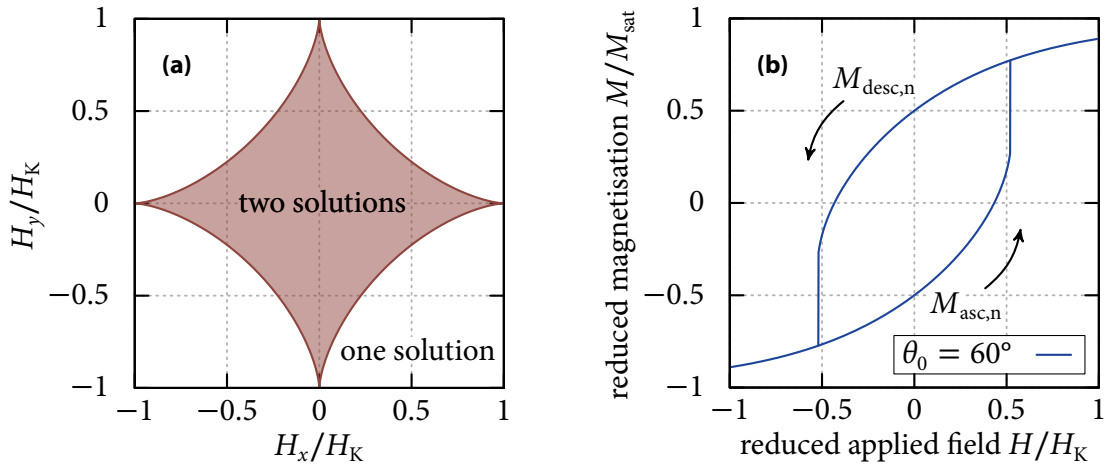


Figure 4.4.: (a) shows the typical STONER-WOHLFARTH-astroïd, whereby H_i/H_K represents the projected external field onto i with $i \in \{x, y\}$ normalized to the anisotropy field H_K , that is the minimum field capable of flipping the saturation magnetisation over the energy barrier imposed by the magnetic anisotropy. The area containing two solutions represents solutions for which hysteretic behaviour can be anticipated. The astroïd can be constructed using the conditions for energetic minima, $\partial_\theta W_{\text{ges}}^{\text{SW}} = 0 < \partial_\theta^2 W_{\text{ges}}^{\text{SW}}$. (b) depicts an example curve of the simple SW model with $\theta_0 = 60^\circ$. $M_{\text{asc},n}$ respectively $M_{\text{desc},n}$ represent the ascending respectively the descending branch of the normalized magnetisation.

the minima of equation (4.12) with respect to θ one obtains up to four solutions, wherefore up to two solutions have physically meaningful. As a consequence it is possible to construct the so-called STONER-WOHLFARTH-astroïd (see figure 4.4a) that separates regions with only one *physical* solution (hence two *mathematical* solutions) for $\theta = \theta_{\text{res}}$ from regions with two *physical* solutions (hence four *mathematical* solutions). Thus a bifurcation of the energy minima is taking place at its surface, consequently fixing the typical SW model hysteresis jumps there.

In figure 4.5a is the geometrical construction of the angles between the ascending respectively the descending branch of the magnetisation vector with the easy axis elucidated. The light gray dashed line shows how the orientation of, as an example, the magnetisation of the ascending branch for a given external applied field can be constructed. The saturation magnetisation vector of the ascending branch results from the tangent of the border of the STONER-WOHLFARTH-astroïd that goes

geometrical construction of the angles that are relevant for hystereses

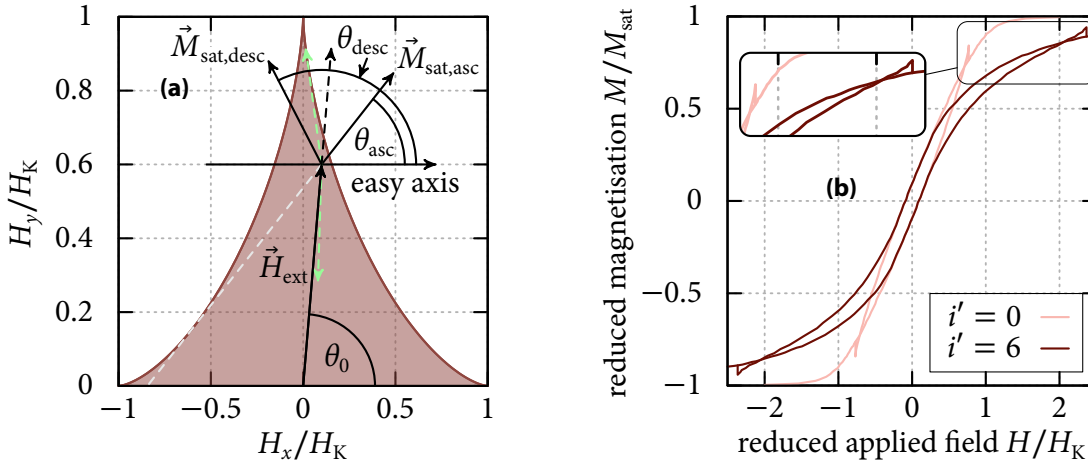


Figure 4.5.: (a) shows exemplarily how a crossover occurs in the standard SW model. θ_{asc} is the angle between the easy axis and the saturation magnetisation of the ascending branch of the hysteresis and θ_{desc} the angle between the easy axis and the saturation magnetisation of the descending branch. Thus the magnetisation parallel to the external field can be calculated with equation (4.15). For a sufficiently big external field and a sufficiently big angle θ_0 , here $\theta_0 \approx 80.5^\circ$, the ascending branch's magnetisation parallel to the external field, $M_{\text{asc}}^{\text{SW}}$, yields a *bigger* value than the corresponding $M_{\text{desc}}^{\text{SW}}$, thus resulting in a crossover shown in (b). Picture inspired by [71]. (b) shows the magnetisation of a SW particle in dependence of the applied field normalized to the anisotropy field [71]. The inset shows the crossovers. The shown i' values correspond to the upper limit of the sum in equation (4.7).

through the tip of the external applied field vector. The dashed green lines represent further solutions to the energy minimization problem, but these are unstable. For uniaxial anisotropy the solutions that bear the smallest tilting towards the easy axis are always stable³. For a explanation of the geometrical power of astroïds see [72].

The hysteresis is obtained by taking the projection of the saturation magnetisation onto the external field direction for all H_{ext} values of interest, thus

$$M^{\text{SW}} = \cos(\theta_0 - \theta_{\text{res}}) \quad \text{with } 0 < \theta_{\text{res}} < 90^\circ \text{ or } \theta_{\text{ht}} < \theta_{\text{res}} < 180^\circ, \quad (4.15)$$

³To clarify this with an example from figure 4.5a: $\theta_{\text{desc}} \approx 136^\circ$ features a *smaller* tilting towards the easy axis than the upper, dashed, green arrow with $\theta_{\text{uga}} \approx 105^\circ$.

contruction of hys-
teresis with the pre-
viously calculated
angles

wherein the angle that the tangent of the astroïd in the point where the elongation of \vec{H}_{ext} intersects the surface of the astroïd forms with the easy axis is defined such that

$$\theta_{\text{ht}} = 180^\circ - \arctan(\tan(\theta_0)^{1/3}) \quad (4.16)$$

holds true. This allows to restrict the solution space such that there are only the two physically correct solutions remaining. An example of such a resulting hysteresis (without crossover) can be found in figure 4.4b using an angle of $\theta_0 = 60^\circ$ between the particle's easy axis and the external field. The arrows show how the magnetisation moves through the hysteresis cycle.

considerations on
the crossover case

Figure 4.5a shows the solution for the special, crossover case in which the magnetization of the ascending branch $M_{\text{asc}}^{\text{SW}}$ is herefore *bigger* than the one of the descending branch $M_{\text{desc}}^{\text{SW}}$. Crossovers always occur if the magnetocrystalline energy density shows a point of inflection for $\theta \in [0, \pi/2]$, as is the case with equation (4.8). For equation (4.8) the angle, above which crossover behaviour occurs, can be calculated via

$$\theta_{\text{co}} = \frac{1}{2} \arccos\left(\frac{-2}{\sqrt{5}}\right). \quad (4.17)$$

Taking higher orders of $\sin(\theta)$ into account leads to a shift of the crossover point to higher fields, see figure 4.5b, but due to inflection points always occurring within equation (4.7) there will always be crossover points (confer [71]).

So far this model does not account for variations of, for example, the nanoparticle size distribution. Consequently, more parameters are included in the extended equation for the critical field discussed in the next subsection.

4.2.2. Extended equations for the critical field

differences between
 H_c and H_{cr}

In the beginning it is crucial to note that in the SW model the coercivity H_c is generally *not* the same as the critical field H_{cr} , *although* these terms are often mixed up in the literature. Whilst for low angles $H_c = H_{\text{cr}}$ holds true, there is an increasing difference for higher angles, as the critical field induced »jump« occurs *after* the magnetisation has passed the $M^{\text{SW}} = 0$ line. For an explanatory plot see figure 4.6.

To take the nanoparticles diameter as well as the temperature, the effective anisotropy and the angular dependency into account one has to modify the equation for the critical field, at which the switch from one solution space to the other one occurs.

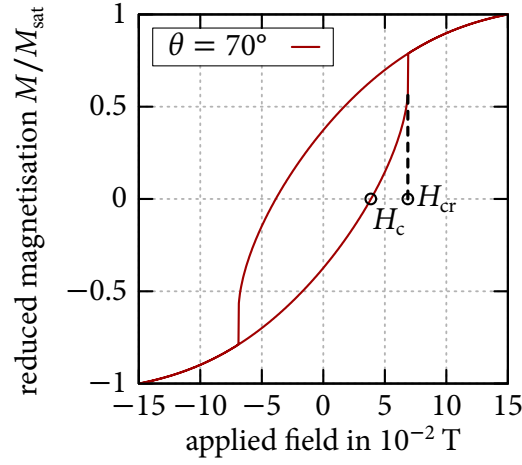


Figure 4.6.: Comparison of H_c and H_{cr} for a SW particle with $\theta = 70^\circ$ at $T = 2$ K. As $\theta > 45^\circ$, H_c is smaller than H_{cr} . For $\theta \leq 45^\circ$ the two fields are identical. Raw data:

This can be achieved by defining the critical size below which superparamagnetic behaviour eventuates via [73]

$$\lambda_{\text{spm}} = 2 \left(\frac{6 k_B T}{K_{\text{eff}}} \right)^{1/3}. \quad (4.18)$$

critical size for superparamagnetic behaviour

Subsequently the critical size for superparamagnetism can be utilized as a parameter in the definition of the size dependency of the coercive field as was done by [74], who used

$$H_{\text{crna}} = \begin{cases} 0 & \lambda^{\text{dia}} < \lambda_{\text{spm}} \\ -\frac{1}{2} H_K \left[1 - \left(\frac{\lambda_{\text{spm}}}{\lambda^{\text{dia}}} \right)^{3/2} \right] & \lambda^{\text{dia}} > \lambda_{\text{spm}} \end{cases} \quad (4.19)$$

size dependency of the coercive field

for the coercivity. Therefore, up to here, the nanoparticles diameter, temperature and effective anisotropy are taken into account. As [75] points out the coercive field can be combined with a function accounting for the angular dependency resulting in the *critical* field, as only at higher angles a discrepancy between the critical field and the coercivity occurs, such that a prefactor that diminishes with increasing angles should be sufficient to describe the critical field in terms of the coercivity.

Furthermore, if crossover behaviour shall be avoided, the formula for the angular dependency above θ_{co} has to be adjusted (confer [71]). Finally one obtains

final equation for the critical field in the Stoner-Wohlfarth model

$$H_{cr} = \begin{cases} \frac{H_{crna}}{([\sin(\theta_0)^{2/3}] + [\cos(\theta_0)^{2/3}])^{3/2}} & \theta_0 < \theta_{co} \\ -\frac{H_{crna} \cos(2\theta_0)}{\sqrt{2}} & \theta_0 > \theta_{co} \end{cases} \quad (4.20)$$

as an end result that contains the dependencies discussed above. Equation (4.20) is used in the corresponding *Mathematica* program explained in the next subsection.

4.2.3. Mathematica implementation

The actual *Mathematica* code that allows the simulation of hystereses according to the extended STONER-WOHLFARTH model can be found in appendix C.1. To give a short overview of the function a flowchart is depicted in figure 4.7, further information can be found in the appendix. Note that the reason for the inclusion of the possibility to restrict the possible angles that the nanoparticles can take with respect to the applied field is explained in detail in section 4.2.4.

As the SW model fitting that has been implemented in *Mathematica* is too long to show it here it can be found in appendix C.2. Therefore the use of the *Mathematica* function that allows the fitting of the hysteresis with only a subset of all possible angles θ is briefly explained. An interface that allows an easy configuration via

Mathematica function that can be used for fitting to the extended Stoner-Wohlfarth model

```
54 CompleteSWModelLoopFit[minval_, maxval_,
    stepsize_, FinenessOfLoop_,
    DataFileToUse_, FileLocation_,
    TemperatureInput_, KeffInput_,
    diameterstartvalue_, diameterendvalue_,
    diameterstepsize_,  $\mu_$ ,  $\sigma_$ ,
    latticeconstant_,  $\mu$ SaturationPerAtom_,
    Fcc_, Bcc_]
```

wherein all angles between *minval_* and *maxval_* are considered (discretized with *stepsize_*) is provided. *FinenessOfLoop_* sets the stepsize for the

description of the parameters that can be passed on to the *Mathematica* function

subsets. To clarify this consider the following example: `minval = 0.0`, as well as `maxval = 90.0`, `stepsize = 1.0` and `FinenessOfLoop = 10.0` are chosen, the loop would try to fit the subsets 0° to 90° , 10° to 90° , ..., 80° to 90° , 0° to 80° , ... - each subset understood as a superposition of hystereses calculated in 1° steps. `DataFileToUse_` specifies, as the name indicates, the data file containing the raw measured data. The data file is assumed to be saved in a `.dat` file, so the file ending has to be omitted. `FileLocation_` should be the name of the temporary files created, again with omitted file ending. While the fitting procedure runs the progress can be monitored by watching these temporary files. `TemperatureInput_` is the temperature at which the hysteresis measurement was performed. `KeffInput_` represents the effective anisotropy constant of the nanoparticles. `diameterstartvalue_`, also represented as $\lambda_{\text{start}}^{\text{dia}}$, stands for the beginning of the size interval that is taken into account. `diameterendvalue_`, or $\lambda_{\text{end}}^{\text{dia}}$, marks the end of this interval that is discretized with `diameterstepsizevalue_` or $\lambda_{\text{step}}^{\text{dia}}$. All diameter values have to be entered in units of nanometers. `$\mu_$` respectively `$\sigma_$` , also notated as μ^{LN} and σ^{LN} , are the parameters that form the log-normal probability density function. The `latticeconstant_` represents the nanoparticles material lattice constant λ_{lat} that has to be entered in units of meters. Furthermore the loop is supplied with `μ SaturationPerAtom_`, the saturation magnetic moment per atom μ_{satpa} . Finally `Fcc_`, face-centered cubic, and `Bcc_`, body-centered cubic, contain boolean values whose values depend on the type of structure the nanoparticles exhibit. In the end the fitting loop returns a message that states which starting and ending angle combination had the smallest error via the least squares method.

4.2.4. $\text{Co}_x\text{Ni}_{1-x}$ nanoparticles and fits

brief description of the system used

BOGANI et al. produced $\text{Co}_x\text{Ni}_{1-x}$ nanoparticles embedded in a silica thin film over silica slabs via the sol-gel method described in section 2.1.2. Note that these alloys exhibit a large anisotropic magnetoresistance and the heavily spin-orbit coupling Co atoms in Ni function as scattering barriers whose height depends on the spin, see figure 4.8a. If these nanoparticles are now irradiated with a laser, the dynamics of magnetisation change, such that consequently the width of the hysteresis obtained from magnetic circular dichroism measurements changes, depending on the wavelength.

Therefore, the following theoretical framework originally proposed by ELLIOTT and YAFET [76, 77] is helpful to understand the physical phenomena taking place

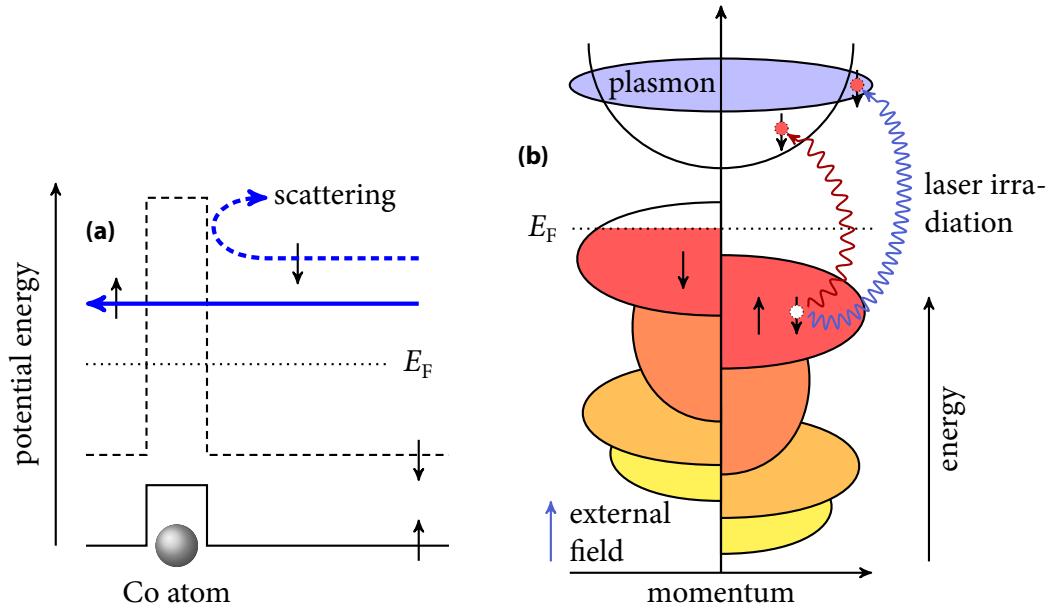


Figure 4.8.: (a) Spin dependent scattering of electrons. The dashed potential lines are relevant for electrons with spin down, while the solid black line of the potential energy is relevant for their spin up counterparts. A relevant amount of scattering events thus only occurs for electrons with spin down and only for these the ELLIOTT-YAFET mechanism can result in a flipping of the electron spin. (b) Schematic view of the density of states of a single nanoparticle with an applied field. The left band stands for the minority band, while the right band represents the majority band. Irradiation with a laser leads to the creation of a plasmon, such that these excited electrons can move collectively. Pictures from [1].

in the system. The ELLIOTT-YAFET theory explains the transport of momentum from an electron to the lattice by means of spin-orbit coupling. As the laser induced plasmon oscillations (collective electron oscillations) introduce a linear momentum in our system, a similar behaviour is expected. One can define the *dominant* spin-up respectively spin-down BLOCH states (due to a respectively a^* approximately unity) of the nanoparticles,

$$\Psi_{\vec{k},\uparrow} = (a_{\vec{k}}|\uparrow\rangle + b_{\vec{k}}|\downarrow\rangle) \exp(i\vec{k} \cdot \vec{r}) \quad \text{and} \quad (4.21)$$

$$\Psi_{\vec{k},\downarrow} = (a_{-\vec{k}}^*|\downarrow\rangle - b_{-\vec{k}}^*|\uparrow\rangle) \exp(i\vec{k} \cdot \vec{r}), \quad (4.22)$$



that arise due to the no longer commuting single-electron hamiltonian with the electron-spin operator \hat{S}_z [78]. As above said the spin-orbit coupling of the Co atoms enhances the height of the potential barrier for spins from the minority band, such that the discrepancy in the amount of scattering processes is nonneglectable, see figure 4.8a. FERMIS golden rule allows the determination of the actual transition rate, henceforth denoted by $\gamma_{\uparrow\downarrow}$. Due to the fact that the amount of electrons that take part in the plasmon oscillation depends on the optical oscillator strength $f(\lambda)$, the total reversal rate of spins is given by $\gamma_{sc} \propto f(\lambda) \gamma_{\uparrow\downarrow}$. Caused by the large surface to volume ratio of nanoparticles, the influence of this effect is important in the CoNi nanoparticle system, as it adds remarkably to the magnetic anisotropy.

To further clarify the processes involved, consider a single nanoparticle that is irradiated with a laser. Consequently, a plasmon is generated by lifting electrons from the valence band to an excited state, confer figure 4.8b, such that these electrons can move collectively. The plasmon induces an additional anisotropy, such that the directions the effective overall anisotropy can take are limited. As the laser light is linearly polarized, the directions the »effective easy axes« of randomly oriented nanoparticles can take with respect to the applied field are limited, such that the behaviour should be similar to that of nanoparticles that have a »forbidden« angular regime of θ . This is the reason why the simulation as well as the fitting procedure described in section 4.2.3 provide the option to limit the scope of angles that θ can occupy. Due to the wavelength depending absorption, different amounts of nanoparticle plasmons are generated. A broad plasmonic absorption peak is found at a wavelength of circa 370 nm which diminishes steadily towards higher wavelengths [1]. Since larger wavelengths excite less plasmons, the influence of the laser on the dynamics of the magnetisation is decreased. Therefore the coercivity *increases* for larger wavelengths, if the orientation of the laser polarisation with respect to the orientation of the external applied field leads to an *increase* of the *minimum* angle of the »effective easy axes«.

To examine if these findings can be mapped with an angularly restricted extended STONER-WOHLFARTH model the fitting routine described in section 4.2.3 was used to obtain a fit to the data shown in figure 4.9a. As one can see there is a big discrepancy between the coercivity that stems from the best fit and the coercivity that the actual data suggests. This is most likely caused by the lack of an adequate equation for the critical field, as the equation that was used, equation (4.20), does not describe effects of the ELLIOTT-YAFET mechanism that is thought to play a major role. Although an equation for the coercive field given by the ELLIOTT-YAFET mechanism is known [1], it does neither (directly) take the particle size distribution

introduction to Elliott-Yafet theory and application to our system

physical processes involved

comparison between coercivities obtained from fitting and from experimental CoNi data

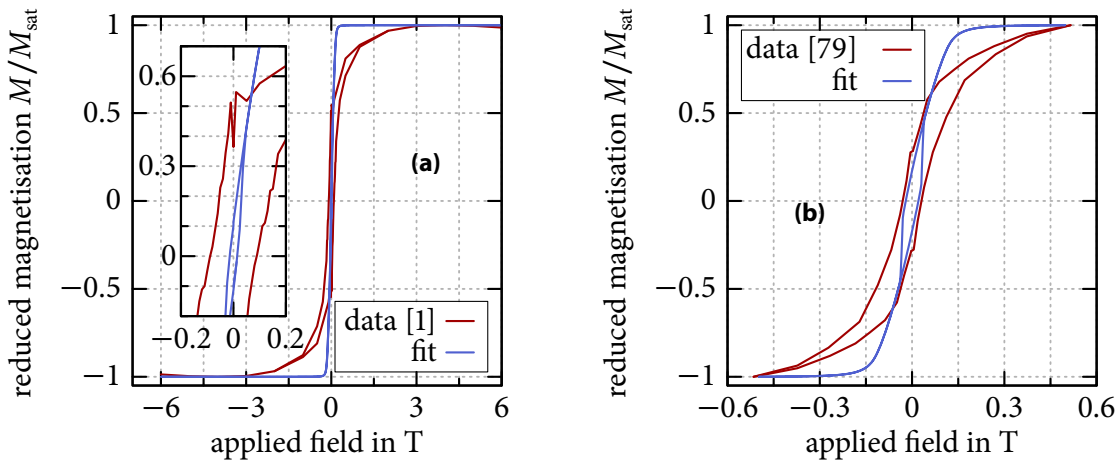


Figure 4.9.: Fits of the angularly restricted STONER-WOHLFARTH model to data from (a) $\text{Co}_{50}\text{Ni}_{50}$ [1] and (b) Fe nanoparticles [79]. The coercivity of the simulated hysteresis in (a) is far off the experimental value, most likely due to the equation for the critical field that does not account for the ELLIOTT-YAFET mechanism. While the fit in (b) is bad at predicting the shape of the curve, it does predict the coercivity reasonably well given the fact that the system should not be angularly restricted, thus indicating that the extended equation for the critical field, equation (4.20), is not per se wrong, but rather ill-suited for the $\text{Co}_{50}\text{Ni}_{50}$ system due to the reasons stated above.

into account nor is it clear if this equation can be combined with a prefactor that depends on the angle to correctly reproduce actual physical behaviour.

As a prove that the coercivity is predicted correctly for other nanoparticle systems, data from [79] was taken and fitted analogously, see figure 4.9b. While the coercivity matches quite good between the experiment and the data, the rest of the fitted curve is far from being close to the experimental data, but this is expected, as an angular restriction is not the correct way to model the corresponding magnetic behaviour. Note that some of the values used for fitting are subject to nonneglectable errors, such that the coercivity difference would decrease further by taking the error bars into account.

To prove the ability of the angularly restricted extended STONER-WOHLFARTH model that was used to indeed vary the coercivity according to the subset of angles chosen, hystereses were simulated in steps of 2° , thus resulting in the contour plot

comparison between
coercivities obtained
from fitting and from
experimental Fe data

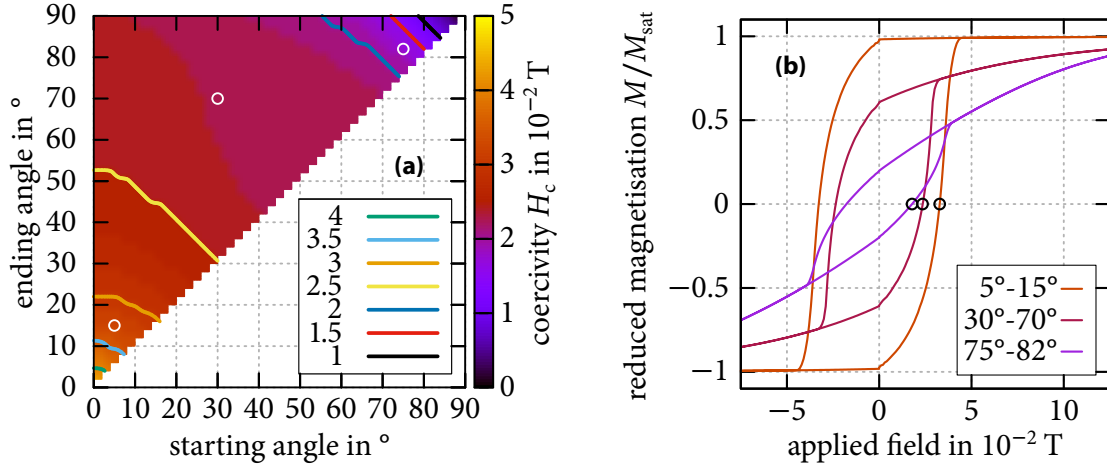


Figure 4.10.: (a) shows the coercivity H_c in dependence of a starting and an ending angle, that form a subset of $[0^\circ, 90^\circ]$ in the extended SW model. The parameters chosen for the simulation were $\mu^{\text{LN}} = 1.6$, $\sigma^{\text{LN}} = 1$ and $T = 2$ K. More parameters were $K = 3.7 \times 10^5 \text{ J m}^{-3}$ as well as a lattice constant of $\lambda_{\text{lat}} = 250 \text{ pm}$ and a saturation magnetic moment per atom of $\mu_{\text{satpa}} = 2.59 \mu_B$. The size distribution was taken into account from $\lambda_{\text{start}}^{\text{dia}} = \lambda_{\text{spm}}$ to $\lambda_{\text{end}}^{\text{dia}} = 20\lambda_{\text{spm}}$ with a stepsize of $\lambda_{\text{step}}^{\text{dia}} = 0.125\lambda_{\text{spm}}$. A face-centered cubic structure of the nanoparticles was assumed. Raw data: . (b) shows some example hystereses (raw data:), each of the three corresponding coercivities marks *one point*, illustrated by a circle, in (a).

shown in figure 4.10. Do note that the values chosen for the simulation were based on the values of the Fe nanoparticles of MARGÉAT et al., confer figure 4.9b. As one can see is the contour plot relatively flat, except the regions with small (below 20°) and large (above 70°) starting *and* ending angles. This was expected, as only in these subsets the influence of small respectively large coercivities does not get »smeared out«. Ergo provides the angular restriction in an extended STONER-WOHLFARTH model a way to tune the coercivity.

This subsection is based on the unpublished paper of BOGANI et al. [1], who also proposed the corresponding effects. Further elaborated texts on the topic of magnetization dynamics can be found in [78, 80]. To complement the models discussed so far, the next section deals with a model for multi domain ferromagnetism.

4.3. Jiles-Atherton-model

A widely used model that describes multi domain ferromagnetism is the JILES-ATHERTON-model that was invented in 1984 [12], which complements the superparamagnetic and single domain ferromagnetic models described thus far.

4.3.1. Theoretical background

The basic idea of this model is that there are two parts contributing to the magnetization. Firstly there is an anhysteretic magnetisation contribution, M_{an} , that shows no remanence and secondly an irreversible magnetisation contribution, M_{irr} .

To take the coupling between the different domains in a ferromagnet into account, an effective magnetic field is considered:

$$H_{\text{eff}} = H_{\text{ext}} + \alpha M^{\text{JA}} \quad (4.23)$$

Note that α is used to weigh the strength of the interdomain coupling. Consequently the anhysteretic magnetisation can be calculated via the LANGEVIN function,

$$M_{\text{an}}(H_{\text{eff}}) = M_{\text{sat}} \mathcal{L}(H_{\text{eff}}/a) = M_{\text{sat}} \left[\coth\left(\frac{H_{\text{eff}}}{a}\right) - \frac{a}{H_{\text{eff}}}\right], \quad (4.24)$$

wherein a is related to shape of the anhysteretic magnetisation.

While equation (4.24) already bears a hysteresis for a sufficiently strong interdomain coupling, or, correspondingly, a sufficiently large α , it is nevertheless appropriate to call it »anhysteretic« due to the fact that the interdomain coupling in experiments is usually found to be much smaller.

It has to be noted that the initial magnetisation curve exhibits, particularly at small applied fields, smaller values than the anhysteretic curve suggests, as the anhysteretic curve does not incorporate the possibility of domain wall movement hindrances by impurities.

The irreversible magnetisation contribution exists due to the impurities occurring in real materials, as domain walls »jump« over them if the externally applied field is large enough but they cannot easily »jump« back if the external field is turned off.

While JILES and ATHERTON found the basic equation for describing multi domain ferromagnetic materials, VENKATARAMAN extended it, notably via δ_M to avoid the unphysical occurrence of a *decreasing* magnetisation with an *increasing*

brief introduction to the concepts used throughout Jiles-Atherton theory

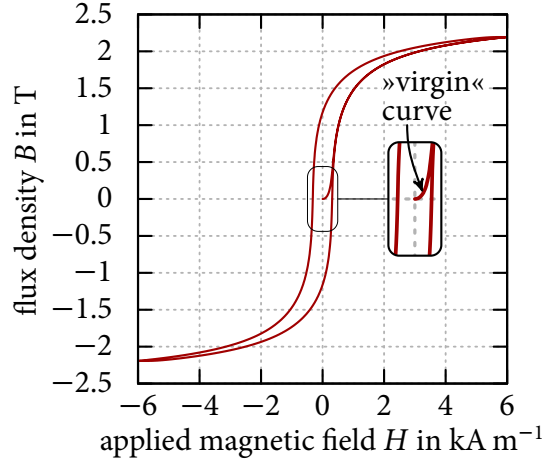


Figure 4.11.: Simulation using equation (4.27) as main equation. The values chosen were $\alpha = 1.6 \times 10^{-3}$, $a = 1100 \text{ A m}^{-1}$, $c = 0.2$, as well as $k = 0.0004 \text{ A m}^{-1}$ and $M_{\text{sat}} = 2 \times 10^6 \text{ A m}^{-1}$. The amount of steps sums up to 5000. Raw data:

external field. The resulting ordinary differential equation is

ordinary differential
equation for Jiles-
Atherton hystereses

$$\frac{dM^{\text{IA}}}{dH_{\text{ext}}} = \frac{k\delta c[\partial_{H_{\text{eff}}} M_{\text{an}}(H_{\text{eff}})] + \mu_0 \delta_M (M_{\text{an}} - M^{\text{IA}})}{k\delta - \mu_0 \delta_M \alpha [M_{\text{an}}(H_{\text{eff}}) - M^{\text{IA}}] - k\delta \alpha c [\partial_{H_{\text{eff}}} M_{\text{an}}(H_{\text{eff}})]} \quad (4.25)$$

wherein

$$\delta_M = \begin{cases} 0 & \dot{H}_{\text{ext}} < 0 \text{ and } M_{\text{an}}(H_{\text{eff}}) - M^{\text{IA}}(H_{\text{ext}}) > 0 \\ 0 & \dot{H}_{\text{ext}} > 0 \text{ and } M_{\text{an}}(H_{\text{eff}}) - M^{\text{IA}}(H_{\text{ext}}) < 0 \\ 1 & \text{otherwise} \end{cases} \quad (4.26)$$

and

$$\delta = \text{sgn}(\dot{H}_{\text{ext}}). \quad (4.27)$$

The k used above is a prefactor in the calculation of the total energy dissipated due to impurities by moving a domain wall a certain length. A measure for the material specific magnetic reversibility is included via c . \dot{H}_{ext} stands for the temporal change of the external applied field. An example curve can be found in figure 4.11.

This section, especially the part with the equations, is based upon [81, 82]. There are more models available, notably the PREISACH-model dating back to 1935 that is also commonly used.

4.3.2. Mathematica implementation

The *Mathematica* implementation of the extended JILES-ATHERTON model uses a trick introduced in [83], whereby the alternating applied field is constructed using

$$H = H_{\max} \sin(\omega t^{\text{IA}}). \quad (4.28)$$

As *Mathematica* cannot solve equation (4.25) with its standard built-in methods to the best of the authors knowledge a standard fourth order RUNGE-KUTTA method was coded, as it is quite suitable [84]. With this attempt to solve the ordinary differential equation it is possible to apply alternating x -values, as it is needed for hysteresis simulations. Consequently the following *Mathematica* function (see appendix D) has been defined that simulates a hysteresis with the extended JILES-ATHERTON model:

```
28 ExtendedJAModel[t_, M_, tstart_, tend_,
    numberofsteps_, Ms_, a_, k_, alpha_, c_, mu0_,
    Hmax_, omega_]
```

It is important to note that $t_$ and $M_$ have to be entered as just t and M . To account for the alternating nature of the applied field a starting value for t , $tstart_$, and an ending value, $tend_$, have to be given. The starting value has to be greater than 0, but can be arbitrarily small. The $numberofsteps_$ represent the number of steps that are used to reach $tend_$. Bear in mind that, due to the recursivity of this approach, the stepsize should not be chosen too large, as otherwise the precision decreases strongly.

Due to the sparse time available no fitting procedure for this model was implemented. Note that the parameters used for this model are non-trivial to estimate and there are papers dealing to a large extent with the procedures of finding suitable starting values, see for example [85, 86].

4.4. Conclusions

One can draw the conclusion that the superparamagnetism model represented by equation (4.6), at least if *not* fitted with other equations simultaneously, is not suited for extracting the nanoparticle size distribution, although it may be used to extract

explanation of the trick used to solve equation (4.25)

explanation of the *Mathematica* function that allows the calculation of Jiles-Atherton hystereses

an approximation of the peak of the distribution, which is reproduced roughly correct. The fit is however still a clear improvement over a single LANGEVIN fit, as can be seen in the increase of the adjusted coefficient of determination. Furthermore, the code of the *Mathematica* implementation is commented and documented in appendix B.

An extended STONER-WOHLFARTH model with an equation for the critical field that takes the temperature, the particle size distribution, the effective anisotropy and the angle θ between the external field and the easy axis into account. As the $\text{Co}_x\text{Ni}_{1-x}$ nanoparticle systems by BOGANI et al. are thought to be restricted in the orientation of their »effective easy axes«, if irradiated with a laser, the option to arbitrarily vary the subset of the angles between the »effective easy axis« and the external field was implemented in the corresponding *Mathematica* simulation and fitting models. The fitting routine did not yield sensible results for a $\text{Co}_{50}\text{Ni}_{50}$ system, probably caused by not respecting the ELLIOTT-YAFET mechanism in the equation for the critical field. However, it was proven that by limiting the scope of »effective easy axes« contributing to the hysteresis the coercivity can be varied over a large range. To increase the reusability of the *Mathematica* code for simulation and for fitting of STONER-WOHLFARTH hystereses it was included in appendix C, see ibidem for a documentation.

Finally, a *Mathematica* implementation of the multi domain ferromagnetism model, the JILES-ATHERTON model, allows hysteresis simulations in an extended form that rules out unphysical behaviour. Similar to the other models, the code can be found in appendix D with an appropriate documentation.

5. NiTi and Ni nanoparticles

There are a number of points to consider NiTi an interesting material. Alongside the biocompatibility and their implant process optimizing properties [14, 16] already mentioned in section 2.4 are NiTi («nitinol») materials famous for their shape memory, superelasticity and fatigue resistance [15]. As the nanoparticles used in [16] were also LASiS produced, but with an average diameter of approximately 60 nm, it was sensible to start the characterization of the used nanoparticles via gathering size related information with a TEM described in the following section 5.1.

5.1. TEM measurements on NiTi nanoparticles

To characterize the nitinol nanoparticles independently from magnetic measurements, a TEM as described in section 3.1 was used. Due to the sparse time the Tecnai G² was available only measurements at nitinol nanoparticles produced in water with a laser power of 0.33 W respectively 1.28 W were performed, as only these nitinol nanoparticles showed superparamagnetic behaviour in their ZFC-FC curves and hence were considered to be the most interesting. The samples were prepared as described in section 3.1. Two images are exemplarily shown in figure 5.1. The «dirt» that can be seen in figure 5.1 is probably due to remnants of acetone that was used to get the dried nanoparticles from their snap cap vial, where they are usually stored, to the carbon substrate that consequently was inserted in the TEM. A close look at figure 5.1 shows some «nanoparticles in nanoparticles». This phenomenon may be explained by sintering of newly created nanoparticles with TiO₂ as «filling» material [52], as the laser pulse heats them above a critical threshold – similar has been reported by AMENDOLA et al. for LASiS produced iron nanoparticles in a gel [87].

The resulting images, 13 for the 0.33 W nanoparticles and 28 for the 1.28 W nanoparticles, were evaluated manually by measuring the FERET¹ diameter of each

Explanation of the TEM images

¹Even though HEYWOOD brings up the issue that for elongated nanoparticles this diameter shows a large positive error, it can be used reliably for (almost) spherical nanoparticles, as for such

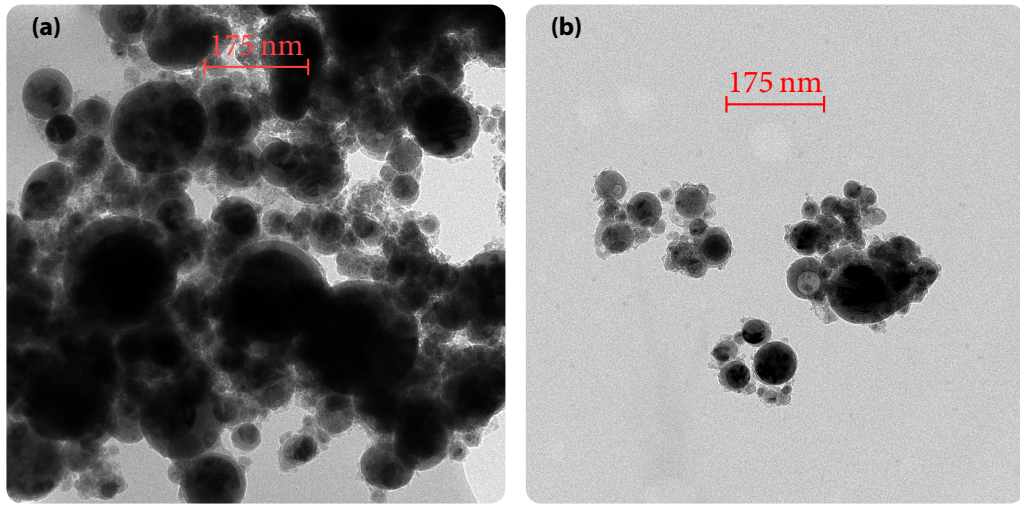


Figure 5.1.: The pictures show TEM images of nitinol nanoparticles produced with **(a)** 0.33 W respectively **(b)** 1.28 W. One pixel corresponds to 213.7 pm. The »dirt« is probably due to remnants of acetone.

clearly distinguishable nanoparticle. A manual evaluation was necessary, as the samples were too dirty to use an automated program routine. Consequently histograms were generated and a log-normal probability density function,

Evaluation of the TEM images

$$f^{\text{LN}}(D) = \begin{cases} \frac{1}{\sqrt{2\pi}\sigma^{\text{LN}}D} \exp\left(-\left[\frac{\ln(D) - \mu^{\text{LN}}}{\sqrt{2}\sigma^{\text{LN}}}\right]^2\right) & D > 0 \\ 0 & D \leq 0 \end{cases}, \quad (5.1)$$

as is appropriate for LASiS produced nanoparticles [89], is fitted to the histograms, confer figure 5.2. As expected show LASiS nanoparticles produced with higher laser power a narrower size distribution. This manifests itself in the smaller standard deviation, namely 8.1 nm for 1.28 W and 20.0 nm for 0.33 W. Note, that while the mean diameter is approximately equal, 29.7 nm for 1.28 W and 29.4 nm for 0.33 W, the maximum of the particle size probability density is at 26.3 nm for 1.28 W and 22.7 nm for 0.33 W. A possible explanation of this phenomenon may be given by the larger amount of material ablated by higher power laser pulses that subsequently

the error is small. For a comparison of different methods estimating the size of nanoparticles, confer [88].

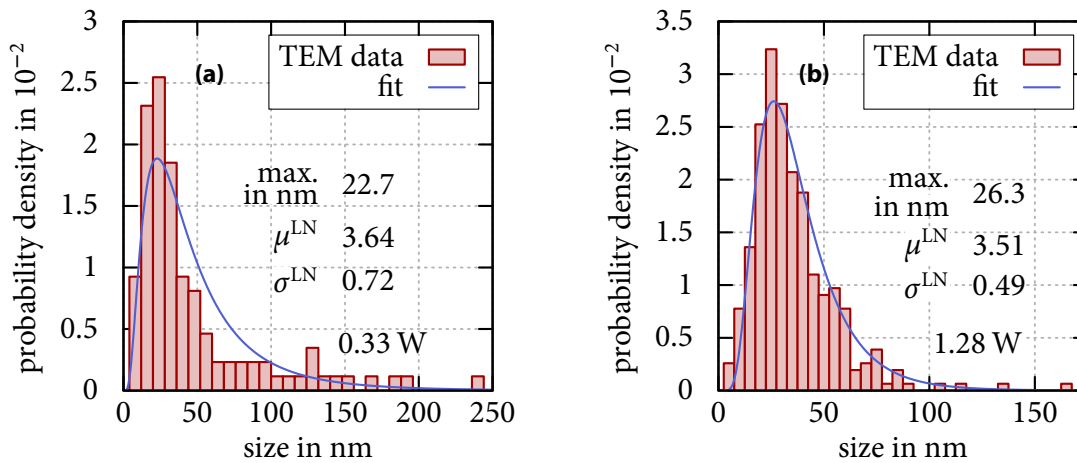


Figure 5.2.: The subfigures show the size probability density for nitinol nanoparticles produced in water. The fit assumes a log-normal distribution. **(a)** shows the result for nitinol nanoparticles produced with a laser pulse power of 0.33 W. The fit yields $\mu^{\text{LN}} \approx 3.64$ and $\sigma^{\text{LN}} \approx 0.72$. A total of 108 nanoparticles were analyzed. Raw data: . **(b)** shows the result for nitinol nanoparticles produced with a laser pulse power of 1.28 W. The fit yields $\mu^{\text{LN}} \approx 3.51$ and $\sigma^{\text{LN}} \approx 0.49$. A total of 309 nanoparticles were analyzed. Raw data: .

increases density of ablated material in the region where nucleation occurs, hence increasing chances for small nuclei to hit each other and therefore grow (in some cases) to a larger size compared to the lower power laser pulse case (confer [90]). Furthermore the stability of the laser is influenced by the laser power, such that there are larger fluctuations if the laser power is lower, therefore resulting in a broader probability density function [91]. This may also cause the shift of the maximum peak towards smaller diameters for the lower laser pulse power. However, it cannot be ruled out that the amount of nanoparticles that were countable from the images taken for the 0.33 W sample was just too small and these findings are just coincidental. It is crucial to note that the »giant« nanoparticles above 100 nm may rarely occur, but are not neglectable for magnetic considerations, as the amount of spins contributing to the magnetic behaviour scales with the cubic of the diameter.

Before magnetic measurements complementing these results could have been performed in the SQUID it was necessary to prepare the samples accordingly. The corresponding steps are discussed in the subsequent section 5.2.

Possible physical explanations for the change in the particle size distribution

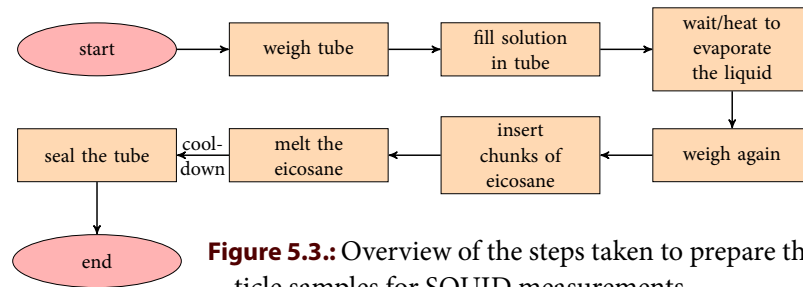


Figure 5.3.: Overview of the steps taken to prepare the nanoparticle samples for SQUID measurements.

5.2. Sample preparation for SQUID measurements

As the nanoparticles were received in powder form from the Ruhr-Universität Bochum, they had to be prepared for measurements. The procedural steps taken to obtain samples ready for SQUID measurements are sketched in figure 5.3 and comprise the following: First the empty NMR tube was weighed. This allowed the calculation of the sample mass later on, as the sample mass could not be measured directly with the equipment available due to the fact that substantial amounts of the nanoparticle powder adhere to the paper lying on top of the weighing scale. Then some drops of acetone are put with a one-way glass pipette into the nanoparticles' glass bottle. Subsequently the glass pipette was used to get the solution out of the bottom part of the nanoparticle glass tube and into the bottom part of the NMR tube. It is noteworthy that the solution was dropped into the bottom of the NMR tube with as little contact with the higher sections of the NMR tube as possible, such that there was less opportunity for the nanoparticles to adhere to the NMR tube there, consequently maximizing the signal at the bottom of the tube.

After some time the nanoparticles gather at the bottom of the NMR tube, if not much time was available a magnet was used to accelerate this process. To speed up the evaporation of the acetone a one-way glass pipette *without the usual yellow rubber balloon* was used to get the acetone above the nanoparticles out of the NMR tube by exploiting capillarity. The remnant of the acetone was either evaporating over night or, via heat gun, heated such that evaporation rate was greatly increased. In the latter case it is important to be aware of boil over. Thereafter the NMR tube was weighed again, the difference to the first weight measurement yields the weight of the added nanoparticles. Then (preferably larger chunks of) eicosane were added to the nanoparticles at the bottom of the tube. Consequently the eicosane was

insertion of nanoparticles to the sample tube

completion of sample tube preparation

melted by holding the NMR tube over a heat gun, such that upon eicosane freezing again the nanoparticles' reorientation is prevented later on. Finally the cooled down NMR tube was sealed with Teflon, labelled and stored in the sample holder.

The SQUID insertion of the samples was preceded by the following steps: Firstly the Teflon seal and the label had to be removed at the beginning. One of the plastic SQUID tube was taken and, by means of a toothpick, four holes surrounding the plastic tube in 90° steps were put on the middle of it. This procedure prevents the movement of the NMR tube later on. Subsequently Teflon tape was wrapped around the top of the NMR tube until it exactly fits into the plastic SQUID tube. Then the NMR tube was pushed into the plastic SQUID tube until the bottom of the NMR tube reached the four holes in the plastic SQUID tube. Lastly the ending can be placed at the bottom of the plastic SQUID tube, the protector of the sample holder was pushed up so that the plastic SQUID tube could be connected and after the protector was pushed down again the sample holder was ready to be inserted into the SQUID.

steps needed to make the sample tube »SQUID-ready«

It should be noted that these steps are not only relevant for the Ni respectively NiTi nanoparticles, but also the Fe₂O₃ nanoparticles mentioned in chapter 6. In section 5.3 are the results of subsequently performed magnetic measurements on the samples prepared by the methodology explained in this section shown.

5.3. Influence of the LASiS liquid on the magnetic behaviour

Depending on the liquid chosen for LASiS varies the nanoparticle size distribution. Two main effects are known to influence the nanoparticle size growth and hence the size distribution. Via layer formation of polar molecules of the liquid around the charged, growing nanoparticle are further charged nanoparticles electrostatically driven away. Additionally shrinks the reachable surface of the nanoparticle for approaching, non-charged nanoparticles. Thus the emerging nanoparticles are smaller for liquids with larger dipolar momentum, as the repulsive forces grow accordingly. The other main effect is relevant to liquids that contain carbon. If enough carbon is present, a carbon matrix can cover – at least partially – the surface of the, up to that moment, growing nanoparticle, thus inhibiting further growth.

factors contributing to nanoparticle growth

To estimate the influence of the liquid in which the nanoparticles were generated, measurements were performed on nanoparticles obtained in ethanol, water, acetone

and ethylacetat. The metal plate upon which the laser was focused was a nickel titanium alloy. Due to the modus operandi of LASiS (see section 2.1), fragments of the original liquid will interact with the ablated metal. Consequently, one can, *exempli gratia*, expect to find oxidized nanoparticles if the liquid in which they were created was water, as there is plenty of oxygen available. Thus it is of great importance to be aware of the species that occur in the nanoparticles. Therefore EDX measurement results are discussed in the following subsection.

5.3.1. EDX measurements

As it is necessary to know which atomic elements occur within a material to be able to understand the behaviour of the considered material, EDX is suited for this task, as it allows the determination of the type of atoms present in the sample. It is notable that this technique allows to get the chemical composition of punctual areas with approximately 1 nm diameter, such that it is possible to separately check the surface of a nanoparticle and also its core, as the penetration depth can be as large as 5 μm [92]. CHAKIF performed in his PhD thesis [52] EDX measurements on NiTi nanoparticles that were produced in different liquids – ethanol, water, acetone and ethyl acetate. As exactly these nanoparticles were used later on for the magnetic measurements, their composition is important. An investigation of a lighter area, as can be found in figure 5.1, reveals that the overwhelming amount of atoms in this shell are either Ti or O. Thus it seems reasonable to assume that the dominating structure in these regions of the nanoparticles is given by either TiO or TiO₂. The darker, core area of the nanoparticles is on the other hand dominated by a large amount of Ni, such that probably the most occurring lattices are Ni₃Ti and Ni₃Ti₂, respectively. Theoretical calculations of VENKATARAMANAN et al. have shown that the total magnetic moment of Ni_xTi clusters with $x \geq 5$ is nonzero, that the magnetic moments of the Ti atom align antiferromagnetically and that the stability of Ni₃Ti, Ni₆Ti and Ni₁₀Ti is larger than that of clusters with neighboring x values [93]. Notably, some nanoparticle cores consist almost purely of either Ni or Ti.

Figure 5.4a shows the atomic concentration of O, Ti and Ni in the nanoparticles for each liquid that was used while creating the nanoparticles. The amount of oxygen in the nanoparticles that were created in water is substantially higher than in any other liquid that was used. This can be understood by having a look at figure 5.4b. Therein the actually measured atomic concentration in the nanoparticles generated in the considered liquid is plotted against the atomic concentration of oxygen in the

EDX measurements
of NiTi nanoparticles

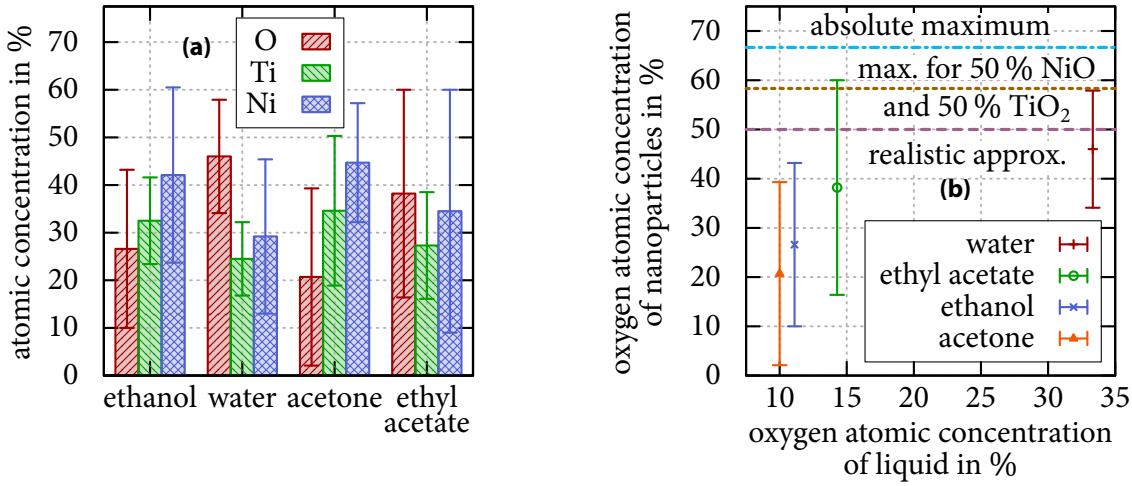


Figure 5.4.: (a) Atomic concentration of O, Ti and Ni in NiTi nanoparticles LASiS produced in different liquids. The measurement was done using EDX on 10 nanoparticles for each liquid and averaging. Remarkable is the large amount of O of the nanoparticles produced in water. Data from M` BAREK CHAKIF. (b) Plot of the atomic concentration of oxygen in the nanoparticles versus the atomic concentration of oxygen in the LASiS liquid. The steady increase indicates that the availability of oxygen in the LASiS liquid is the factor that limits the occurrence of oxygen in the nanoparticles until »oxidization saturation« is reached.

considered liquid. As one can see there is a steady increase in the measured atomic concentration in the nanoparticles with an increasing »offer«, respectively atomic concentration, of oxygen in the liquids. This is indicative of a oxygen concentration limit posed by the oxygen availability in the LASiS liquid, that in the end limits the occurrence of oxygen in the nanoparticles. Note that the absolute maximum that the oxygen atomic concentration could reach is given by a combination of NiO_2 and TiO_2 (or other compounds with such non-oxygen : oxygen ratios) and thus is found at 66.6 %, see the light blue line in figure 5.4b. Due to the strong oxidization potential of NiO_2 and Ni_2O_3 it is unlikely that they are found in relevant concentrations in the nanoparticles. Consequently, if NiO_2 , Ni_2O_3 and also NiTiO_3 , $\text{Ni}(\text{OH})_2$, NiCO_3 (only relevant if the LASiS liquid contains carbon) are neglected the brown line in figure 5.4b marks the new, lower maximum. A more realistic approximation would decrease the maximum concentration even more, as not all Ni and Ti atoms can

atomic concentrations found in the NiTi nanoparticles

Table 5.1.: Coercivity and shift of the 20 K hysteresis curves shown in figure 5.5. All values are in units of mT. Beware that this is by a factor of 10^3 smaller than the units of the applied field in figure 5.5.

	ethanol	water	acetone	ethyl acetate
coercivity	34.8	35.3	5.4	7.9
shift	0.12	0.03	0	-0.06

get oxidized, even if there would be enough oxygen available, as there is no way of ruling out the chance of the metal ions in the cooling plasma plume to interact with each other and therefore form for example NiTi *before* oxygen comes near them. A purple example line is drawn in figure 5.4b to provide a reasonable »guide to the eye«, although it is only an educated guess justified with the reasons stated above. Thus, the nanoparticles produced in water are probably near the »saturation oxidization« that is practically reachable with the LASiS procedure and NiTi as target substrate.

Subsequently some hysteresis measurements are shown and discussed.

5.3.2. Hysteresis measurements

hysteresis measurements

The results of the LASiS liquid dependent SQUID-magnetometer measurements lead to the curves shown in figure 5.5. As these samples were measured before the weighing of the samples was done as described in figure 5.3, their weight was not available, such that the measured magnetic moment could not be converted in the magnetisation. The hystereses observed indicate that for all nanoparticle powders, regardless of the chosen LASiS liquid, ferromagnetic behaving nanoparticles are present in a substantial amount of the whole sample. In the literature the coercivity for NiTi nanoparticles is found to be around 16 mT [94], but it has to be kept in mind that the authors do not mention the temperature at which they measured the hysteresis. As a comparison the values of the coercivities of the hystereses shown in figure 5.5 are listed in table 5.1. The occurrence of a relevant amount of Ni/NiO – or other exchange bias causing – surfaces can be ruled out, as the shift of the hysteresis is completely neglectable due to its very small values that may very well be caused by small measurement errors, see table 5.1.

To further examine the magnetic behaviour of these nanoparticles and obtain

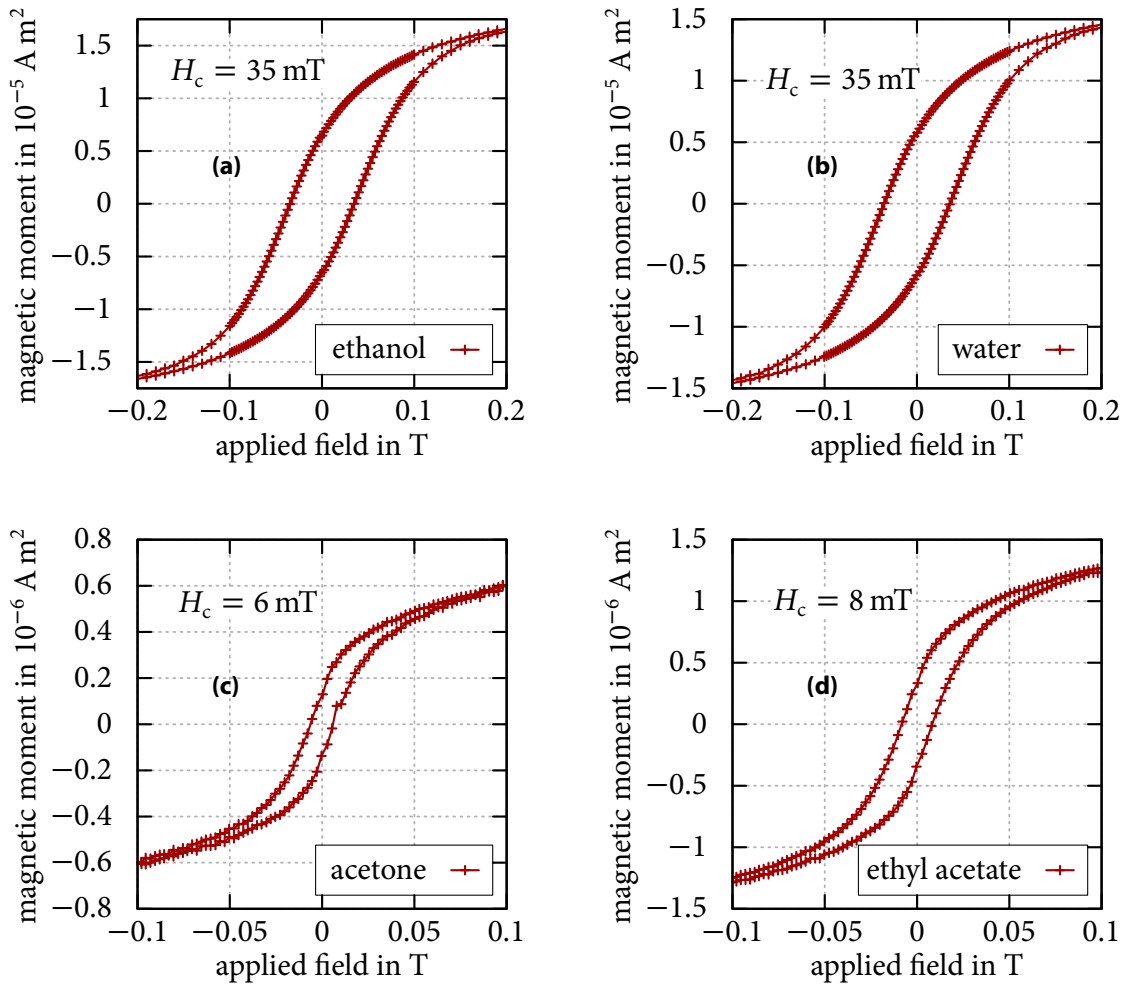


Figure 5.5.: These diagrams show the hysteresis measurements with a temperature of 20 K of nitinol nanoparticles produced in **(a)** ethanol (raw data: ) , **(b)** water (raw data: ) , **(c)** acetone (raw data: ) and **(d)** ethyl acetate (raw data: ) with a laser power of 1.28 W. Note the different x - and y -axis scales. The standard deviation, that can also be found in the raw data, is around 2%, only very few datapoints have higher deviations.

Table 5.2.: Fitting results of figures 5.6a, 5.6c and 5.6d using equation (5.2). Even though the fitting procedure worked, it has to be noted that the system resembles deterministic chaotic behaviour, as the dependence upon the given start values heavily influenced the fittings outcome. As the temperature at which the switching of the modified to the unmodified CURIE-WEISS law occurs is not ab initio determined, 125 K was chosen as reasonable fits were achievable thereby. Consequently this temperature is subject to a certain error proneness. Therefore the results have to be taken with care.

	ethanol	acetone	ethyl acetate
γ	1.30	1.24	1.33
T_1 in K	-136	-110	-189
T_2 in K	42	-46	-42

reliable information about, for example, the occurrence of superparamagnetically behaving nanoparticles, additional measurements using the ZFC-FC method were executed.

5.3.3. ZFC-FC measurements

The ZFC-FC measurements resulted in the diagrams shown in figure 5.6. As one can see exhibit the NiTi nanoparticles produced in ethanol, acetone and ethyl acetate similar paramagnetic behaviour. Consequently the measured magnetic moment was fitted by using a critical scaling behaviour of the CURIE-WEISS law [95] for low temperatures below $T < 125$ K, and an unmodified CURIE-WEISS law above this temperature, such that

$$\text{Curie-Weiss fitting function} \quad \mu_{\text{ZFCFC}} \propto \begin{cases} \frac{C_1}{(T - T_1)^\gamma} & T < 125 \text{ K} \\ \frac{C_2}{T - T_2} & T \geq 125 \text{ K} \end{cases} \quad (5.2)$$

describes the fit function. The results obtained are listed in table 5.2. The γ value for acetone is close to the theoretical value given by the standard ISING-model ($\gamma = 1.240$, [95]), while the values for ethanol and ethyl acetate are found in the realm between the ISING- and the HEISENBERG-model ($\gamma = 1.387$, [95]). This does

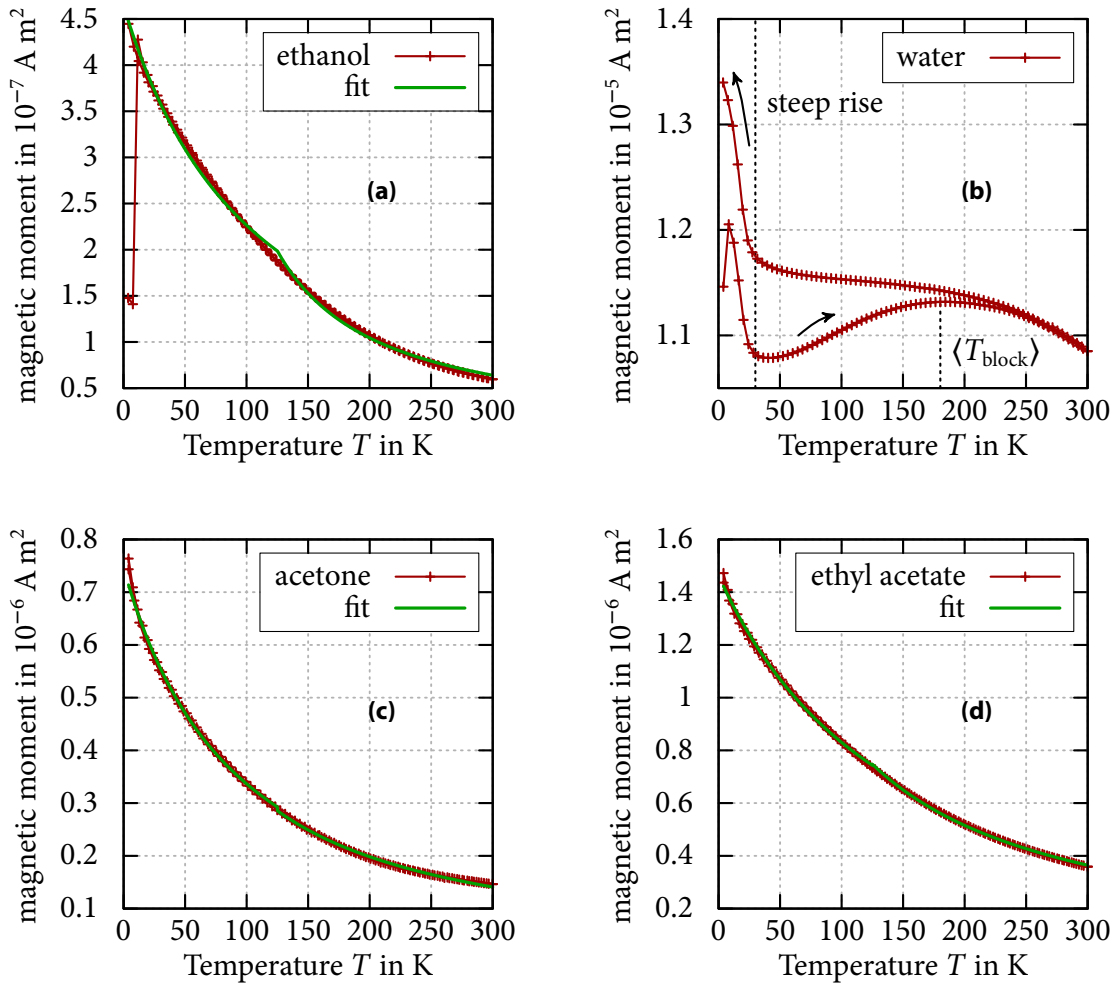


Figure 5.6.: These diagrams show the ZFC-FC measurements with an applied field of 0.1 T (respectively 1 kOe) of nitinol nanoparticles produced in **(a)** ethanol (raw data: ) **(b)** water (raw data: ) **(c)** acetone (raw data: ) and **(d)** ethyl acetate (raw data: ) with a laser power of 1.28 W. Note the different y -axis scales. The standard deviation is below 1 % and can be found in the raw data. **(b)** shows in contrast to the other samples superparamagnetic behaviour with an average temperature of system blocking of $\langle T_{\text{block}} \rangle = 180$ K and a steep rise of the magnetic moment if very small temperatures are approached – probably due to paramagnetic impurities.

however not imply that the nanoparticles act physically as these models describe, as the plethora of species that has to be assumed may, in superposition, lead to a behaviour that only *mimics* the behaviour of a true model obeying system. An influential amount of antiferromagnetically behaving nanoparticles seems to be located in the samples, as a negative T_1 is indicative for such dependencies found here. T_2 respectively the WEISS constant Θ , is larger than T_1 for all substances, but while the values for acetone and ethyl acetate still suggest antiferromagnetically behaving nanoparticles, switches the sign for ethanol from T_1 to the WEISS constant, indicating that the influence of ferromagnetically behaving nanoparticles exceeds in this regime the influence of antiferromagnetically behaving nanoparticles. Keep in mind that all these considerations have to be taken with care, due to reasons described in table 5.2.

The nanoparticles produced in water differ substantially, as they show clearly superparamagnetic behaviour in figure 5.6b with an average temperature of system blocking $\langle T_{\text{block}} \rangle = 180$ K. The irreversibility temperature is located around 230 K, as the ZFC and FC curves start converging there. Unusual for superparamagnetic behaviour is the steep rise of the measured magnetic moment that can be seen below 30 K. A possible explanation would be that this rise is caused by paramagnetic impurities. These may stem from a certain amount of almost pure Ti nanoparticles, that probably are found in the sample due to LASiS production restraints, as bulk Ti is paramagnetic [96].

To complement the ZFC-FC characterization of NiTi nanoparticles produced in water, the strength of the applied magnetic field was varied from 5 mT, 10 mT, 20 mT, ..., 120 mT (respectively 50 Oe, 100 Oe, 200 Oe, ..., 1200 Oe) leading to a contour plot shown in figure 5.7. Herefor NiTi nanoparticles produced with 0.33 W in water were used, as there should be no significant difference in species composition. Do note that the isolines shown are *not* identical to single ZFC or FC curves. For increasingly small fields the ZFC-FC curves get more and more »flat«, while for increasingly large fields the convergence of the two curves shifts to lower temperatures, so the externally applied field is, for ideal representation of the typical ZFC-FC features chosen to lie between 40 mT and 90 mT.

The ZFC measurements allow the extraction of field dependent peak temperatures that allow to check via a linear fit in a $T_{\text{max}}^{1/2}$ versus H diagram the influence of superparamagnetic behaviour and via a linear fit (called ALMEIDA-THOULESS line) in a T_{max} versus $H^{2/3}$ diagram the influence of spin glass-like behaviour [97]. A useful quantity for estimating which fit is superior is given by the coefficient of

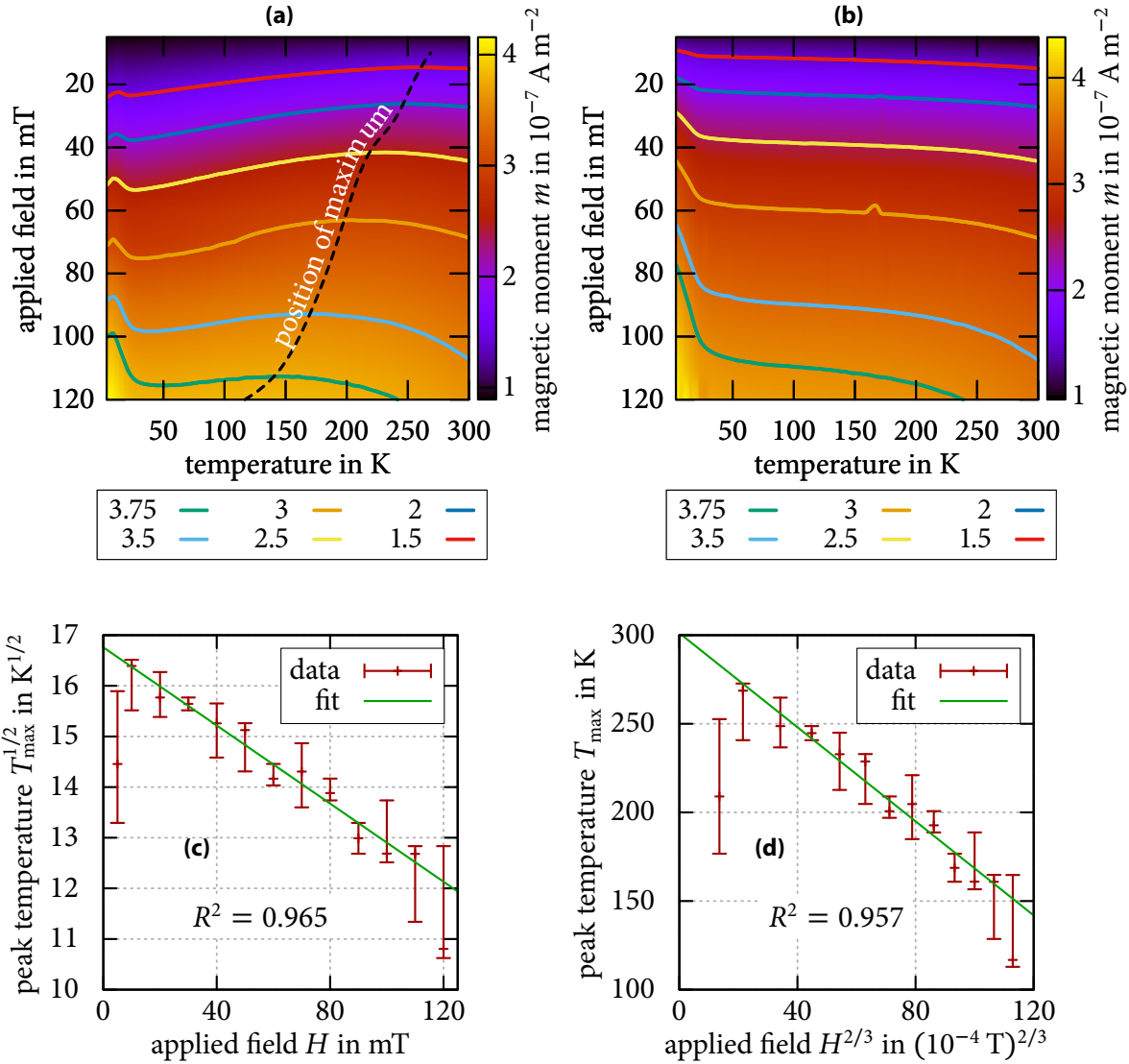


Figure 5.7.: Contour plots of (a) ZFC (raw data:) and (b) FC measurements (raw data:) of NiTi nanoparticles produced in water with 0.33 W depending on temperature and the applied magnetic field. Measurements were taken for applied magnetic field ranging from 5 mT, 10 mT, 20 mT, ..., 120 mT. Keep in mind that the isolines are not identical to single measurements. (c) and (d) allow to compare how well linear fits assuming (c) superparamagnetic behaviour and (d) spin glass-like behaviour work by displaying the coefficient of determination R^2 . Raw data for (c), (d): .

Table 5.3.: Comparison of the fitted linear curve coefficients of determination from figure 5.7c and figure 5.7d. Note that the first and last measurement point were excluded (confer text for further explanation). The high values of R^2 indicate that both fits work relatively well.

R^2 for	$T_{\max}^{1/2}$ versus H	T_{\max} versus $H^{2/3}$	ΔR^2
NiTi nanoparticles	0.9649	0.9575	0.0074
NiO nanoparticles [97]	0.9847	0.9945	0.0098

discussion of R^2 for
superparamagnetic
and spin-glass fits

determination, R^2 , as it quantifies how well a fit fits to the given data. For a perfect fit $R^2 = 1$, the less the fit function works with the given data points, the more approaches R^2 zero. This holds true if both systematic errors and the influence of the amount of fit variables can safely be neglected, as is the case in the corresponding plots that can be seen in figure 5.7c and figure 5.7d. Note that the measurement at 5 mT and 120 mT were excluded for the fits, as the initial ZFC curves showed a large amount of noise. The results are shown in table 5.3. They indicate that the system behaves more like a superparamagnet, even though the discrepancy, $\Delta R^2 = 0.0074$, is small, such that it seems unreasonable to completely rule out that measurement errors may contribute enough to make the systems behaviour *seem* to be different of what it actually is. In [97] the authors find $\Delta R^2 = 0.0098$ sufficient to conclude that the dominating effect is spin glass-like behaviour, but this value is bigger than the value found here, such that caution is appropriate.

Another source of information is given by ac measurements that are subsequently described on the NiTi nanoparticles.

5.3.4. AC measurements

brief introduction to
AC measurements
of NiTi nanoparticles

As mentioned beforehand offer ac measurements a valuable source of information about the dynamic behaviour of the studied nanoparticles. The outcomes of ac measurements yield a real part of the magnetic moment denoted by μ' and an imaginary part of the magnetic moment denoted by μ'' . Due to problems in the weighing procedure that was described in figure 5.3 the sample mass was not available for calculation of the magnetisation, hence preventing the use of χ' respectively χ'' . While quantitative statements are therefore impossible, the qualitative messages are still valid, as there is only a constant prefactor necessary to obtain the real re-

spectively imaginary magnetic susceptibility corresponding to the real respectively imaginary magnetic moment. The results of the LASiS liquid dependent nanoparticles ac measurements is shown in figure 5.8 for the real part and in figure 5.11 for the imaginary part of the magnetic moment.

As one can see in figure 5.8 show none of the investigated nanoparticles a strong frequency dependency of the shape of the curve – this would presuppose less symmetric isolines with respect to the frequency axis direction. While both acetone and ethyl acetate as LASiS liquid create NiTi nanoparticles that show a low temperature peak of μ' , shows water a steady increase with increasing temperature, but no peak is visible. Nanoparticles created in ethanol exhibit a barely visible peak in the very low temperature region (shown in more detail later on in the high resolution temperature scans) and a steady increase thereafter. It can, however, not be ruled out that nanoparticles generated in ethanol and especially water would peak (again) at a sufficiently high temperature above 300 K.

Thereafter some high resolution frequency scans were performed for each nanoparticle sample at the temperatures indicated by the dashed lines. These measurements are shown in figure 5.10 with the colour of each line corresponding to the colour of the dashed line in figure 5.8 respectively figure 5.11. Finally high resolution temperature scans around the peaks in figures 5.8c and 5.8d were performed for certain frequencies indicated by dot dashed lines in figure 5.8 respectively figure 5.11. Consequently these »cuts« through the contour plots in figure 5.8 respectively figure 5.11 may help to elucidate the shown data.

The μ' of the high resolution temperature scans is shown in figure 5.9. In figures 5.9c and 5.9d one can see that the peak for acetone and ethyl acetate is around 40 K and the local maximum for ethanol is at about 13 K. To show the evolution of the maximum temperature a guide to the eye passing through the maxima is drawn. The nanoparticles produced in ethanol and water show an increase in the magnetic moment with an increase in temperature, which may be caused by a peak that reaches its maximum value above 300 K and is therefore not measurable, as the eicosane used in the sample preparation would melt at temperatures above 300 K. Notable is, that the coarse grained measurement that was performed to obtain the ethyl acetate contour plot, figure 5.8d, shows the peak at approximately 60 K, thus showing the limitedness of measurements with large stepsizes ($\Delta T = 20$ K).

The overall decrease of the real part of the magnetic moment with increasing frequency is probably due to the smaller timespan that the nanoparticles can effectively use to align themselves along the external applied field. As a consequence, less magnetic moments are found aligned for larger frequencies.

μ' contourplot of NiTi nanoparticles

overview of the performed measurements

μ' high resolution temperature scans of NiTi nanoparticles

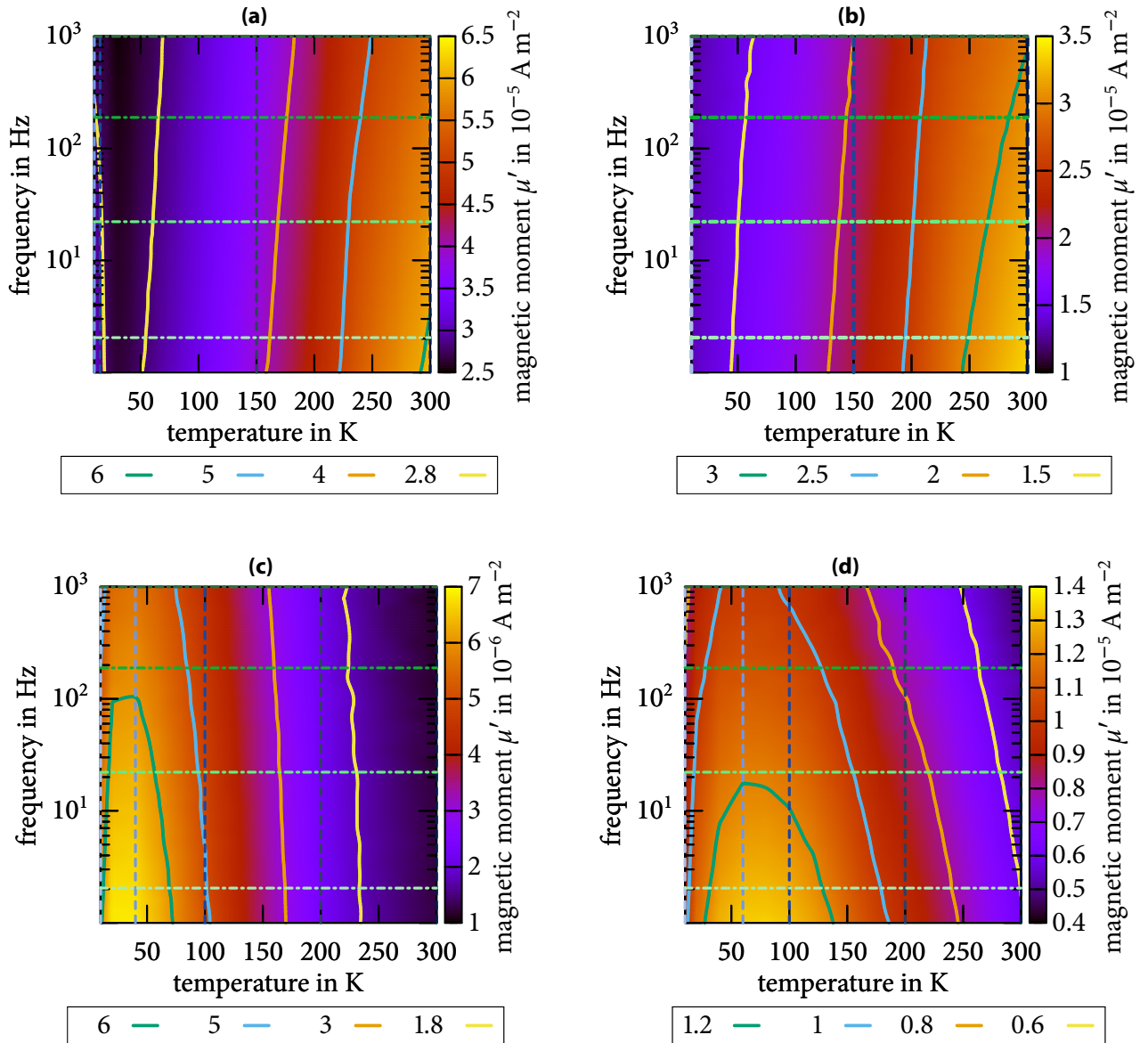


Figure 5.8.: These ac measurements were conducted with a frequency range of 1 Hz to 1 kHz. Temperature was varied from 10 K to 300 K. The color indicates the in-phase part of the magnetic moment, μ' . The nanoparticles were produced with a laser power of 1.28 W in (a) ethanol (raw data: ) (b) water (raw data: ) (c) acetone (raw data: ) and (d) ethyl acetate (raw data: ) with a NiTi substrate.

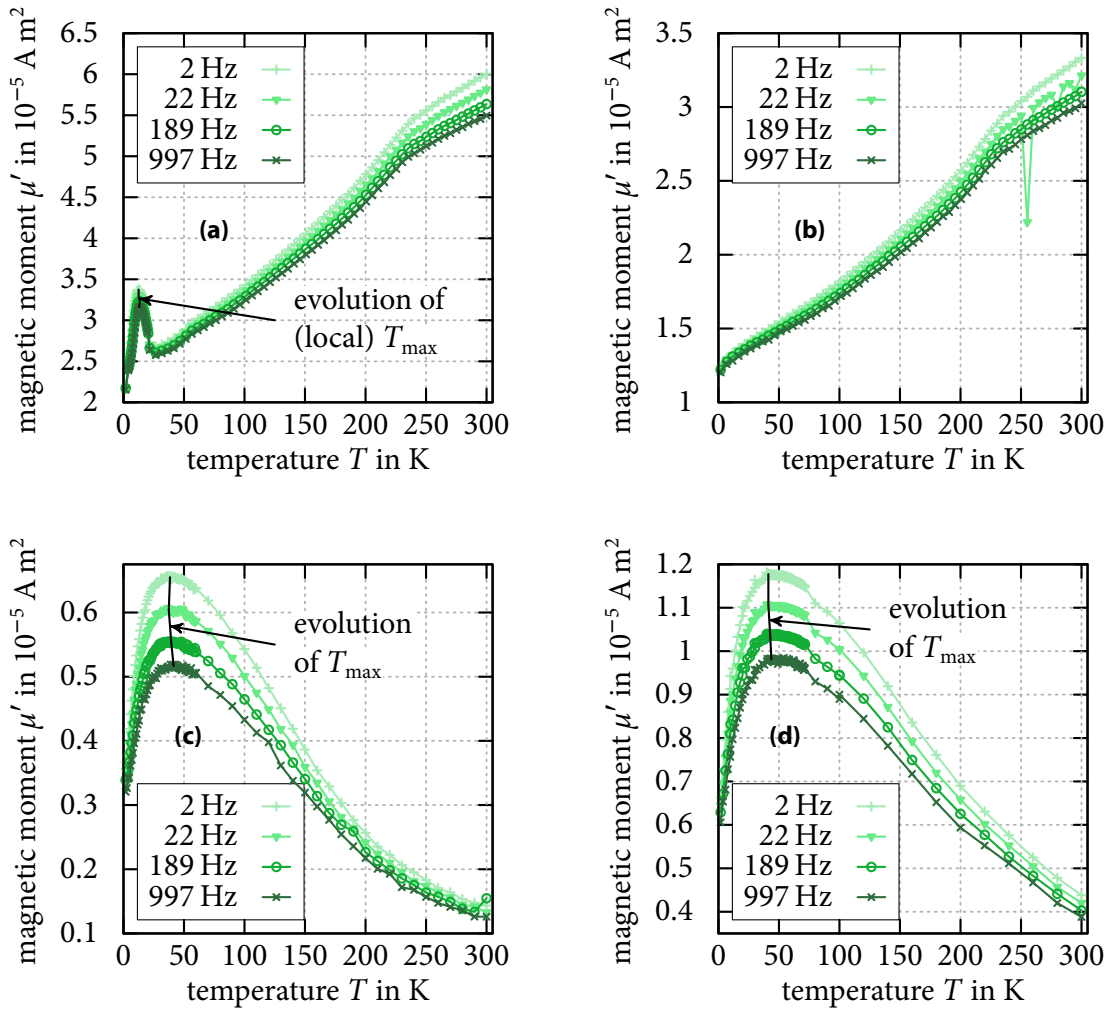


Figure 5.9.: These diagrams show high resolution temperature scans of the real part of the magnetic moment, μ' , of nitinol nanoparticles produced in (a) ethanol (raw data: \boxtimes), (b) water (raw data: \boxtimes), (c) acetone (raw data: \boxtimes) and (d) ethyl acetate (raw data: \boxtimes). The black line in (c) and (d) represents a guide to the eye through the temperatures for each frequency at which the maximum real part of the magnetic moment is reached.

Table 5.4.: Temperature T_{\max} corresponding to the maximum of the real part of the magnetic moment. Notice that a 6th order *moving average* was used to determine the maximum for acetone and ethyl acetate in order to minimize fluctuations. The resulting \bar{X} using equation (5.3) is shown as well.

T_{\max} in K at	ethanol	water	acetone	ethyl acetate
2 Hz	12.50	—	38.43	41.25
22 Hz	12.50	—	37.42	41.25
189 Hz	13.50	—	39.43	42.75
997 Hz	13.00	—	41.44	43.75
\bar{X}	0.004	—	0.01	0.01

A good way to estimate if a material is showing to a large part superparamagnetic behaviour is the value of \bar{X} , that for spin glass-like behaviour is found to be between 0.0045 and 0.06. For a superparamagnet \bar{X} is a lot bigger, on the order of 0.28². This value can be calculated via

$$\bar{X} = \sum_{i=1}^3 \frac{1}{3} \frac{T_{i+1} - T_i}{T_{i+1} (\ln(f_{i+1}) - \ln(f_i))}. \quad (5.3)$$

Note that this equation *averages* over the measured values. The results are shown in table 5.4 and indicate a spin glass-like behaviour for NiTi nanoparticles produced in acetone and ethyl acetate, as $\bar{X} \approx 0.01$. Even though \bar{X} is larger than 0 for nanoparticles produced in ethanol, the value is extremely small such that it is most probably not due to noninteracting superparamagnetic nanoparticles nor due to typical spin glass-like behaviour [99]. This may be indicative of cluster glass-like behaviour [99]. The behaviour of the nanoparticles created in acetone or ethyl acetate is however not unexpected, as neither the acetone nor the ethyl acetate produced NiTi nanoparticles show typical superparamagnetic behaviour in their ZFC-FC curves (figure 5.6c respectively figure 5.6d) and fine particle systems are known to behave often spin glass-like [100]. Another possible explanation that has to be considered is given by the fact that the peak temperature is determined from the smoothed raw data to minimize the influence of noise. Consequently there is a chance that the determined peak temperature is not the »real« peak temperature.

²For these values see [98].

explanation of \bar{X} for the nanoparticles produced in different LASiS liquids

Table 5.5.: The averaged fitting parameter $\bar{\alpha}_d$ that is indicative of the broadness of the relaxation time distribution is shown for each LASiS liquid used. As for most nanoparticles in this thesis, NiTi nanoparticles produced with a laser power of 1.28 W were used.

	ethanol	water	acetone	ethyl acetate
$\bar{\alpha}_d$	0.990 ± 0.008	0.989 ± 0.006	0.967 ± 0.008	0.974 ± 0.008

This view is supported by the *decrease* in the peak temperature that can be seen by comparing 2 Hz to 22 Hz for NiTi nanoparticles produced in acetone, see table 5.4.

A peak in the real part of the magnetic moment indicates that the susceptibility of the material to an external field is lower below the peak due to the low thermal energy that prevents easy »flipping« of the magnetic moments. Correspondingly the decrease observed above the peak stems from thermal fluctuations that are sufficiently large to lead to more disorder.

The high resolution frequency scans at a constant temperature of the real part of the magnetic moment are depicted in figure 5.10. To model the frequency dependency a modified COLE-COLE model using the assumption of $\mu_\infty = 0$ is used (see [101, 102]), thus leading to

$$\mu^{\text{mCC}} = \frac{\mu'_0}{1 + (i 2\pi f\tau)^{1-\alpha_d}}. \quad (5.4)$$

modified Cole-Cole fitting function

It is important to note that $\alpha_d = 0$ is indicative of a single relaxation time, whereas an increasing $\alpha_d < 1$ stems from an increasingly broad relaxation time distribution [101, 103]. The real parts of the magnetic moments shown in figure 5.10 are fitted to the real part of equation (5.4), $\Re(\mu^{\text{mCC}})$. In the insets are the measured points logarithmically in the range from 1 Hz to 100 Hz plotted, thus clarifying how good the fit is in this region. A simultaneous fit including the imaginary part was also tried, but did not succeed properly probably due to the noisy and very low values near the resolution limit of the imaginary part of the magnetic moment. The results of the fits are displayed in table 5.5. As the samples contain a broad distribution of nanoparticles with respect to size and composition a large value for $\bar{\alpha}_d$ is expectable. Accordingly, $\bar{\alpha}_d$ is roughly on the order of 0.98 for all tested liquids. This verifies the broad relaxation time distribution. Note that the errors are neglectable for the interpretation, due to their small value and the purely qualitative analysis.

μ' high resolution frequency scans of NiTi nanoparticles

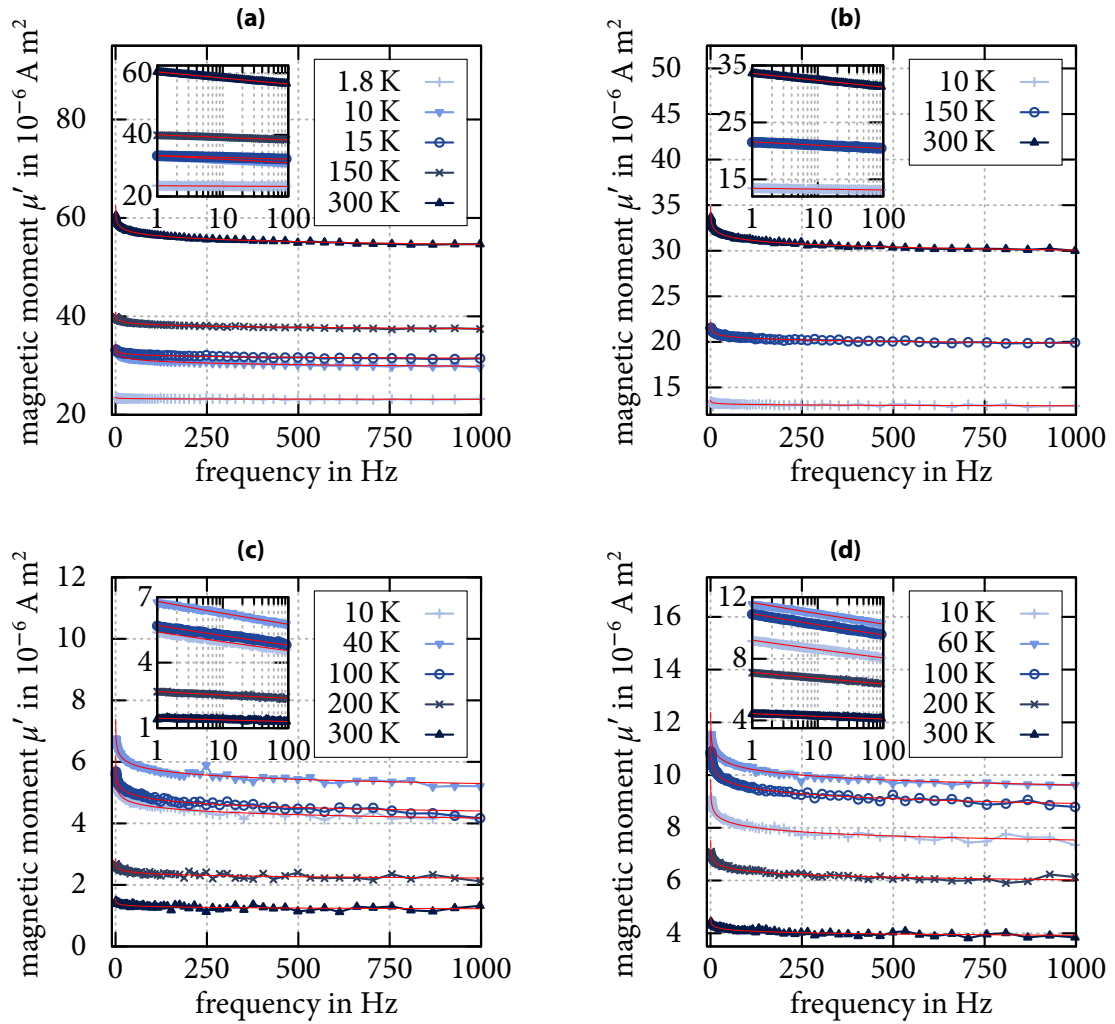


Figure 5.10.: Depicted are the real parts of the magnetic moment recorded with ac measurements of NiTi nanoparticles produced in **(a)** ethanol (raw data: \boxtimes), **(b)** water (raw data: \boxtimes), **(c)** acetone (raw data: \boxtimes) and **(d)** ethyl acetate (raw data: \boxtimes). The fits indicated by the red lines are achieved by fitting equation (5.4). To get a better impression of the measured data – fit course the inset in each picture shows the range between 1 Hz and 100 Hz logarithmically.

Subsequently are the plots of the imaginary parts of the magnetic moments shown, confer figure 5.11. In comparison to the real parts of the magnetic moment one can see that there are, in general, more fluctuations and the trend of the isolines shows a relatively high degree of parallelism with the frequency axis. Again, nanoparticles created in acetone and ethyl acetate express a peak in the measured temperature range, while their pendants generated in water shows a steady increase of μ'' with increasing temperature. Ethanol as LASiS liquid leads to sharp peak at very low temperatures, barely visible in the coarse contour plot, and a subsequent increase to higher temperatures. It is unclear from this data whether the nanoparticles obtained from ethanol or water as LASiS liquid would (again) reach a peak within a reasonably larger temperature, unfortunately were measurements with higher temperatures not possible due to the eicosanes melting point at circa 310 K in which the nanoparticles are embedded. As before follow high resolution temperature and frequency scans that may help to understand the contour plots.

μ'' contourplot of NiTi nanoparticles

Corresponding to the high resolution temperature scans of μ' are in figure 5.12 the results for μ'' shown. As is already visible in the contour plots in figure 5.11 is the amount of noise large compared to the real part of the magnetic moment. This is at least partially ascribable to the resolution limit that is around 10^{-7} A m², such that the errors can easily be larger than 20 %. Note that the peaks are – for acetone and ethyl acetate –, like for the μ' temperature scans, in the region at around 40 K, if the smoothed data is used. This may be an explanation to the fact that the corresponding contour plots do not show consistently a peak in this region. A peak in μ'' indicates that, at the peak temperature, the phase shift is at its maximum. Below the peak is the temperature too low to allow easy flipping of the magnetic moment, thus μ'' is small, as the phase shift is small. Above the peak thermal fluctuations take more and more over, such that the energy barrier is no longer the main obstacle preventing the flipping of the magnetic moment, effectively decreasing μ'' . For nanoparticles created in ethanol and water a general increase with temperature is visible. This may be caused by a broad peak at temperatures above 300 K. The general increase for higher frequencies may be due to the increased problems of the magnetic moments to follow the applied field at higher frequencies.

μ'' high resolution temperature scans of NiTi nanoparticles

The high resolution frequency scans of μ'' in figure 5.13 show that the imaginary part of the magnetic moment is on the order of 10^{-7} A m², consequently the data is very noisy, as can be seen by the single, red raw data line drawn for comparison with the smoothed data obtained via a 10th order running average. Thus the data has to be taken with care, as at best the general trend can be seen, but smaller features that may be present apart from the noise get smeared out by applying the running

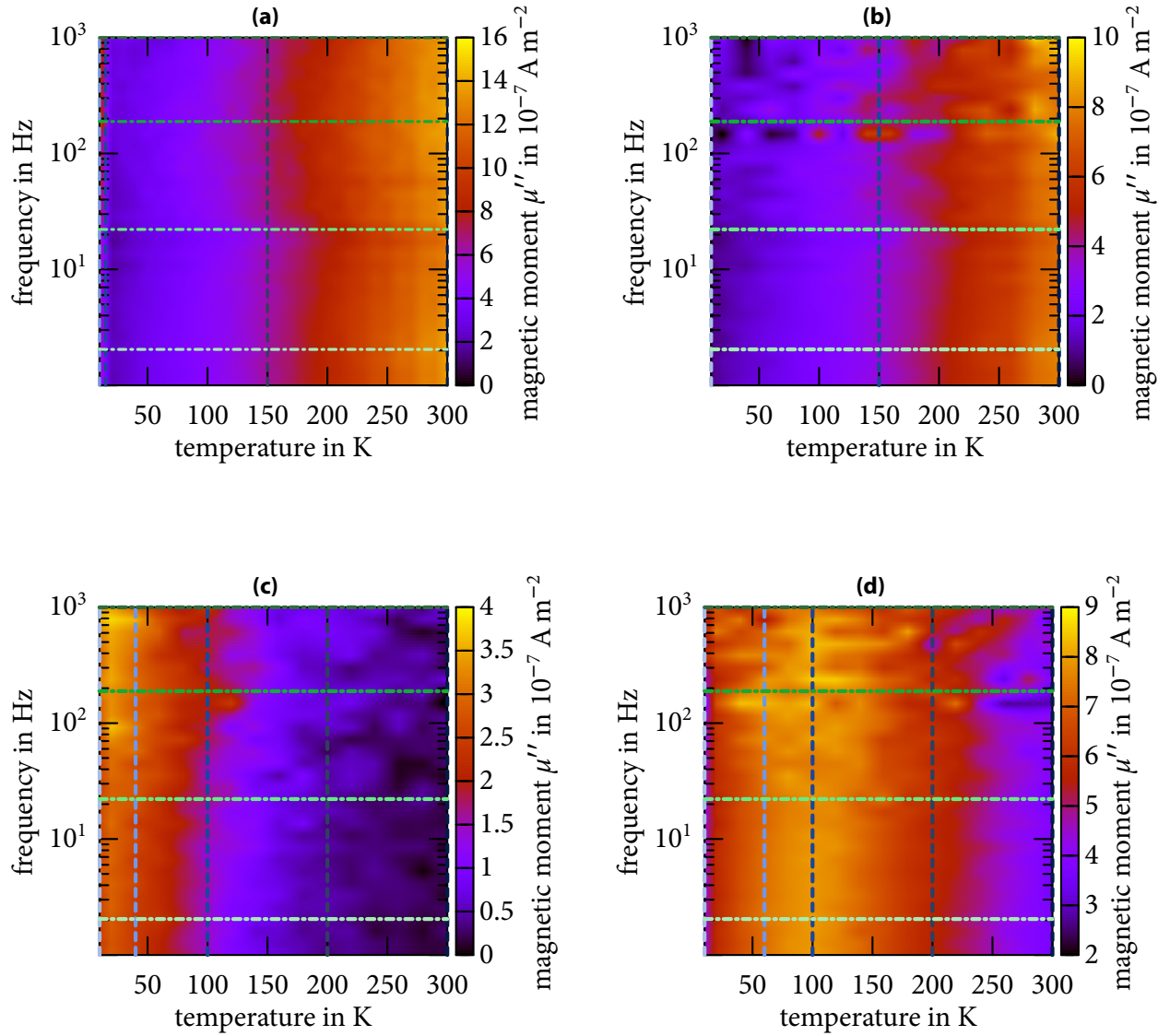


Figure 5.11.: These ac measurements were conducted with a frequency range of 1 Hz to 1 kHz. Temperature was varied from 10 K to 300 K. The color indicates the out-of-phase part of the magnetic moment, μ'' . The nanoparticles were produced with a laser power of 1.28 W in (a) ethanol (raw data: ) (b) water (raw data: ) (c) acetone (raw data: ) and (d) ethyl acetate (raw data: )

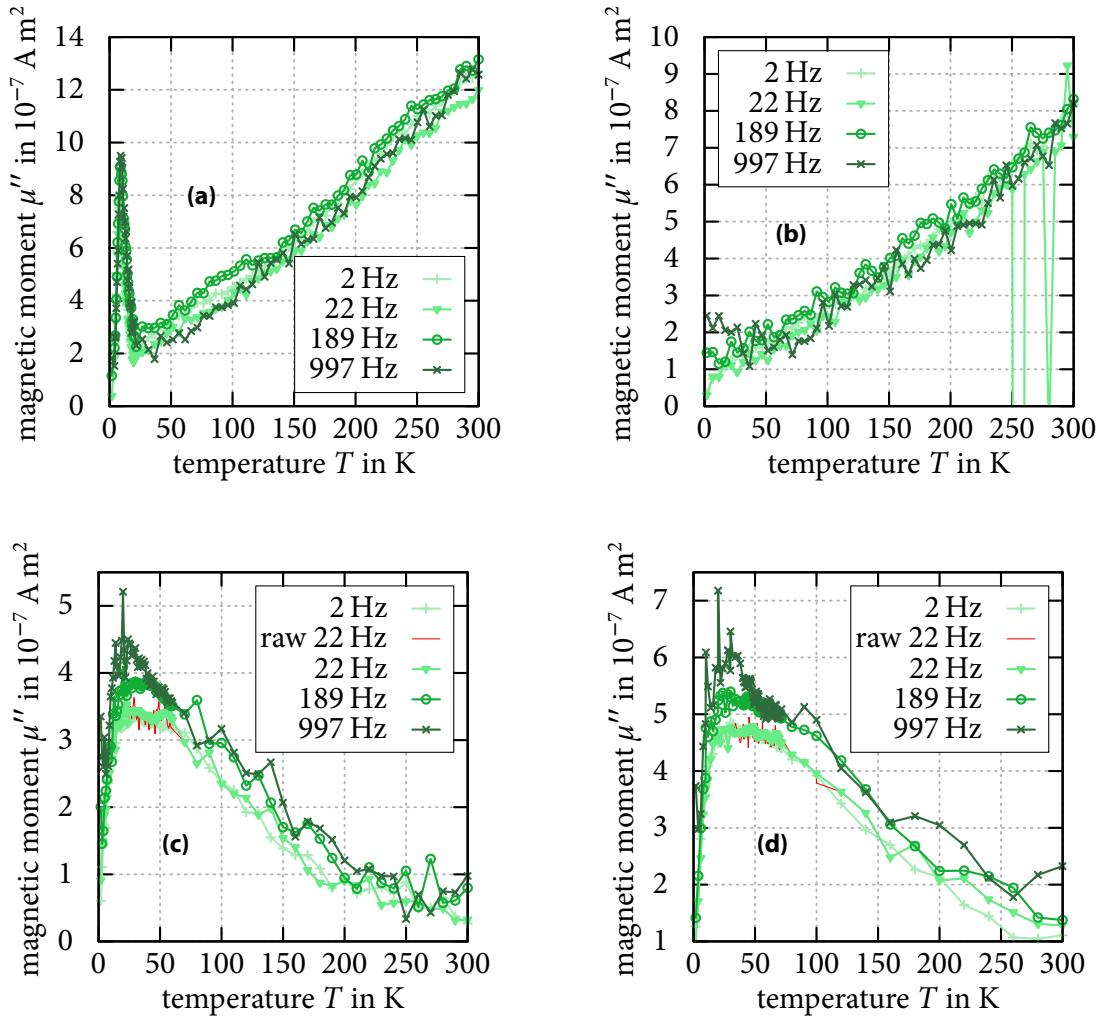


Figure 5.12.: These diagrams show high resolution temperature scans of the imaginary part of the magnetic moment, μ'' , of nitinol nanoparticles produced in (a) ethanol (raw data: \boxtimes), (b) water (raw data: \boxtimes), (c) acetone (raw data: \boxtimes) and (d) ethyl acetate (raw data: \boxtimes). For the sake of clarity are in the area of the peaks not the noisy measured datapoints, but the datapoints resulting from a 6th order running average shown (for nanoparticles created in acetone and ethyl acetate). To get an impression of the fluctuations the raw data for 22 Hz is plotted as well as the running average smoothed curve.

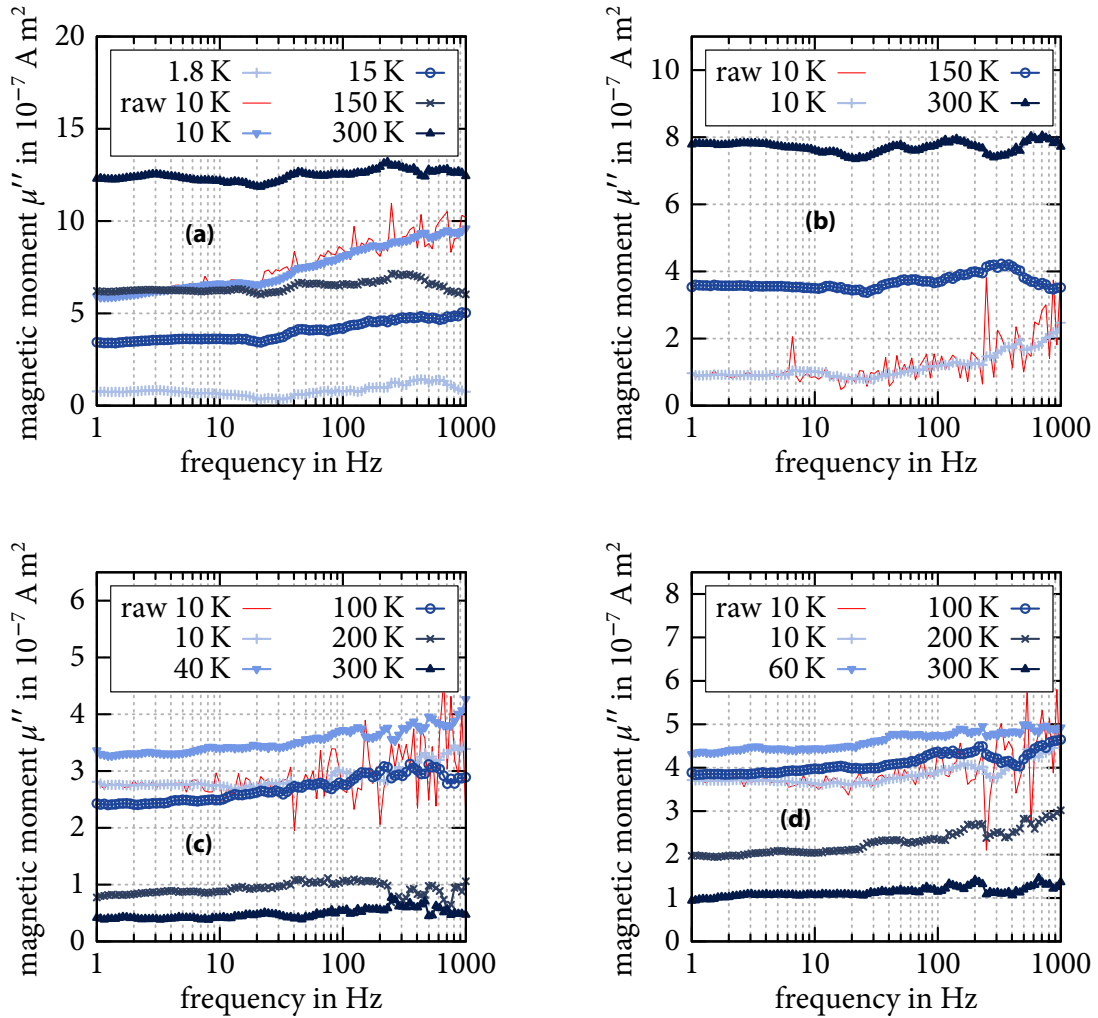


Figure 5.13.: Depicted are the imaginary parts of the magnetic moment recorded with ac measurements of NiTi nanoparticles produced in **(a)** ethanol (raw data: \square), **(b)** water (raw data: \square), **(c)** acetone (raw data: \square) and **(d)** ethyl acetate (raw data: \square). Note that a 10th order running average is shown instead of the actually measured data, as the raw data is very noisy, especially for higher frequencies. The 1st, 2nd, ..., 9th measurement point uses a 1st, 2nd, ..., 9th order running average, as there are not enough preceding data points for a 10th order running average. For a comparison of the averaged data to the raw data the latter is included for 10 K.

Table 5.6.: Coercivity and shift of the 20 K hysteresis curve shown in figure 5.14. All values are in units of mT. Beware that this is by a factor of 10^3 smaller than the units of the applied field in figure 5.5. Compare with the values of the NiTi nanoparticles in table 5.1. The Ni coercivity is close to values reported in the literature for similar systems [104].

Ni in water	
coercivity	23.9
shift	13.8

average. It can be seen that for high temperature frequency scans the imaginary part of the magnetic moment is neglectable, as it is comparable with the resolution of the SQUID-magnetometer. Corresponding to the discussion of the temperature scans of the imaginary part of the magnetic moment, the »offsets« of the frequency scans follows the shape of the temperature curves in figure 5.12. The running average data suggests that there is a slight increase of μ'' for frequencies above 100 Hz. This probably has its cause in the increasing difficulty for magnetic moments to follow fields that »switch« very fast. Note that $\Im(\mu^{\text{mCC}})$, confer equation (5.4), does *not* work as a fitting function due to the large influence of the noise.

μ'' high resolution frequency scans of NiTi nanoparticles

In general it is striking that the $\text{p}K_a$ value varies as follows in the LASiS liquids:

$$\begin{aligned} \text{p}K_a(\text{water}) &= 15.74, & \text{p}K_a(\text{ethanol}) &= 16, \\ \text{p}K_a(\text{acetone}) &= 20, & \text{p}K_a(\text{ethyl acetate}) &= 24.5. \end{aligned}$$

Thus the lower values for ethanol and water *may* be one of the factors that contribute to the different composition and hence dynamic properties of the nanoparticles.

As indicated by the EDX measurements discussed in section 5.3.1 are Ni rich nanoparticles not seldomly found in the LASiS produced NiTi substrate nanoparticles. To shed light on the magnetic behaviour of these nanoparticles some nanoparticles were LASiS produced in water with a pure Ni substrate. In the following section are the results of the measurements on these nanoparticles briefly shown.

5.4. Exchange bias in Ni nanoparticles

As Ni nanoparticles were expected to occur in the NiTi nanoparticles scrutinized so far, some nanoparticles LASiS produced in water from a pure Ni substrate were

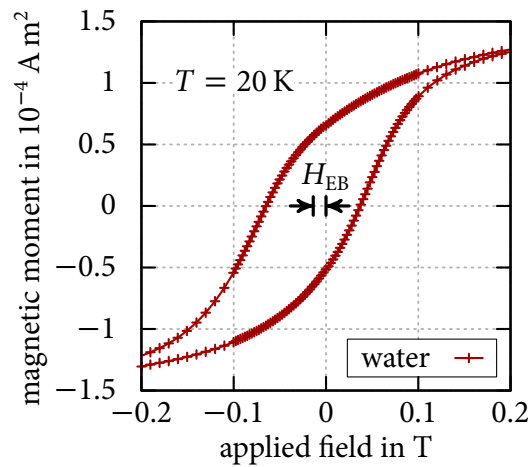


Figure 5.14.: Hysteresis measurement at 20 K for nickel nanoparticles produced in water with a pulsed laser power of 1.28 W. The exchange bias field was found to be $H_{EB} \approx 13.8$ mT (respectively 138 Oe). As nickel is ferromagnetic and nickel oxide is antiferromagnetic the ferromagnetic and the antiferromagnetic substances are probably in direct contact due to a core-shell morphology produced by the LASiS procedure. Similar behaviour of Ni/NiO interfaces is also reported in [105]. Raw data: .

analysed via hysteresis measurements to be able to compare them to the NiTi nanoparticles. In comparison with the values listed in table 5.1 shows the Ni hysteresis in figure 5.14 (see table 5.6 for the corresponding values) a large shift, while the coercivity is smaller than that for NiTi nanoparticles generated via LASiS in water respectively ethanol.

As a displacement of the hysteresis loop can be observed, it is probably caused by the exchange bias. Consequential of interfacial interactions of an antiferromagnetic substance in contact with a ferromagnetic substance an unidirectional anisotropy in the ferromagnetic substance is given rise to [106]. To create the exchange bias one typically has to cool down a system in which the order temperature of the ferromagnetic substance, the CURIE temperature T_C , lies above the order temperature of the antiferromagnetic substance, the NÉEL temperature T_N , with either an applied field or a magnetized ferromagnetic substance. It has to be noted that there are systems for which $T_C > T_N$ does not hold true [107]. Further information about Ni nanoparticles can be found in [108].

brief description of
the exchange bias
effect

In [109, 110] it was proposed that the exchange bias field H_{EB} depends on the average *slope* of the roughness, defined as the ratio h_{sl}/W between the the peak-to-valley height h_{sl} and the »wavelength« of the surface W . Either one or both of the two reasons mentioned afterwards are probably the cause for this effect. One potential cause is the assumed smaller grain size in the sample with larger roughness slope, as domain walls in the antiferromagnetic material tend to constitute themselves at grain boundaries due to a sudden change in the exchange interaction. The other possible cause may be the increased contact area of the ferro-/antiferromagnetic materials, hence an increased number of unidirectional spins influenced by the exchange interaction. It is noteworthy that even a dramatic increase in the root mean squared roughness did not increase H_{EB} accordingly (confer for this paragraph [109] and [110]).

slope of roughness
dependency of the
exchange bias field

In contrast to the systems described in [109, 110] show the nickel nanoparticles generated in water used to obtain figure 5.14 an exchange bias probably due to the formation of a Ni/NiO core-shell morphology of these nanoparticles. Consequently Ni has to be considered our ferromagnetic pendant to NiFe used in the papers by HWANG et al. [109, 110]. It seems reasonable to assume that, due to the »chaotic« nature of the nanoparticle formation with LASiS, our nanoparticles exhibit a comparatively large slope of roughness between the ferro- and the antiferromagnetic layer. Conclusively, yet hard to prove due to the lack of equally size distributed Ni/NiO core-shell nanoparticles with a slope of roughness that is *known* to be small, LASiS produced ferro-/antiferromagnetic core-shell nanoparticles may exhibit a large exchange bias field H_{EB} , although problems in terms of practical purposes would arise for sure due to the hardly experimentally adjustable slope of roughness. Further information can be found nonexhaustively in [67]. One possible application of the exchange bias is in systems working as spin valves [111].

comparison with sys-
tems found in the
literature

5.5. Conclusions

To summarize the most important features found for NiTi nanoparticles:

Even though BARCIKOWSKI et al. found no negative impact of laser ablated NiTi nanoparticles on the viability of stem cells [14], it does not seem reasonable to use these nanoparticles for in vivo applications, as TEM-EDX measurements showed that almost pure Ni nanoparticles do occur [52] – and these are thought to be carcinogenetic (confer [112]).

The influence of the laser power on the particle size distribution was found to

narrow with increasing power, even though the median diameter does not distinctively change. Counterintuitively, the maximum peak *increased* for larger laser power, maybe caused by larger fluctuations at smaller laser powers or an increased density of ablated material. Furthermore, the amount of oxygen in the LASiS liquid was identified as a parameter that allows the variation of oxygen in the finally produced nanoparticles.

All magnetically scrutinized NiTi nanoparticle samples contain ferromagnetically behaving Ni nanoparticles, although the coercivity of nanoparticles produced in ethanol and water is larger than that of nanoparticles produced in acetone and ethyl acetate. Only the nanoparticles produced in water show a clear peak in the ZFC measurements, with a steep rise below 30 K, probably due to paramagnetic Ti clusters or a second peak at very low temperatures. Linear fits to the ZFC peak temperatures in a $T_{\max}^{1/2}$ versus H respectively a T_{\max} versus $H^{2/3}$ diagram indicate that the whole system behaves more like a superparamagnet than like a spin glass, although the difference in the coefficient of determination that encourages this distinction is small and therefore to be taken cautiously. The ZFC measurements for the other liquids showed paramagnetic behaviour.

Extensive ac measurements revealed spin glass-like behaviour for NiTi nanoparticles created in acetone and ethyl acetate with a peak of the complex magnetic moment at circa 40 K. Nanoparticles that were generated in water respectively ethanol behaved similar to each other, with a steady increase of the complex magnetic moment, the only notable exception is a sharp peak at around 13 K for ethanol as LASiS liquid. A modified COLE-COLE fit verified the broadness of the relaxation time distribution that was anticipated due to the heterogeneity of the material.

Tests with nanoparticles ablated from pure Ni substrate show an exchange bias due to the Ni/NiO core-shell structure. Consequently, as the NiTi nanoparticles exhibit a neglectable exchange bias, »clean« Ni/NiO core-shell structures are probably not important for the explanation of the magnetic behaviour of the NiTi nanoparticles.

6. Fe₃O₄ and Fe nanoparticles

To complement the measurements of the influence of the LASiS liquid some measurements on nanoparticles produced by a different material, Fe, were performed to be able to estimate the influence of the laser power as described in the following section.

6.1. Influence of laser power on the magnetic behaviour of Fe nanoparticles

Initially hysteresis measurements on Fe nanoparticles produced by LASiS in an acetone : water (95 % : 5 %) mixture were performed. The sample preparation route was similar to the one described in section 5.2. Water is only sparsely added to acetone to keep the average diameter of the nanoparticles small as described elsewhere [28].

In figure 6.1a and figure 6.1b the hysteresis curves recorded at 20 K respectively 300 K are shown. The inset enlarges the area near the zero magnetic moment crossing to allow a better comparison of the corresponding coercivities. Figure 6.1c illustrates the coercivity in dependence of the laser power used for LASiS. There is a clear increase in coercivity if one switches from 1.28 W produced nanoparticles to such created at 2 W, while a slight coercivity decrease is evident for the switch from 2 W to 2.88 W. This behaviour is counterintuitive if the results of the laser power as discussed in section 5.1 are taken into account, as one would have expected a narrower size distribution and hence *more* superparamagnetic nanoparticles that do not contribute to the coercivity. The slight coercivity decrease for the switch from 2 W to 2.88 W has to be taken with care, as the error bars are comparably large at 2.88 W, such that the coercivity may very well be »saturated« and fluctuations may create the impression of a decrease. Problematic is also the small number of data-points, as trends are therefore hard to solidify. A possible explanation is given by a (slight) change not only in the size distribution, but in the chemical composition as well. Due to the lack of measurement time at an EDX this hypothesis was not

hysteresis measurements on Fe nanoparticles created at different laser powers

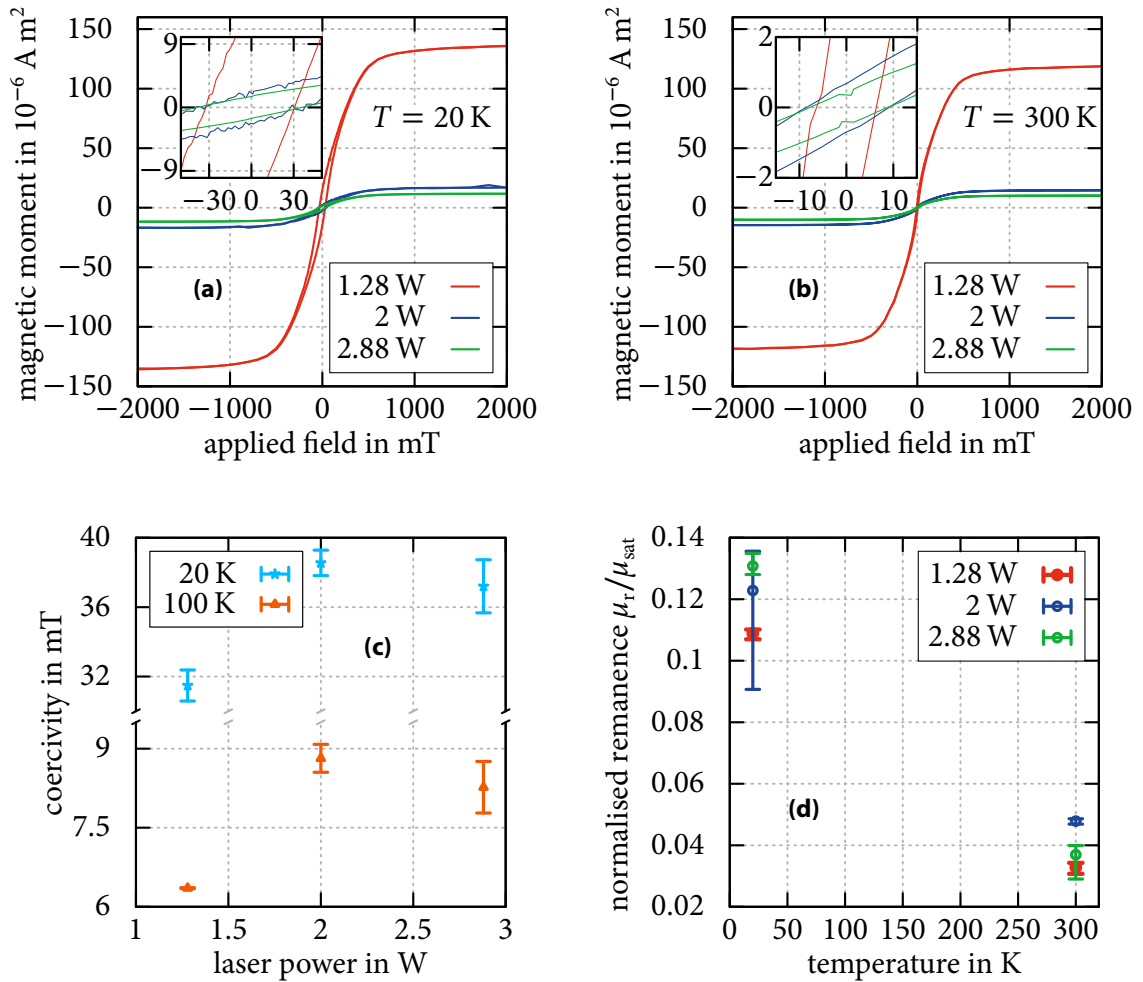
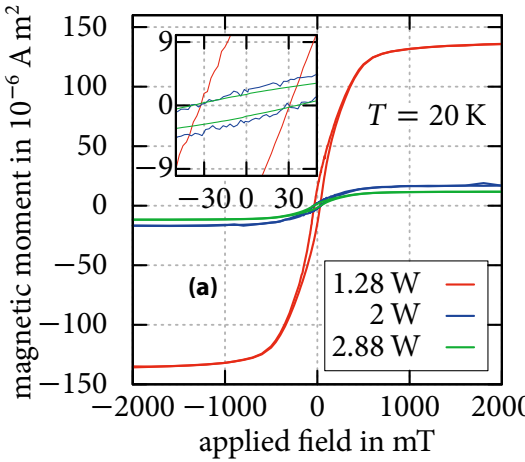
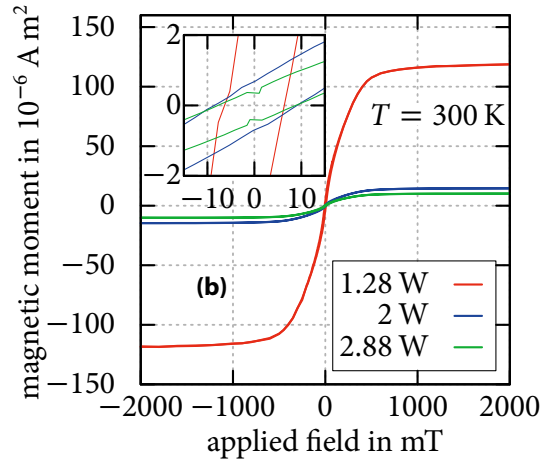
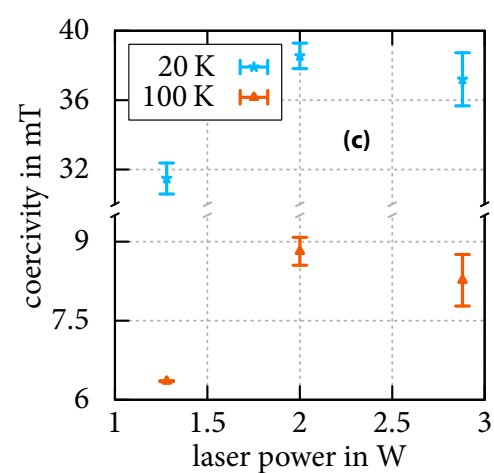
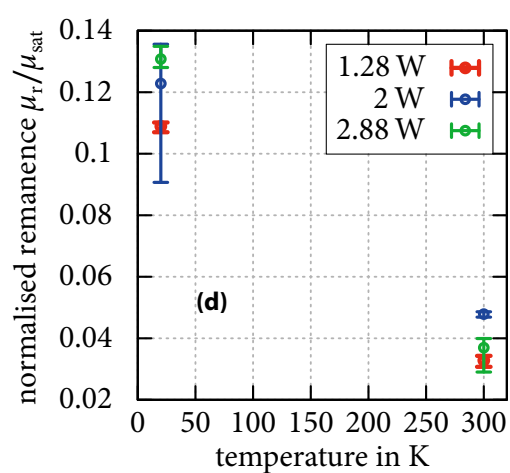


Figure 6.1.: Hysteresis measurements of Fe nanoparticles produced at different laser powers at **(a)** 20 K and **(b)** 300 K. **(c)** shows that the coercivity increases with laser power, while **(d)** shows that the remanence increases with laser power and decreasing temperatures. Note that the lines in **(c)** and **(d)** do *not* necessarily coincide with the actual physical behaviour, but serve merely as a guide to the eye. Raw data: **(a)** , **(b)** , **(c)**  and **(d)** .

testable within the timespan of the thesis. The problem of a low number of datapoints is especially obvious in figure 6.1d, such that one has to be cautious with the conclusions drawn from that graph and the lines have to be considered purely as guide to the eyes. In general the values of the normalised remanence vary between 0 and 1. STONER and WOHLFARTH predicted a normalised remanence of 0.5 for noninteracting, randomly oriented nanoparticles magnetically acting as dictated by coherent spin rotation. If the normalised remanence exceeds 0.5 exchange-coupling between the nanoparticles is indicated, below 0.5, as is clearly the case for the Fe nanoparticles scrutinized here, confer figure 6.1d, magnetostatic interactions may be of importance [113]. As the values increase slightly for higher laser power the amount of nanoparticles that comply to single domain ferromagnetic behaviour probably increases with laser power. Note that the value of the Fe nanoparticles created at 2.88 W and measured at 300 K is smaller than the one of the 2 W nanoparticles. It is noteworthy that the error bar for the 2.88 W nanoparticles is quite large and therefore, in combination with the very low amount of datapoints, a distinction between a measurement error and a trend in general cannot be made. The increase of remanence with decreasing temperatures is typical for ferromagnetic behaviour [114].

discussion about the remanence of the Fe nanoparticles

Figure 6.2 shows the influence of LASiS laser power on ZFC-FC measurements. The small deviation of the curves that can be seen in figure 6.2a and figure 6.2b may have multiple causes. On the one hand it is possible that the mean distance between the nanoparticles embedded in frozen eicosane was not constant and *thus* interparticle interactions vary between the samples. On the other hand it seems possible that the effect is not due to the final sample preparation steps, but rather due to an inherent change of, *exempli gratia*, the particle size distribution or the chemical composition caused by the variation of the laser power that consequently modifies interparticle interactions. Hence, a clear distinction between these possibilities is not feasible. Note that the occurrence of interparticle interactions can be assumed quite safely, as otherwise the normalised ZFC-FC curves should match each other and no shift of peaks should be visible¹ [115].

ZFC-FC measurements on the Fe nanoparticles

To check if there is a change in the superparamagnetic nature of the Fe nanoparticles, the same procedure as in figure 5.7c was used, leading to figure 6.2c. The corresponding coefficients of determination are shown in table 6.1. Appropriately, the trend suggests that with increasing laser power the system behaves *less* like a su-

¹As the peaks are broad, it may not be clear at a first glance that the peak temperature indeed varies, but figure 6.2c clearly shows that the peak temperatures are only similar for low applied fields.

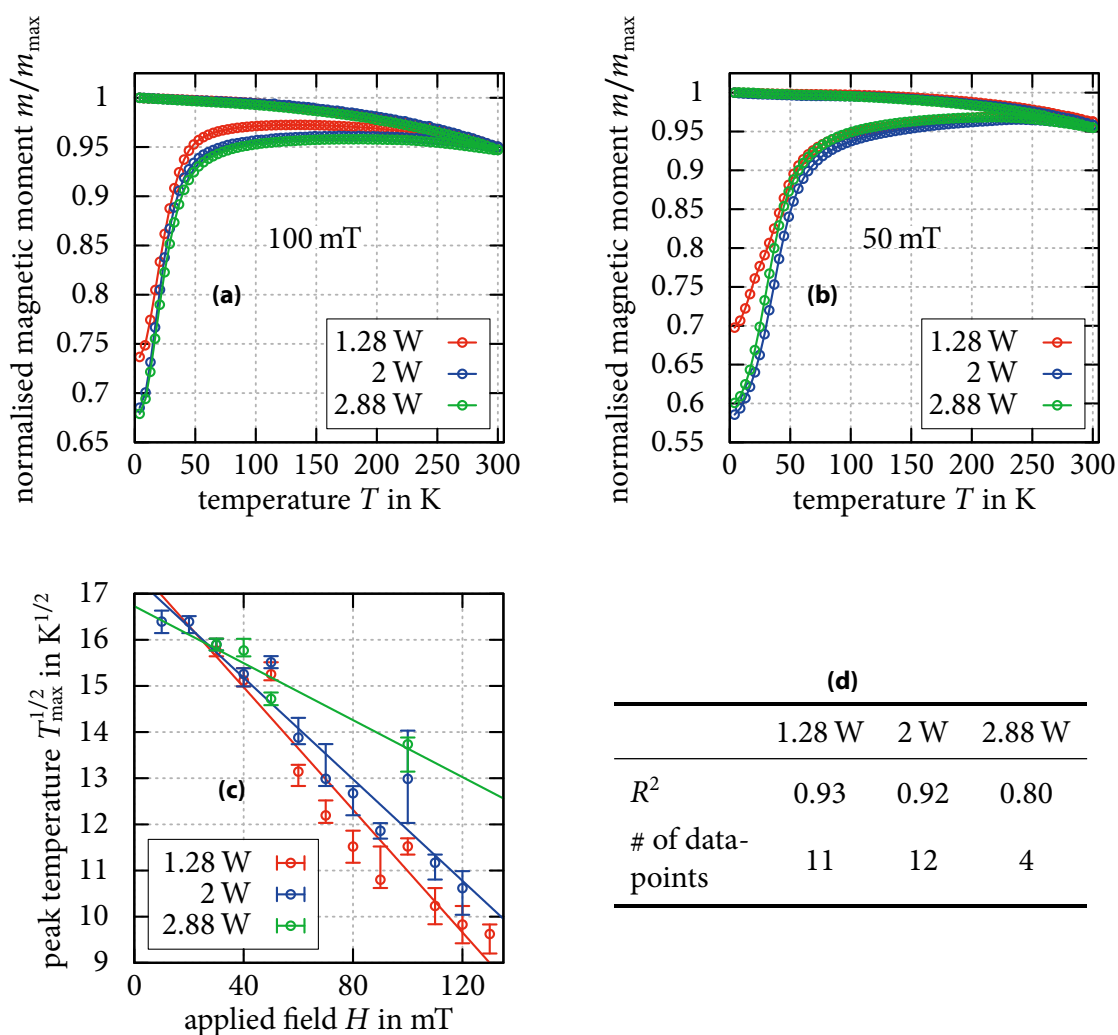


Figure 6.2 & Table 6.1: Normalized ZFC-FC measurements of Fe nanoparticles produced with different laser powers with an external field of (a) 100 mT (raw data: Ⓜ) and (b) 50 mT (raw data: Ⓜ). The small deviation of the curves indicate that interparticle interactions do occur and change [115], especially between 1.28 W and 2 W. A linear fit to a $T_{\max}^{1/2}$ versus H plot as shown in (c) (raw data: Ⓜ) can be used to determine how well the systems obey to superparamagnetic behaviour (confer figure 5.7c). (d) shows the coefficient of determination to the corresponding fits from (c) and the number of datapoints used to obtain R^2 . A detailed discussion of the implications is given in the text.

perparamagnetic one, as is expected due to the corresponding increase in coercivity that suggests larger particles, confer figure 6.1c. Do note that it is highly nontrivial to fit a function to datapoints with respect to their asymmetric error bars. Thus it was tried to improve the fit to the data for the nanoparticles created at 1.28 W via manually changing the datapoints (in the borders given by the error bars) taken into account by the linear regression fit. Thereby the coefficient of determination increased from approximately 0.89 to 0.93. Another point of concern is the small amount of datapoints for 2.88 W, as contributions of fluctuations are much more influential if there are few datapoints. Consequently, the trend that can be seen in the coefficients of determination might be severely weakened by applying the fitting method described above for 1.28 W to the nanoparticles created at the other laser powers as well as by increasing the amount of datapoints, especially for 2.88 W.

Note that measurements on purely superparamagnetic Fe_3O_4 nanoparticles were performed as well. The Fe_3O_4 nanoparticle samples² were prepared by a different method to prevent the nanoparticles from direct contact with air. After approximately 0.1 mL of the solution containing the nanoparticles was put in a NMR tube, it was cooled down by placing the NMR tube in liquid nitrogen. Parallely the NMR tube was evacuated and filled with argon multiple times. In the end the tube was sealed with a BUNSEN burner melting the top of the tube. These measurements did not yield sensible results, probably at least partly due to a low amount of original Fe_2O_3 nanoparticles in the solution, as many may have degraded due to photo-oxidization to iron oxide hydroxide [116]. This assumption is strengthened by the yellow-orange color of the solution, as this color matches with the assumed iron oxide hydroxide. Additionally the low concentration indicated by the color and the absence of flocculation may have contributed to the obtained nonsensible results.

Synoptically, one can draw the conclusion that the measurements performed in this chapter do not suffice to estimate unambiguously the effect of laser power on the properties of Fe nanoparticles. An increase in coercivity with laser power as well as a decrease of the coefficient of determination with respect to a superparamagnetic fit with laser power was observed. This is counterintuitive, as this suggests an increase in particle size, contrary to what has been found in section 5.1. To solidify these trends, TEM and EDX measurements would be very helpful, as they would allow to greatly increase the confidence that the findings are not mere correlations, but indeed causally conditioned.

²It should be noted that these were produced in 2012 by Particular GmbH via the LASiS method – over two years ago, so ageing effects may not be neglectable.

coefficients of determination to a superparamagnetic fit

measurements on purely superparamagnetic nanoparticles

7. Conclusions and perspectives

In this thesis, various dynamic and static magnetic measurement techniques have been utilized to reveal the magnetic properties of magnetic nanoparticles and obtain information about the influence of the fabrication method on the magnetic behaviour.

An extensive magnetic characterisation of NiTi nanoparticles produced via laser ablation synthesis in solution (LASiS) was undertaken. Nanoparticles fabricated in ethanol, water, acetone and ethyl acetate were investigated to estimate the influence of the LASiS mother solution on the magnetic behaviour. For nanoparticles created in acetone and ethyl acetate, spin glass-like behaviour was uncovered, while nanoparticles produced in water show a field dependent temperature shift of the peak zero field cooling (ZFC) temperature that indicates superparamagnetic behaviour. Nanoparticles produced in ethanol exhibit mainly paramagnetic behaviour. Thus, it is possible to tune the magnetic behaviour of nanoparticles by choosing specific LASiS liquids. The broadness of the relaxation time distribution was successfully determined by a modified COLE-COLE fit to dynamic measurements, whereby the cause for the broad distribution can be found in the broad nanoparticle size distribution and the diverse chemical composition. The varying magnetic responses of the nanoparticles are partly related to the different amounts of oxygen in the nanoparticles that can be fine-tuned by choosing a LASiS liquid which contains a specific amount of oxygen. Another adjustable parameter is the laser power used to ablate the nanoparticles, whose impact was additionally checked with Fe nanoparticles. It was found that with increasing laser power the coercivity increases and the amount of superparamagnetically behaving nanoparticles decreases. This eventually opens a window to fine-tune the coercivity as desired for a specific application. Hereby, further measurements on nanoparticles produced at different laser powers are compulsory to solidify these claims and to estimate the »coercivity resolution« that can be reached conclusively. Altogether, these findings provide a well-elaborated basis that simplifies further developments in magnetic tailoring of NiTi nanoparticles. Depending on long-term biocompatibility studies this may prepare the ground for a use as hyperthermia agents.

Further insights in the magnetic behaviour of nanoparticles were achieved by the successful *Mathematica* implementation of the extended, superparamagnetic LANGEVIN model for $m(H)$ measurements that takes the particle size distribution into account. The quality of this fit to pure Ni nanoparticles is superior to that of a »standard« LANGEVIN fit, which does not consider the particle size distribution. Nevertheless, there is still a discrepancy between the particle size distribution as obtained via TEM images and the distribution resulting from the extended LANGEVIN fit. This is most likely due to the sensitive nature of the equations in the used magnetic model. Further improvements that probably lead to a more accurate reproduction of the size distribution are possible by simultaneously fitting to $m(H)$, ZFC and field cooling (FC) data as TAMION et al. proposed [10].

Finally, an exotic system of CoNi nanoparticles that allows the functionalisation of the magnetic behaviour with laser light was theoretically investigated with the help of simulations. CoNi nanoparticles exhibit a wavelength dependent modification of the coercivity caused by excited nanoparticle plasmons induced by laser light. This leads to an additional, artificial anisotropy that results in an »effective« easy axis. As the angle between the »effective« easy axis and the direction of an applied field is only a subset of the angles that are possible if no laser light modulation is used, the magnetic behaviour changes accordingly. To reproduce this behaviour an extended STONER-WOHLFARTH model was implemented in *Mathematica*, which revealed that the limitation of the allowed angles between the nanoparticles »effective« easy axis and the direction of an applied field indeed permits drastic coercivity changes. The discrepancy between the coercivity found by simulations and real CoNi data originates from not considering the spin-flip transition rate inside the nanoparticles stemming from the ELLIOTT-YAFET mechanism. Consequently, a mathematical model of the ELLIOTT-YAFET mechanism has to be implemented in the simulation procedure to improve the simulation results. This would grant a decisive insight in the applicability of the extended STONER-WOHLFARTH model on the magnetic behaviour of light stimulated nanoparticles.

Advanced parameters that influence the magnetic behaviour of nanoparticles are not found in any common magnetism model. However, functionalisation of the nanoparticle surface, the choice of a certain shape of and the chemical composition are practically of huge importance, as they strongly influence the magnetic properties. Thus, the implemented and documented magnetism models can serve as a starting point for other researchers that will speed up the understanding of magnetic nanoparticles, as there is currently a lack of freely available implementations.

8. Acknowledgements

First I want to thank Prof. DRESSEL for giving me the opportunity to conduct my master's thesis at his institute, even though neither of my master's in-depth nor my master's complementary module did cover solid state physics. Additionally I have to thank Prof. MICHLER for being my second supervisor. I also want to express my gratitude towards Dr. BOGANI, as he had an enormous amount of patience and could always help if help was needed.

I am probably most indebted to MICHAEL SLOTA and ERIC HEINTZE who are exceptionally good tutors, as their large fund of knowledge, their patience, humour and continuous encouragement contributed greatly to the (hopefully) successful completion of this thesis.

Furthermore I want to thank Dr. M'BAREK CHAKIF for providing the LASiS produced samples as well as Dr. KATHARINA HIPPE for providing access to and help with the TEM. Not to forget is the valuable companionship of the other members of the office, Dr. RALPH HÜBNER for his patience with a non-chemist, RALF KONNERTH and LUKAS SEBEKE for supplying me with enough candy to keep my blood sugar level high enough to actually do work, MARIAN BLANKENHORN and JONATHAN NÄGELE for the many discussions about strange behaviour of gauges and programs. Also worth mentioning is the support by the users of `mathematica.stackexchange` and `tex.stackexchange`.

It is a pleasure to finally have the opportunity to thank my parents and my brother for all the support over all these years. Last but not least: SANDY, for your invaluable support and love. Thanks!

Bibliography

It has to be noted that the date shown at the article citations is the *first* date the article was published – either electronically or via a print edition.

- [1] LAPO BOGANI et al. »Continuous modulation of the magnetic hysteresis of CoNi alloy nanoparticles by light«. Unpublished.
- [2] ANDREW MCWILLIAMS. *Global Markets for Nanocomposites, Nanoparticles, Nanoclays, and Nanotubes*. Wellesley, MA 02481 USA: BCC Research, May 2014. URL: <http://www.bccresearch.com/market-research/nanotechnology/nanocomposites-market-nan021f.html>
- [3] AN-HUI LU, ELENA-LORENA SALABAŞ and FERDI SCHÜTH. »Magnetic Nanoparticles: Synthesis, Protection, Functionalization, and Application«. In: *Angewandte Chemie International Edition. Review*, Vol. 46.8 (5th Feb. 2007), pp. 1222–1244. DOI: 10.1002/anie.200602866
- [4] TETSUYA OSAKA et al. »Synthesis of magnetic nanoparticles and their application to bioassays«. In: *Analytical and Bioanalytical Chemistry*, Vol. 384.3 (4th Jan. 2006), pp. 593–600. DOI: 10.1007/s00216-005-0255-7
- [5] AN-HUI LU et al. »Nanoengineering of a Magnetically Separable Hydrogenation Catalyst«. In: *Angewandte Chemie International Edition*, Vol. 43.33 (13th Aug. 2004), pp. 4303–4306. DOI: 10.1002/anie.200454222
- [6] HUI S. HUANG and JAMES F. HAINFELD. »Intravenous magnetic nanoparticle cancer hyperthermia«. In: *International Journal of Nanomedicine*, Vol. 8.1 (17th July 2013), pp. 2521–2532. DOI: 10.2147/IJN.S43770
- [7] JERED B. HAUN, TAE-JONG YOON, HAKHO LEE and RALPH WEISSLEDER. »Molecular Detection of Biomarkers and Cells Using Magnetic Nanoparticles and Diagnostic Magnetic Resonance«. In: *Biomedical Nanotechnology*. Ed. by SARAH J. HURST. Vol. 726. *Methods in Molecular Biology*. Humana Press, 16th Feb. 2011, pp. 33–49. DOI: 10.1007/978-1-61779-052-2_3

- [8] GÜNTER REISS and ANDREAS HÜTTEN. »Magnetic nanoparticles: Applications beyond data storage«. In: *Nature Materials*, Vol. 4.10 (Oct. 2005), pp. 725–726. DOI: 10.1038/nmat1494
- [9] SERGEY P. GUBIN. *Introduction*. In: *Magnetic Nanoparticles*. Wiley-VCH Verlag GmbH & Co. KGaA, 16th Sept. 2009, pp. 1–23. DOI: 10.1002/9783527627561
- [10] ALEXANDRE TAMION, MATTHIAS HILLENKAMP, FLORENT TOURNUS, EDGAR BONET and VÉRONIQUE DUPUIS. »Accurate determination of the magnetic anisotropy in cluster-assembled nanostructures«. In: *Applied Physics Letters*, Vol. 95.6 (10th Aug. 2009). DOI: 10.1063/1.3200950
- [11] EDMUND C. STONER and ERICH P. WOHLFARTH. »A Mechanism of Magnetic Hysteresis in Heterogeneous Alloys«. In: *Philosophical Transactions of the Royal Society of London, Series A, Mathematical and Physical Sciences*, Vol. 240.826 (4th May 1948), pp. 599–642. DOI: 10.1098/rsta.1948.0007
- [12] DAVID C. JILES and DAVID L. ATHERTON. »Theory of ferromagnetic hysteresis (invited)«. In: *Journal of Applied Physics*, Vol. 55.6 (15th Mar. 1984), pp. 2115–2120. DOI: 10.1063/1.333582
- [13] FERENC PREISACH. »Über die magnetische Nachwirkung«. German. In: *Zeitschrift für Physik*, Vol. 94.5-6 (15th Feb. 1935), pp. 277–302. DOI: 10.1007/BF01349418
- [14] STEPHAN BARCIKOWSKI, ANNE HAHN, MERLIN GUGGENHEIM, KERSTIN REIMERS and ANDREAS OSTENDORF. »Biocompatibility of nanoactuators: stem cell growth on laser-generated nickel–titanium shape memory alloy nanoparticles«. In: *Journal of Nanoparticle Research*, Vol. 12.5 (12th Mar. 2010), pp. 1733–1742. DOI: 10.1007/s11051-009-9834-4
- [15] GEORGE B. KAUFFMAN and ISAAC MAYO. »The Story of Nitinol: The Serendipitous Discovery of the Memory Metal and Its Applications«. In: *The Chemical Educator*, Vol. 2.2 (1st June 1997), pp. 1–21. DOI: 10.1007/s00897970111a
- [16] SARAH STRAUSS, ANNE HAHN, STEPHAN BARCIKOWSKI, KERSTIN REIMERS and PETER M. VOGT. »Implantat Optimierung mittels Nitinol-Nanobeschichtungen«. German. In: *Chirurgisches Forum und DGAV Forum 2010*. Ed. by REINER GRADINGER, MICHAEL D. MENGER and HANS-JOACHIM MEYER. Vol. 39. Deutsche Gesellschaft für Chirurgie. Springer

- Berlin Heidelberg, 2010, pp. 259–260. DOI: 10.1007/978-3-642-12192-0_99
- [17] SATOSHI HORIKOSHI and NICK SERPONE. *Introduction to Nanoparticles*. In: *Microwaves in Nanoparticle Synthesis*. Wiley-VCH Verlag GmbH & Co. KGaA, 26th Apr. 2013, pp. 1–24. DOI: 10.1002/9783527648122.ch1
- [18] ISO/TS 27687:2008(en): *Nanotechnologies – Terminology and definitions for nano-objects – Nanoparticle, nanofibre and nanoplate*. International Organization for Standardization. Geneva. URL: www.iso.org/iso/catalogue_detail?csnumber=44278. Published.
- [19] AMANDA L. WILLIS, NICHOLAS J. TURRO and STEPHEN O'BRIEN. »Spectroscopic Characterization of the Surface of Iron Oxide Nanocrystals«. In: *Chemistry of Materials*, Vol. 17.24 (4th Nov. 2005), pp. 5970–5975. DOI: 10.1021/cm051370v
- [20] YONGCHAO LAI, WEIWEI YIN, JINTING LIU, RIMO XI and JINHUA ZHAN. »One-Pot Green Synthesis and Bioapplication of L-Arginine-Capped Superparamagnetic Fe₃O₄ Nanoparticles«. In: *Nanoscale Research Letters*, Vol. 5.2 (13th Nov. 2009), pp. 302–307. DOI: 10.1007/s11671-009-9480-x
- [21] XUN WANG, JING ZHUANG, QING PENG and YADONG LI. »A general strategy for nanocrystal synthesis«. In: *Nature*, Vol. 437.7055 (1st Sept. 2005), pp. 121–124. DOI: 10.1038/nature03968
- [22] LOUIS FRANZEL, MASSIMO F. BERTINO, ZACHARY J. HUBA and EVERETT E. CARPENTER. »Synthesis of magnetic nanoparticles by pulsed laser ablation«. In: *Applied Surface Science*, Vol. 261 (14th Aug. 2012), pp. 332–336. DOI: 10.1016/j.apsusc.2012.08.010
- [23] VINCENZO AMENDOLA and MORENO MENEGHETTI. »Laser ablation synthesis in solution and size manipulation of noble metal nanoparticles«. In: *Physical Chemistry Chemical Physics*, Vol. 11.20 (1st Apr. 2009), pp. 3805–3821. DOI: 10.1039/B900654K
- [24] GIOVANNI MATTEI et al. »Synthesis, Structure, and Magnetic Properties of Co, Ni, and Co–Ni Alloy Nanocluster-Doped SiO₂ Films by Sol–Gel Processing«. In: *Chemistry of Materials*, Vol. 14.8 (12th July 2002), pp. 3440–3447. DOI: 10.1021/cm021106r

- [25] CHAO LIU, ADAM J. RONDINONE and Z. JOHN ZHANG. »Synthesis of magnetic spinel ferrite CoFe_2O_4 nanoparticles from ferric salt and characterization of the size-dependent superparamagnetic properties«. In: *Pure and Applied Chemistry*, Vol. 72.1-2 (Feb. 2000): *Special Topic Issue on the Theme of Nanostructured Systems*, pp. 37–45. DOI: 10.1351/pac200072010037
- [26] JenLas® D2.fs IR & Green Femtosecond Laser Series. Specifications. JENOPTIK AG. 07739 Jena, Germany, Dec. 2013. URL: [http://www.jenoptik.com/cms/products.nsf/0/D528AAFD40D6C5B2C1257C3E005D6708/\\$File/201312_d2.fs_series_en.pdf](http://www.jenoptik.com/cms/products.nsf/0/D528AAFD40D6C5B2C1257C3E005D6708/$File/201312_d2.fs_series_en.pdf) (visited on 16th Sept. 2014)
- [27] NIKOLAOS G. SEMALTIANOS. »Nanoparticles by Laser Ablation«. In: *Critical Reviews in Solid State and Materials Sciences*, Vol. 35.2 (8th June 2010), pp. 105–124. DOI: 10.1080/10408431003788233
- [28] M`BAREK CHAKIF et al. »Impact of solvent mixture on iron nanoparticles generated by laser ablation«. In: *Colloidal Nanoparticles for Biomedical Applications IX. Proceedings of SPIE*. Ed. by WOLFGANG J. PARAK, MAREK OSIŃSKI and KENJI I. YAMAMOTO. Vol. 8955. Society of Photo-Optical Instrumentation Engineers. Bellingham, Washington, USA, 24th Mar. 2014, pp. 895507-1–895507-9. DOI: 10.1117/12.2037682
- [29] JIANHUA LIN, SHENGFENG LIU, XIAOLIANG QIAN, JIUMA BAYI and MIANZENG SU. »Synthesis of $\text{Nd}_2\text{Fe}_{17}$ by reduction-diffusion process«. In: *Journal of Alloys and Compounds*, Vol. 238.1–2 (1st May 1996), pp. 113–115. DOI: 10.1016/0925-8388(95)02130-2
- [30] JIAN-PING WANG, DE-HUA HAN, HE-LIE LUO, NEI-FAI GAO and YUAN-YUAN LIU. »Preparation and magnetic properties of $\text{Fe}_{100-x}\text{Ni}_x-\text{SiO}_2$ granular alloy solid using a sol-gel method«. In: *Journal of Magnetism and Magnetic Materials*, Vol. 135.3 (Aug. 1994), pp. L251–L256. DOI: 10.1016/0304-8853(94)90354-9
- [31] C. JEFFREY BRINKER, GREGORY C. FRYE, ALAN J. HURD and CAROL S. ASHLEY. »Fundamentals of sol-gel dip coating«. In: *Thin Solid Films*, Vol. 201.1 (5th June 1991), pp. 97–108. DOI: 10.1016/0040-6090(91)90158-T
- [32] TYRION L. *Details of Sol-Gel dip coating process*. 12th Nov. 2008. URL: http://commons.wikimedia.org/w/index.php?title=File:SolGel_DipCoating2.jpg&oldid=69253794 (visited on 8th Oct. 2014)

- [33] LARRY L. HENCH and JON K. WEST. »The sol-gel process«. In: *Chemical Reviews*, Vol. **90**.1 (Jan. 1990), pp. 33–72. DOI: 10.1021/cr00099a003
- [34] SIEGFRIED HUNKLINGER. *Festkörperphysik*. German. 2nd ed. Oldenbourg Wissenschaftsverlag GmbH, 2009. 595 pp. DOI: 10.1524/9783486596410
- [35] STEPHEN BLUNDELL. *Magnetism in Condensed Matter*. Vol. 4. Oxford Master Series in Condensed Matter Physics. Oxford University Press, 4th Oct. 2001. 256 pp. URL: <http://ukcatalogue.oup.com/product/9780198505914.do>
- [36] PIERRE WEISS. »L'hypothèse du champ moléculaire et la propriété ferromagnétique«. French. In: *Journal de Physique Théorique et Appliquée*, Vol. **6**.1 (4th Apr. 1907), pp. 661–690. DOI: 10.1051/jphystap:019070060066100
- [37] MANUEL ARRUEBO, RODRIGO FERNÁNDEZ-PACHECO, MANUEL IBARRA GARCÍA and JESÚS SANTAMARÍA. »Magnetic nanoparticles for drug delivery«. In: *Nano Today*, Vol. **2**.3 (June 2007), pp. 22–32. DOI: 10.1016/S1748-0132(07)70084-1
- [38] FLORENT TOURNUS and ALEXANDRE TAMION. »Magnetic susceptibility curves of a nanoparticle assembly II. Simulation and analysis of ZFC/FC curves in the case of a magnetic anisotropy energy distribution«. In: *Journal of Magnetism and Magnetic Materials*, Vol. **323**.9 (20th Nov. 2010), pp. 1118–1127. DOI: 10.1016/j.jmmm.2010.11.057
- [39] FLORENT TOURNUS and EDGAR BONET. »Magnetic susceptibility curves of a nanoparticle assembly, I: Theoretical model and analytical expressions for a single magnetic anisotropy energy«. In: *Journal of Magnetism and Magnetic Materials*, Vol. **323**.9 (20th Nov. 2010), pp. 1109–1117. DOI: 10.1016/j.jmmm.2010.11.056
- [40] SERGEI P. GUBIN, YURII A. KOKSHAROV, GENNADY B. KHOMUTOV and GLEB Y. YURKOV. »Magnetic nanoparticles: preparation, structure and properties«. In: *Russian Chemical Reviews*, Vol. **74**.6 (2005), pp. 489–520. DOI: 10.1070/RC2005v074n06ABEH000897
- [41] DIMITRIS KECHRAKOS. *Magnetic Nanoparticle Assemblies*. In: *Nanoparticles and Quantum Dots*. Ed. by KLAUS D. SATTLER. Handbook of Nanophysics 3. CRC Press, Sept. 2010. Chap. 22, pp. 22-1–22-16

- [42] ALBERTO P. GUIMARÃES. *Principles of Nanomagnetism*. Ed. by PHAEDON AVOURIS et al. NanoScience and Technology. Springer, Oct. 2009. DOI: 10.1007/978-3-642-01482-6
- [43] ARATI G. KOLHATKAR, ANDREW JAMISON, DMITRI LITVINOV, RICHARD C. WILLSON and T. RANDALL LEE. »Tuning the Magnetic Properties of Nanoparticles«. In: *International Journal of Molecular Sciences*, Vol. 14.8 (31st July 2013), pp. 15977–16009. DOI: 10.3390/ijms140815977
- [44] *Introduction to: AC Susceptibility*. Quantum Design. San Diego, CA 92121, USA, 16th Mar. 2010. 4 pp. URL: <http://www.qdusa.com/sitedocs/appNotes/ppms/1078-201.pdf>
- [45] NATALIE A. FREY and SHOUHENG SUN. *Magnetic Nanoparticle for Information Storage Applications*. In: *Inorganic Nanoparticles: Synthesis, Applications, and Perspectives*. Ed. by CLAUDIA ALTAVILLA and ENRICO CILIBERTO. 19th Nov. 2010, pp. 33–68
- [46] SRIKANTH SINGAMANENI, VALERY N. BLIZNYUK, CHRISTIAN BINEK and EVGENY Y. TSYMBAL. »Magnetic nanoparticles: recent advances in synthesis, self-assembly and applications«. In: *Journal of Materials Chemistry*, Vol. 21.42 (11th Aug. 2011), pp. 16819–16845. DOI: 10.1039/C1JM11845E
- [47] HENG HUANG, SAVAS DELIKANLI, HAO ZENG, DENISE M. FERKEY and ARND PRALLE. »Remote control of ion channels and neurons through magnetic-field heating of nanoparticles«. In: *Nature Nanotechnology*, Vol. 5.8 (27th June 2010), pp. 602–606. DOI: 10.1038/nnano.2010.125
- [48] ERIC JENSEN. *Example: Transmission Electron Microscope System*. 18th Nov. 2012. URL: <http://www.texample.net/tikz/examples/transmission-electron-microscope/>
- [49] MAX KNOLL and ERNST RUSKA. »Das Elektronenmikroskop«. German. In: *Zeitschrift für Physik*, Vol. 78.5-6 (16th June 1932), pp. 318–339. DOI: 10.1007/BF01342199
- [50] DAVID B. WILLIAMS and C. BARRY CARTER. *Transmission Electron Microscopy. A Textbook for Materials Science*. Springer US, 2009. DOI: 10.1007/978-0-387-76501-3
- [51] JITKANG LIM, SWEE P. YEAP, HUI X. CHE and SIEW C. LOW. »Characterization of magnetic nanoparticle by dynamic light scattering«. In: *Nanoscale*

- Research Letters*, Vol. 8.1 (8th Sept. 2013), p. 381. DOI: 10.1186/1556-276X-8-381
- [52] M'BAREK CHAKIF. *Herstellung, Eigenschaften und strukturelle Untersuchung von lasergenerierten NiTi-Nanopartikeln*. German. PhD thesis. Ruhr-Universität Bochum, 4th June 2014. URN: urn:nbn:de:hbz:294-42094
- [53] JOHN C. RIVIÈRE and SVERRE MYHRA. *Handbook of Surface and Interface Analysis. Methods for Problem-Solving*. 2nd ed. CRC Press, June 2009. DOI: 10.1201/9781420007800
- [54] BRIAN D. JOSEPHSON. »Possible new effects in superconductive tunneling«. In: *Physics Letters*, Vol. 1.7 (8th June 1962), pp. 251–253. DOI: 10.1016/0031-9163(62)91369-0
- [55] ROBERT C. JAKLEVIC, JOHN J. LAMBE, ARNOLD H. SILVER and JAMES E. MERCEREAU. »Quantum Interference Effects in Josephson Tunneling«. In: *Physical Review Letters*, Vol. 12.7 (17th Feb. 1964), pp. 159–160. DOI: 10.1103/PhysRevLett.12.159
- [56] RANDALL C. BLACK and FREDERICK C. WELLSTOOD. *Measurements of Magnetism and Magnetic Properties of Matter*. In: *The SQUID Handbook. Vol. II Applications of SQUIDS and SQUID Systems*. Ed. by JOHN CLARKE and ALEX I. BRAGINSKI. Wiley-VCH Verlag GmbH & Co. KGaA, 11th Dec. 2006. DOI: 10.1002/9783527609956
- [57] ROBERT L. FAGALY. »Superconducting quantum interference device instruments and applications«. In: *Review of Scientific Instruments*, Vol. 77.10, 101101 (11th Oct. 2006). DOI: 10.1063/1.2354545
- [58] JOHN CLARKE and ALEX I. BRAGINSKI, eds. *The SQUID Handbook. Fundamentals and Technology of SQUIDS and SQUID Systems, Volume I*. Wiley-VCH Verlag GmbH & Co. KGaA, 11th May 2005. DOI: 10.1002/3527603646
- [59] JOHN CLARKE and ALEX I. BRAGINSKI, eds. *The SQUID Handbook. Applications of SQUIDS and SQUID Systems, Volume II*. Wiley-VCH Verlag GmbH & Co. KGaA, 11th Dec. 2006. DOI: 10.1002/9783527609956
- [60] MIKE MCELFRISH. *Fundamentals of Magnetism and Magnetic Measurements. Featuring Quantum Design's Magnetic Property Measurement System*. Quantum Design, Inc.; San Diego, CA 92121, USA, 1994. 34 pp. URL: <http://www.qdusa.com/sitedocs/appNotes/mpms/FundPrimer.pdf>

- [61] WALTER FRIEDRICH, PAUL KNIPPING and MAX VON LAUE. »Interferenzerscheinungen bei Röntgenstrahlen«. German. In: *Annalen der Physik*, Vol. 346.10 (1913), pp. 971–988. DOI: 10.1002/andp.19133461004
- [62] WILLIAM L. BRAGG. »The Diffraction of Short Electromagnetic Waves by a Crystal«. In: *Proceedings of the Cambridge Philosophical Society*, Vol. 17 (1913), pp. 43–57. URL: <https://archive.org/stream/proceedingsofcam1718191316camb#page/n59/mode/2up>
- [63] The International Centre for Diffraction Data. URL: <http://www.icdd.com/> (visited on 25th Oct. 2014)
- [64] RAVI SHARMA, DURGA P. BISEN, USHA SHUKLA and BALGOPAL SHARMA. »X-ray diffraction: a powerful method of characterizing nanomaterials«. In: *Recent Research in Science and Technology*, Vol. 4.8 (19th Oct. 2012), pp. 77–79. URL: <http://recent-science.com/index.php/rrst/article/view/14887>
- [65] MAXIM M. NOGINOV et al. »Magnetic resonance in iron oxide nanoparticles: Quantum features and effect of size«. In: *Journal of Magnetism and Magnetic Materials*, Vol. 320.18 (2nd May 2008), pp. 2228–2232. DOI: 10.1016/j.jmmm.2008.04.154
- [66] PETER ATKINS and JULIO DE PAULA. *Physical Chemistry*. 10th ed. Oxford University Press, 20th Mar. 2014. 1040 pp. URL: <http://ukcatalogue.oup.com/product/9780199697403.do> (visited on 3rd Nov. 2014)
- [67] JOHN M. D. COEY. *Magnetism and Magnetic Materials*. Cambridge Books Online. Cambridge University Press, 2010. DOI: 10.1017/CB09780511845000
- [68] CHARBEL TANNOUS and JACEK GIERALTOWSKI. »The Stoner-Wohlfarth model of Ferromagnetism: Static properties«. Version 3. In: arXiv: physics/0607117 [physics.class-ph] (25th Apr. 2008)
- [69] CHARBEL TANNOUS and JACEK GIERALTOWSKI. »The Stoner-Wohlfarth model of Ferromagnetism: Dynamic and Statistical properties«. Version 4. In: arXiv: physics/0607118 [physics.class-ph] (25th Apr. 2008)
- [70] ALEXANDRU STANCU. *The Stoner-Wohlfarth Model*. MAGMANet. URL: http://wwwold.unizar.es/magmanet/magmanet-eu/index.php?/topic_1_0.html (visited on 10th July 2014)

- [71] ALEXANDRU STANCU and IRINEL CHIORESCU. »Crossover condition in the coherent rotation model and the Preisach-type models«. In: *IEEE Transactions on Magnetics*, Vol. 33.4 (July 1997), pp. 2573–2579. DOI: 10.1109/20.595917
- [72] ANDRÉ THIAVILLE. »Extensions of the geometric solution of the two dimensional coherent magnetization rotation model. Dedicated to John Slonczewski on the occasion of the fortieth anniversary of his pioneering paper.« In: *Journal of Magnetism and Magnetic Materials*, Vol. 182.1–2 (1st Feb. 1998), pp. 5–18. DOI: [http://dx.doi.org/10.1016/S0304-8853\(97\)01014-7](http://dx.doi.org/10.1016/S0304-8853(97)01014-7)
- [73] DANIEL ORTEGA. *Structure and Magnetism in Magnetic Nanoparticles*. In: *Magnetic Nanoparticles. From Fabrication to Clinical Applications*. Ed. by NGUYỄN T. K. THANH. CRC Press, 1st Feb. 2012. Chap. 1, pp. 3–44. DOI: 10.1201/b11760-3
- [74] JOSEPH A. CHRISTODOULIDES et al. »Intrinsic and hysteresis properties of FePt nanoparticles«. In: *Physical Review B. condensed matter and materials physics*, Vol. 68.5 (27th Aug. 2003), p. 054428. DOI: 10.1103/PhysRevB.68.054428
- [75] DOMINIQUE GIVORD, MICHEL-FRANÇOIS ROSSIGNOL and DAVID W. TAYLOR. »Coercivity mechanisms in hard magnetic materials«. In: *Journal de Physique IV*, Vol. 2.C3 (Dec. 1992), pp. C3-95–C3-104. DOI: 10.1051/jp4:1992314
- [76] ROGER J. ELLIOTT. »Theory of the Effect of Spin-Orbit Coupling on Magnetic Resonance in Some Semiconductors«. In: *Physical Review*, Vol. 96.2 (15th Oct. 1954), pp. 266–279. DOI: 10.1103/PhysRev.96.266
- [77] YAKOV YAFET. »Conduction electron spin relaxation in the superconducting state«. In: *Physics Letters A*, Vol. 98.5–6 (24th Oct. 1983), pp. 287–290. DOI: 10.1016/0375-9601(83)90874-5
- [78] MANFRED FÄHNLE and CHRISTIAN ILLG. »Electron theory of fast and ultrafast dissipative magnetization dynamics«. In: *Journal of Physics: Condensed Matter*, Vol. 23.49 (17th Nov. 2011), p. 493201. DOI: 10.1088/0953-8984/23/49/493201
- [79] OLIVIER MARGEAT, MARC RESPAUD, CATHERINE AMIENS, PIERRE LECANTE and BRUNO CHAUDRET. »Ultrafine metallic Fe nanoparticles: syn-

- thesis, structure and magnetism«. In: *Beilstein Journal of Nanotechnology*, Vol. 1 (3rd Dec. 2010), pp. 108–118. DOI: 10.3762/bjnano.1.13
- [80] IGOR ŽUTIĆ, JAROSLAV FABIAN and S. DAS SARMA. »Spintronics: Fundamentals and applications«. In: *Reviews of Modern Physics*, Vol. 76.2 (Apr. 2004), pp. 323–410. DOI: 10.1103/RevModPhys.76.323
- [81] RAMAKRISHNAN VENKATARAMAN. *Modeling and Adaptive Control of Magnetostrictive Actuators*. PhD thesis. Center for Dynamics and Control of Smart Structures, University of Maryland, 1999. 228 pp. URL: <http://hdl.handle.net/1903/6043> (visited on 4th Sept. 2014)
- [82] DAVID C. JILES and DAVID L. ATHERTON. »Theory of ferromagnetic hysteresis«. In: *Journal of Magnetism and Magnetic Materials*, Vol. 61.1–2 (21st Jan. 1986), pp. 48–60. DOI: 10.1016/0304-8853(86)90066-1
- [83] VLADO OSTOVIC. *Computer-aided Analysis of Electric Machines. A Mathematica approach*. 1st ed. Prentice Hall, 1994. 520 pp.
- [84] ROMAN SZEWCZYK. »Computational Problems Connected with Jiles-Atherton Model of Magnetic Hysteresis«. In: *Recent Advances in Automation, Robotics and Measuring Techniques*. Ed. by ROMAN SZEWCZYK, CEZARY ZIELIŃSKI and MAŁGORZATA KALICZYŃSKA. Vol. 267. *Advances in Intelligent Systems and Computing*. Springer International Publishing, 2014, pp. 275–283. DOI: 10.1007/978-3-319-05353-0_27
- [85] DAVID C. JILES, JENNIFER B. THOELKE and MICHAEL K. DEVINE. »Numerical determination of hysteresis parameters for the modeling of magnetic properties using the theory of ferromagnetic hysteresis«. In: *IEEE Transactions on Magnetics*, Vol. 28.1 (Jan. 1992), pp. 27–35. DOI: 10.1109/20.119813
- [86] NICUSOR C. POP and OVIDIU F. CĂLȚUN. »Jiles–Atherton Magnetic Hysteresis Parameters Identification«. In: *Acta Physica Polonica A*, Vol. 120.3 (23rd Feb. 2011). URL: <http://przyrbwn.icm.edu.pl/APP/ABSTR/120/a120-3-22.html> (visited on 13th Dec. 2014)
- [87] VINCENZO AMENDOLA et al. »Magnetic iron oxide nanoparticles with tunable size and free surface obtained via a ›green‹ approach based on laser irradiation in water«. In: *Journal of Materials Chemistry*, Vol. 21.46 (25th Oct. 2011), pp. 18665–18673. DOI: 10.1039/C1JM13680A

- [88] W. HENRY WALTON. »FERET'S Statistical Diameter as a Measure of Particle Size«. In: *Nature. Letters to the Editor*, Vol. **162** (28th Aug. 1948), pp. 329–330. DOI: 10.1038/162329b0
- [89] VINCENZO AMENDOLA and MORENO MENEGHETTI. »Controlled size manipulation of free gold nanoparticles by laser irradiation and their facile bioconjugation«. In: *Journal of Materials Chemistry*, Vol. **17.44** (26th Sept. 2007), pp. 4705–4710. DOI: 10.1039/B709621F
- [90] PHILIPPE SPIGA et al. »Investigation of nanoparticle formation in a plasma produced by femtosecond laser ablation of gold«. In: *AIP Conference Proceedings*, Vol. **799.1** (31st Oct. 2005), pp. 197–200. DOI: 10.1063/1.2134599
- [91] IĀKOV I. KHANIN. *Principles of Laser Dynamics*. 1st ed. Amsterdam: Elsevier, 1995. DOI: 10.1016/B978-0-444-89696-4.50011-0
- [92] OLIVER PANZER and HARALD FUCHS. *moderne oberflächen-analytik*. German. Kompetenzzentrum für Nanoanalytik in Münster. URL: http://www.centech.de/media/ccn_techniques.pdf (visited on 5th Dec. 2014)
- [93] NATARAJAN VENKATARAMANAN, ROYOJI SAHARA, HIROSHI MIZUSEKI and YOSHIYUKI KAWAZOE. »Titanium-Doped Nickel Clusters TiNi_n (n = 1–12): Geometry, Electronic, Magnetic, and Hydrogen Adsorption Properties«. In: *The Journal of Physical Chemistry A*, Vol. **114.15** (24th Mar. 2010). PMID: 20334429, pp. 5049–5057. DOI: 10.1021/jp100459c
- [94] HO CHANG and YI-CHUN HSU. »Fabrication and material properties of NiTi nanofluid«. In: *Journal of Vacuum Science & Technology B*, Vol. **25.3** (24th May 2007), pp. 935–939. DOI: 10.1116/1.2740286
- [95] RALPH V. CHAMBERLIN. »Mean-field cluster model for the critical behaviour of ferromagnets«. In: *Nature*, Vol. **408.6810** (16th Nov. 2000), pp. 337–339. DOI: 10.1038/35042534
- [96] *Encyclopædia Britannica. titanium (Ti)*. URL: <http://www.britannica.com/EBchecked/topic/597135/titanium-Ti> (visited on 17th Nov. 2014)
- [97] SURENDRA D. TIWARI and K. P. RAJEEV. »Magnetic properties of NiO nanoparticles«. In: *Thin Solid Films*, Vol. **505.1–2** (18th May 2006), pp. 113–117. DOI: 10.1016/j.tsf.2005.10.019
- [98] SURENDRA D. TIWARI and K. P. RAJEEV. »Magnetic Susceptibility of NiO Nanoparticles«. Version 1. In: arXiv: cond-mat/0408427 [cond-mat.soft] (19th Aug. 2004)

- [99] PAUL M. SHAND et al. »Spin glass or random anisotropy?: The origin of magnetically glassy behavior in nanostructured GdAl_2 «. In: *Journal of Applied Physics*, Vol. **97**.10 (12th May 2005), 10J505–10J505-3. DOI: 10.1063/1.1853003
- [100] TERUO BITOH. *Magnetic Properties of Superparamagnetic Fine Particles: Comparison with Spin Glass*. PhD thesis. Mizumotochō: Muroran Institute of Technology, 22nd Dec. 1993. URL: http://www.akita-pu.ac.jp/system/mise/material_structure/bitoh/thesis/thesis_bitoh.pdf (visited on 3rd Dec. 2014)
- [101] TODD MEGLICH et al. *Characterization of frequency dependent magnetic susceptibility in UXO electromagnetic geophysics*. In: *SEG Technical Program Expanded Abstracts 2008*. Society of Exploration Geophysicists, Jan. 2008. Chap. 250, pp. 1248–1252. DOI: 10.1190/1.3059142
- [102] V. TKÁČ et al. »Multiple-timescale relaxation dynamics in $\text{CsGd}(\text{MoO}_4)_2$ — a dipolar magnet with a highly anisotropic layered crystal structure«. In: *Journal of Physics: Condensed Matter*, Vol. **25**.50 (25th Nov. 2013), p. 506001. DOI: 10.1088/0953-8984/25/50/506001
- [103] GARY R. OLHOEFT and DAVID W. STRANGWAY. »Magnetic relaxation and the electromagnetic response parameter«. In: *Geophysics*, Vol. **39**.3 (June 1974), pp. 302–311. DOI: 10.1190/1.1440429
- [104] AMRUT S. LANJE, SATISH J. SHARMA and RAMCHANDRA B. PODE. »Magnetic and Electrical Properties of Nickel Nanoparticles prepared by Hydrazine Reduction Method«. In: *Archives of Physics Research*, Vol. **1**.1 (2010), pp. 49–56. URL: <http://scholarsresearchlibrary.com/APR-vol1-iss1/APR-2010-1-1-49-56.html> (visited on 11th Dec. 2014)
- [105] CAI LEI YUAN. »Room-Temperature Coercivity of Ni/NiO Core/Shell Nanoparticles Fabricated by Pulsed Laser Deposition«. In: *The Journal of Physical Chemistry C*, Vol. **114**.5 (12th Jan. 2010), pp. 2124–2126. DOI: 10.1021/jp911015b
- [106] WILLIAM H. MEIKLEJOHN and CHARLES P. BEAN. »New Magnetic Anisotropy«. In: *Physical Review*, Vol. **105**.3 (1st Feb. 1957), pp. 904–913. DOI: 10.1103/PhysRev.105.904

- [107] MARK G. BLAMIRE. »Unconventional Exchange Bias and Multiferroics«. In: *IEEE Transactions on Magnetics*, Vol. **44.7** (July 2008), pp. 1946–1950. DOI: 10.1109/TMAG.2008.924541
- [108] PING ZHANG et al. »Irreversible magnetization in nickel nanoparticles«. In: *Journal of Magnetism and Magnetic Materials*, Vol. **225.3** (20th Apr. 2001), pp. 337–345. DOI: 10.1016/S0304-8853(00)01379-2
- [109] DO-GUWN HWANG, SANG-SUK LEE and CHANG-MAN PARK. »Anisotropic roughness effects of magnetoresistive hysteresis in scratched NiO spin valves«. In: *Journal of Magnetism and Magnetic Materials*, Vol. **198–199** (1st June 1999), pp. 39–42. DOI: 10.1016/S0304-8853(98)00612-X
- [110] DO-GUWN HWANG, SANG-SUK LEE and CHANG-MAN PARK. »Effect of roughness slope on exchange biasing in NiO spin valves«. In: *Applied Physics Letters*, Vol. **72.17** (27th Feb. 1998), pp. 2162–2164. DOI: 10.1063/1.121308
- [111] JOSEP NOGUÉS and IVAN K. SCHULLER. »Exchange bias«. In: *Journal of Magnetism and Magnetic Materials*, Vol. **192.2** (15th Feb. 1999), pp. 203–232. DOI: 10.1016/S0304-8853(98)00266-2
- [112] RUTH MAGAYE et al. »Metallic Nickel Nanoparticles May Exhibit Higher Carcinogenic Potential than Fine Particles in JB6 Cells«. In: *PLoS ONE*, Vol. **9.4** (1st Apr. 2014). Ed. by YUNLI ZHOU, e92418-1–e92418-9. DOI: 10.1371/journal.pone.0092418
- [113] ALAM ABEDINI, ABDUL R. DAUD, MUHAMMAD A. ABDUL HAMID and NORINSAN KAMIL OTHMAN. »Radiolytic Formation of Fe₃O₄ Nanoparticles: Influence of Radiation Dose on Structure and Magnetic Properties«. In: *PLoS ONE*, Vol. **9.3** (7th Mar. 2014), e90055-1–e90055-8. DOI: 10.1371/journal.pone.0090055
- [114] ING KONG, SAHRIM H. AHMAD, MUSTAFFA H. ABDULLAH and AHMAD N. YUSOFF. »The Effect Of Temperature On Magnetic Behavior Of Magnetite Nanoparticles And Its Nanocomposites«. In: *AIP Conference Proceedings*, Vol. **1136.1** (1st June 2009), pp. 830–834. DOI: 10.1063/1.3160267
- [115] STEEN MØRUP, MIKKEL F. HANSEN and CATHRINE FRANDBSEN. »Magnetic Nanoparticles«. In: *Comprehensive Nanoscience and Technology*. Ed. by DAVID L. ANDREWS, GREGORY D. SCHOLLES and GARY P. WIEDERRECHT. Vol. **1**. Amsterdam: Academic Press, Nov. 2010. Chap. 14, pp. 437–491. DOI: 10.1016/B978-0-12-374396-1.00036-2

- [116] MANH-THUONG NGUYEN, NICOLA SERIANI, SIMONE PICCININ and RALPH GEBAUER. »Photo-driven oxidation of water on α -Fe₂O₃ surfaces: An ab initio study«. In: *The Journal of Chemical Physics*, Vol. **140**.6, 064703 (14th Feb. 2014). DOI: 10.1063/1.4865103
- [117] KURT MEYBERG and PETER VACHENAUER. *Höhere Mathematik. Differentialgleichungen, Funktionentheorie, Fourier-Analyse, Variationsrechnung*. German. 4th ed. 2003. 457 pp. DOI: 10.1007/978-3-642-56655-4

List of Figures

2.1.	Experimental LASiS setup	29
2.2.	Sketched modus operandi of the sol-gel dip-coating process.	32
2.3.	Possible antiferromagnetic spin orientation changes with an applied external field.	35
2.4.	Explanatory curves of field-dependent magnetisation and ZFC-FC measurements.	38
3.1.	Schematic drawing of a TEM	41
3.2.	Schematic drawing of the principle exploited for EDX measurements	43
3.3.	Schematic drawing of a SQUID-magnetometer.	44
4.1.	Simulations of equation (4.2) with variations of D_m , w , M_{sat} and T	52
4.2.	$m(H)$ measurement of pure Ni nanoparticles with corresponding fits and particle size distribution as measured and as a result of the fitting	53
4.3.	Schematic drawing of a SW particle	56
4.4.	STONER-WOHLFARTH-astroïd and sample curve in the simple SW model with $\theta_0 = 60^\circ$	58
4.5.	Construction of the crossover in the standard SW model and corresponding hystereses.	59
4.6.	Comparison of H_c and H_{cr} for a SW particle with $\theta = 70^\circ$	61
4.7.	Flowchart of the <i>Mathematica</i> simulation code.	63
4.8.	Spin dependent scattering of electrons and schematical view of the density of states of a single nanoparticle with an applied field	65
4.9.	Fits of the angularly restricted STONER-WOHLFARTH model to data from $\text{Co}_{50}\text{Ni}_{50}$ and Fe nanoparticles	67
4.10.	Contour plot of the angularly restricted extended STONER-WOHLFARTH model in dependence of starting and ending angle and example hystereses belonging to certain points of the contour plot	68
4.11.	Simulation of a hysteresis with the extended JILES-ATHERTON model.	70

5.1.	TEM images of nitinol nanoparticles	74
5.2.	Size probability density for NiTi nanoparticles produced in water	75
5.3.	Overview of the steps taken to prepare the nanoparticle samples for SQUID measurements.	76
5.4.	Results of EDX measurements of NiTi nanoparticles depending on the used liquid and plot of O at% in nanoparticles vs. liquid	79
5.5.	Hysteresis measurements on different nitinol nanoparticles at 20 K.	81
5.6.	ZFC-FC measurements with an applied field of 0.1 T on NiTi nanoparticles	83
5.7.	Contour plots of ZFC and FC measurements depending on temperature and the applied magnetic field and plots of the peak temperatures versus the applied field	85
5.8.	AC measurements (in-phase magnetic moment, μ') on different nitinol nanoparticles from 10 K to 300 K.	88
5.9.	LASiS liquid dependent high resolution temperature scans of μ'	89
5.10.	Real part of the magnetic moment of NiTi nanoparticles produced in different liquids	92
5.11.	AC measurements (out-of-phase magnetic moment, μ'') on different nitinol nanoparticles from 10 K to 300 K.	94
5.12.	LASiS liquid dependent high resolution temperature scans of μ''	95
5.13.	Imaginary part of the magnetic moment of NiTi nanoparticles produced in different liquids	96
5.14.	Ni hysteresis measurement showing exchange bias	98
6.1.	Hysteresis measurements on Fe nanoparticles produced at different laser powers and coercivity respectively remanence in dependence of laser power.	102
6.2.	Normalized ZFC-FC measurements of Fe nanoparticles produced with different laser powers and a plot of ZFC peak temperatures versus the applied field.	104

List of Tables

2.1.	Comparison of different magnetic nanoparticles production methods	28
4.1.	Comparison of particle size distribution values obtained by means of TEM and fitting	54
5.1.	Coercivity and shift of the LASiS liquid dependent NiTi hysteresis curves	80
5.2.	Fitting results of the ZFC-FC curves of the NiTi nanoparticles . .	82
5.3.	Comparison of the fitted linear curve coefficients of determination from figure 5.7c and figure 5.7d	86
5.4.	T_{\max} and \bar{X} of LASiS liquid dependent μ' measurements	90
5.5.	Averaged fitting parameter $\bar{\alpha}_d$ for each LASiS liquid used	91
5.6.	Coercivity and exchange bias induced shift of Ni nanoparticles . .	97
6.1.	Coefficient of determination and number of datapoints used to obtain R^2 for Fe nanoparticles created at different laser powers . .	104
D.1.	Overview of the <i>Mathematica</i> code line – equation relations in the JA model	163

A. Statutory declaration

I hereby declare in accordance with the examination regulations that I myself have written this master's thesis, that no other sources as those indicated were used and all direct and indirect citations are properly designated, that the thesis handed in was neither fully nor partly subject to another examination procedure or published and that the content of the electronic exemplar is identical to the printing copy.

Rommelshausen, 9th April 2015

UDO HÖFEL

B. Superparamagnetism model related Mathematica code

The code of the following *Mathematica* notebook  allows the fitting of superparamagnetic hysteresis data via the simple LANGEVIN function, confer equation (4.1), the extended LANGEVIN function with a scaling factor, see equation (4.6), and the theoretical straightforward extended LANGEVIN equation mentioned in section 4.1.2.

B.1. Initialisation and Formulæ

In line 5 to line 9 the values that are used as start values for the fits thereafter are defined. Then the temperature is set in line 10. The experimental data is imported and formatted in lines 12 and 13. Be aware that these lines may need to be adjusted, depending on the format of the datafile.

The particle size distribution is defined in line 15, the extended LANGEVIN function *with* a scaling factor in line 17, *without* a scaling factor in line 19 and the simple LANGEVIN function in line 21.

```
1  kB = QuantityMagnitude@UnitConvert[
      Quantity["BoltzmannConstant"]];
2  μ0 = N[4*π*10^-7];
3  μB = QuantityMagnitude@UnitConvert[
      Quantity["BohrMagneton"]];

5  Ntstartvalue = N[0.7*10^15];
6  Msstartvalue = N[1];
7  d0pstartvalueInNanometer = 3.1;
8  d0pstartvalue = d0pstartvalueInNanometer
      *10^-9 kB^(-1/3);
```

```

9 widthdistributionstartvalue = N[0.34];
10 Temperaturevalue = 3;

12 dataInput = Import["C:/Data.dat", "Table"];
13 data = dataInput[[All, {3, 19}]]

15 pdf[dp_?NumericQ, d0p_?NumericQ,
    w_?NumericQ] = kB^(-1/3)/(w*Sqrt[2*Pi])
    *1/dp*E^(-1/(2*w^2)*(Log[dp/Abs[d0p]])^2);

17 mt[b_?NumericQ, Nt_?NumericQ, Ms_?NumericQ,
    d0p_?NumericQ, w_?NumericQ,
    Temp_?NumericQ] := Nt*kB^(4/3)*Ms*Pi/6
    *NIntegrate[dp^3*(Piecewise[{{#/3, Abs[#]
    < 10^-5}, {Coth[#] - 1/(#), True}}] &@(b
    *Ms*Pi*dp^3/(6*Temp)))*pdf[dp, d0p, w],
    {dp, 0, 150}];

19 mt2[b_?NumericQ, Ms_?NumericQ,
    d0p_?NumericQ, w_?NumericQ,
    Temp_?NumericQ] := kB^(1/3)*Ms
    *3*6.59*10^-6/(6*μB*4*(0.5*Abs[d0p])^3
    *6.02214078*10^23)*NIntegrate[dp^3
    *(Piecewise[{{#/3, Abs[#] < 10^-5},
    {Coth[#] - 1/(#), True}}] &@(b
    *Ms*Pi*dp^3/(6*Temp)))*pdf[dp, d0p, w],
    {dp, 0, 150}];

21 Langevin[Msat_, a_, b_] := Abs[Msat]
    *Piecewise[{{#/3, Abs[#] < 10^-5},
    {Coth[#] - 1/(#), True}}] &@(b/a);

```

B.2. Fitting routines

The three blocks for the three different fitting functions are basically identical, thus only the first block is explained in detail. In line 23 the simple LANGEVIN fit is executed, while the following lines 24 to 26 calculate the best fit parameters and the (adjusted) R^2 . For further usage the data is exported in line 27. Note that the values in this line need to be adjusted to the fit results. Finally the results are plotted in line 28.

The code block from line 30 to line 35 (extended LANGEVIN fit with scaling factor) and the next from line 37 to line 42 (extended LANGEVIN fit without scaling factor) possess the same structure as the block described above.

```

23  NLMFitLangevin = NonlinearModelFit[data,
      {Langevin[Msat, a, b]}, {{Msat, 1}, {a,
      1}}, b, MaxIterations -> 100];
      //AbsoluteTiming
24  NLMFitLangevin["BestFitParameters"]
25  NLMFitLangevin["AdjustedRSquared"]
26  NLMFitLangevin["RSquared"]
27  Export["Data1.dat", Table[{b,
      Langevin[Msat, a, b]}, {b, -6, 6, 0.05}]];
28  Show[ListPlot[data], Plot[
      NLMFitLangevin["Function"][x], {x, -20,
      20}]]

30  NLMFit = NonlinearModelFit[data,
      {mt[0.0001*b, Nt, Ms, dOp, w,
      Temperaturevalue]}, {{Nt, Ntstartvalue},
      {Ms, Msstartvalue}, {dOp, dOpstartvalue},
      {w, widthdistributionstartvalue}}, b,
      MaxIterations -> 100]; //AbsoluteTiming
31  NLMFit["BestFitParameters"]
32  NLMFit["AdjustedRSquared"]
33  NLMFit["RSquared"]
34  Export["Data2.dat", Table[{b, mt[0.0001*b,
      ResultOfNt, ResultOfMs, ResultOfdOp,
      ResultOfw, Temperaturevalue]}, {b, -6, 6,

```

```
0.05}}];  
35 Show[ListPlot[data], Plot[  
    NLMFit["Function"][x], {x, -10, 10}]]  
  
37 NLMFit = NonlinearModelFit[data, {mt2[b,  
    Ms, d0p, w, Temperaturevalue]}, {{Ms,  
    109853}, {d0p, 0.12}, {w, 0.34}}, b,  
    MaxIterations -> 10]; //AbsoluteTiming  
38 NLMFit["BestFitParameters"]  
39 NLMFit["AdjustedRSquared"]  
40 NLMFit["RSquared"]  
41 Export["Data3.dat", Table[{b, mt2[0.0001*b,  
    ResultOfMs, ResultOfd0p, ResultOfw,  
    Temperaturevalue]}, {b, -6, 6, 0.05}]];  
42 Show[ListPlot[data], Plot[  
    NLMFit["Function"][x], {x, -10, 10}]]
```

C. Stoner-Wohlfarth *Mathematica* code

C.1. Simulation of Stoner-Wohlfarth hystereses

The code of the following *Mathematica* notebook  allows the calculation of the magnetic moment vector projection on the field direction as a function of the applied field.

C.1.1. Initialisation

In the code shown in this subsection the initial values are entered by the user. `Ps` is the saturation polarisation of the considered particle. `Hmax` is the maximum applied field in Tesla. If the cgs system is preferred one has to change the `KeffSI` and `MsatSI` in line 29 to `KeffCGS` respectively `MsatCGS`. `kB` and `μB` represent the BOLTZMANN constant respectively the BOHR magneton. `numberofsteps` sets the amount of steps that are calculated between 0 and `Hmax`. `startvalue` and `endvalue` are used to restrict the allowed angles between the easy axis of the SW particles and the external applied field. Due to symmetry considerations it is possible to limit the angular range between 0° and 90°. Notice that `startvalue` should be chosen *smaller* than `endvalue`. The `stepsize` sets the stepsize that is used to get from `startvalue` to `endvalue`. Log-normal particle size distributions are accounted by `μ` and `σ`, corresponding to μ^{LN} and σ^{LN} in equation (5.1). `Temperature` accounts for the temperature T at which the hysteresis is calculated. The effective anisotropy `KeffSI` in SI units is entered in line 13. Do note the formula in line 16, that is moved forward from appendix C.1.2 as it should be available to set the minimum in line 18. The discretization of the size distribution is taken into account by lines 18 to 20, that allow to »cut« the ends of the particle size distribution and specify the discrete stepsize that the program uses. Thus it is possible to exclude nanoparticles that are either too small or too large

to contribute to the STONER-WOHLFARTH single domain ferromagnetism. The `latticeconstant`, also called λ_{lat} , should contain the lattice constant of the considered material. `μSaturationPerAtom` allows the specification of the saturation magnetic moment per atom. In combination with the boolean values that determine if the structure of the nanoparticles is either body centered cubic (bcc) or face centered cubic (fcc) (confer lines 24 and 25) it is possible to calculate the `VolumePerAtom`, as can be seen in line 26. Consequently the saturation magnetization `MsatSI` in SI units is calculated in line 27. `Hk` is the anisotropy field. `θcrossover` (also denoted θ_{co}) stands for the angle, above which the ascending branch of the simulated hysteresis increases to a value *larger* than the descending branch (confer section 4.2.1). The value of `ExportToThisPath` in line 33 should contain a string with the absolute path to the to be generated data file. Finally the two tables that will afterwards contain the values of the ascending respectively the descending branch are initialised in the lines 35 and 36. Keep in mind that the values shown are exemplary values. If the particle size distribution should be omitted, enter identical values for `diameterstartvalue` and `diameterendvalue`. Accordingly, if only one angle between the easy axis and the external field is of interest, choose the same values for `startvalue` and `endvalue`.

```

1  Ps = 1. (*The actual value here doesn't matter, as
      we only need dw==0 and not w==0, such that a sole
      prefactor cancels out*);
2  Hmax = 0.15;
3  kB = QuantityMagnitude@UnitConvert[
      Quantity["BoltzmannConstant"]];
4  μB = QuantityMagnitude@UnitConvert[
      Quantity["BohrMagneton"]];
5  numberofsteps = 100.;
6  startvalue = 45.;
7  endvalue = 45.;
8  stepsize = 5.;
9  μ = 1.6;
10 σ = 1.0;

12 Temperature = 2.;
13 KeffSI = 3.7*10^5.;

```

```

14 KeffCGS = 10.*KeffSI;

16 dspm[TemperatureInput_, KeffSIInput_] :=
    2.*Surd[(6.*kB*TemperatureInput)
    /KeffSIInput, 3];

18 diameterstartvalue = 5.*dspm[Temperature,
    KeffSI]*10^9;
19 diameterendvalue = 5.*dspm[Temperature,
    KeffSI]*10^9;
20 diameterstepsize = 0.125*dspm[Temperature,
    KeffSI]*10^9;

22 latticeconstant = 0.25*10.^-9.;
23 μSaturationPerAtom = 2.59*μB;
24 FccStructure = True;
25 BccStructure = False;
26 VolumePerAtom = Piecewise[{{1./4.,
    FccStructure == True}, {1./2.,
    BccStructure == True}}]
    *latticeconstant^3.;
27 MsatSI = μSaturationPerAtom/VolumePerAtom;
28 MsatCGS = MsatSI/10.^3.;
29 Hk = (2.*KeffSI)/MsatSI;

31 θcrossover = N[1/2 ArcCos[-2/Sqrt[5]]];

33 ExportToThisPath = "D:TestExport.dat";

35 hgesn = Table[0, {i, numberofsteps}, {j,
    2}];
36 hgesp = Table[0, {i, numberofsteps}, {j,
    2}];

```

C.1.2. Required Formulæ

This subsection contains the formulas needed for the calculation of the SW model hystereses. The `Clear` command in line 38 is a »safeguard« that, upon subsequent runs, possible changes of one of the following lines are obeyed. Furthermore the magnetocrystalline energy density W_{mc} , in line 39 denoted as `wk`, is calculated. The magnetostatic energy density W_{ms} is given by `wm` in line 40. Both energy densities are summed up in the total energy density W_{SW}^{ges} , respectively `w` in line 41. If additional terms contributing to the total energy density should be taken into account it is necessary to add them to `w`. `dw` in line 42 calculates the first derivative of `w` with respect to θ . `gfunc` contains the angular dependence of the (uncorrected) critical field. The long formula for `HcNoAngularDependency` is necessary to include temperature, anisotropy constant and diameter dependencies for the critical field. Consequently combines `Hc` the angular dependency given by `gfunc` for angles smaller than the crossover angle θ_{co} and a corrected angular dependency formula above the crossover angle with the angular independent `HcNoAngularDependency`. `θs`, see also equation (4.16), is needed afterwards to choose the physically meaningful solutions. Due to the discretized steps that have to be taken between `startvalue` and `endvalue` it is necessary to weigh each step with an area corresponding to the area the easy axis (plus/minus the deviations caused by the discretization) coats on a sphere after rotating completely around the externally applied field. This area is calculated in line 50, in `AreaSpinsOneStep`. Hence the area of one step has to be normalized with the total relevant area on the sphere, called `AreaSpinsTotal`, what is done in `EasyAxisDistribution`. Do note that, if the spins cannot be assumed to show an isotropic distribution, it is easily possible to add, exempli gratia, an angular dependent gaussian to modify this behaviour. Lastly `Magnetization` returns the magnetisation value calculated from the angle θ that minimizes the total energy density.

```

38 Clear[wk, wm, w, dw];
39 wk[θ_] := (KeffSI*Ps*Sin[θ]^2)/MsatSI;
40 wm[H_, θ_, ψ_] := -Ps*H*Cos[ψ - θ];
41 w[H_, θ_, ψ_] := wk[θ] + wm[H, θ, ψ];
42 dw[H_, θ_, ψ_] := D[w[H, θ, ψ], θ];
43 gfunc[ψ_] := (Sin[ψ]^(2./3.) +
               Cos[ψ]^(2./3.))^(−3./2.);

```

```

45 HcNoAngularDependency[TemperatureInput_,
    KeffSIInput_, diameter_] := Piecewise[
    {{1/2*Hk (1 - (dspm[TemperatureInput,
    KeffSIInput]/diameter)^(3./2.)), diameter
    >= dspm[TemperatureInput, KeffSIInput]},
    {0, diameter < dspm[TemperatureInput,
    KeffSIInput]}}];
46 Hc[ψ_, TemperatureInput_, KeffSIInput_,
    diameter_] := Piecewise[
    {{HcNoAngularDependency[TemperatureInput,
    KeffSIInput, diameter]*gfunc[ψ],
    ψ < θcrossover},
    {-HcNoAngularDependency[TemperatureInput,
    KeffSIInput, diameter]
    *Cos[2.*ψ]/Sqrt[2.], ψ > θcrossover}}];
48 θs[ψ_] := N[Pi] - ArcTan[(Tan[ψ])^(1./3.)];
50 AreaSpinsOneStep[α_, stepsizeInput_] :=
    N[Piecewise[{{N[Pi] (2. (Cos[α] - Cos[α
    + (stepsizeInput N[Pi])/(2.*180.))), k
    == startvalue}, {N[Pi] (2. (Cos[α -
    (stepsizeInput N[Pi])/(2.*180.)] - Cos[α
    + (stepsizeInput N[Pi])/(2.*180.))),
    startvalue < k < endvalue}, {N[Pi] (2. (
    Cos[α - (stepsizeInput N[Pi])/(2.*180.)]
    - Cos[α])), k == endvalue}}]]];
51 AreaSpinsTotal[startvaluevar_,
    endvaluevar_] :=
    AreaSpinsTotal[startvaluevar,
    endvaluevar] = N[Pi] (2.
    (-Cos[(endvaluevar N[Pi])/180.] +
    Cos[(startvaluevar N[Pi])/180.]));
53 EasyAxisDistribution[ψvaluevar_,
    stepsizeInput_, startvaluevar_,
    endvaluevar_] :=

```

```

AreaSpinsOneStep[ $\psi$ valuevar,
stepsizeInput]/AreaSpinsTotal[startvaluevar,
endvaluevar];

55 Magnetization[startvaluevar_, endvaluevar_,
ResultOfSolveFor $\theta$ _,  $\psi$ valuevar_,
stepsizeInput_] := Cos[ResultOfSolveFor $\theta$ 
-  $\psi$ valuevar]*EasyAxisDistribution[
 $\psi$ valuevar, stepsizeInput, startvaluevar,
endvaluevar];

```

C.1.3. Loops and calculations

The major loop starting in line 57 sequentially calculates the curves for each given diameter. To allow the calculation of size (and, as the size dependency is found in the same equations as the temperature dependency, see equations (4.18) and (4.19), temperature) independent hysteresis loops there is an IF statement in line 58 that checks if `diameterstartvalue` is identical to `diameterendvalue` – if yes, the influence of the particle size distribution is completely suppressed, thus redefining `Hc` in line 60. Thereafter some basic table initialisations are done in the lines 62 to 65, followed by an IF check if `startvalue` contains an identical value to `endvalue` – if yes, the simulation calculates the hysteresis for a *single* SW particle with *one* angle between the easy axis and the applied field. `ψ valuevar` represents θ in rad. `StepsToHc` calculates how many of the steps possess an applied field smaller than the critical field. `hmp` respectively `hmn` store the values for the upper respectively lower branch of the hysteresis. In line 77 the resulting angle from the energy density minimization problem of the upper hysteresis branch is calculated for each applied field value, subsequently resulting in the corresponding magnetisation. The same for the lower branch can be found in line 82. Line 74 contains a »safeguard« to prevent, if the case occurs, a larger `StepsToHc` than `Hmax`.

If the considered nanoparticles are assumed to be *monodisperse*, but have different θ , such that `startvalue` < `endvalue`, line 89 to line 108 are relevant. The main difference to the single-angle loop is the additional loop over the considered angles, confer lines 90 and 108. In the lines 106 and 107 are the subsequent results of

each angle subsummed. Normalization of the two loops containing the calculation of size independent, single respectively multi angle hystereses is done in line 110 to line 116.

In line 118 starts the part containing the calculations necessary to obtain size dependent results. A initialisation only needed once is consequently done in an IF statement, see Line 119 to line 121, while the initialisations done subsequently in lines 123 and 124 are executed for *every* diameter.

From line 126 to line 145 is the calculation of the magnetisation of particles with a given size distribution, but only *one* angle θ located. The most noteworthy difference to the size independent, single angle loop described above is found in line 128 – StepsToHc respectively Hc are chosen so that size, temperature and the anisotropy constant are taken into account.

As can be seen in line 146 to line 163 is the main difference to the size independent, multi angle loop again found in the usage of Hc incorporating the size dependency.

To rescale the calculated data are lines 165 and 166 necessary. As the isotropic distribution of the considered spins has to be taken into account, lines 168 and 170 weigh each hysteresis branch according to the area the corresponding discretized, rotated angle θ occupies on the upper hemisphere. At the end of the last diameter loop the results are normalised in line 172 to line 181. Note that there are additional checks to prevent a normalisation if diameterstartvalue equals diameterendvalue. This is intended to increase reliability if the program gets modified. The compilation time is shown by the //AbsoluteTiming command in line 183

Finally the data is formatted to be *export ready* in line 185 and actually exported in line 186. Plotting is done in line 188.

```

57 Do[
58   If[diameterstartvalue == diameterendvalue,
      {
60    Hc[ψ_] := Piecewise[{{Hk gfunc[ψ],
                          ψ < θcrossover}, {-Hk Cos[2. ψ]
                          /Sqrt[2.], ψ > θcrossover}}];
62    hgespPartSize = Table[0, {i,
                              numberofsteps}, {j, 2}];

```

```

63   hgesnPartSize = Table[0, {i,
        numberofsteps}, {j, 2}];
64   hgesn = Table[0, {i, numberofsteps}, {j,
        2}];
65   hgesp = Table[0, {i, numberofsteps}, {j,
        2}];

67   If[startvalue == endvalue, {

69      $\psi$ valuevar = startvalue/180.0*N[Pi];
70     StepsToHc = Range[0, Hc[ $\psi$ valuevar],
        Hmax/numberofsteps];

72     hmp = Table[0, {i, numberofsteps}, {j,
        2}];
73     hmn = Table[0, {i, numberofsteps}, {j,
        2}];
74     If[numberofsteps < Length[StepsToHc],
        StepsToHc = hmp];

76     Do[hmp[[i, 1]] = (i - 1.)
        *Hmax/numberofsteps, {i,
        numberofsteps}];
77     hmp[[All, 2]] = Map[Flatten[FindRoot[
        dw[#,  $\theta$ ,  $\psi$ valuevar] == 0., { $\theta$ ,
        N[Pi/4.], 0, N[Pi/2.]}] /. Rule ->
        (#2 &)] &, hmp[[All, 1]]];
78     hmp = Partition[Flatten[hmp], 2];
79     hmp[[All, 2]] = Cos[hmp[[All, 2]] -
         $\psi$ valuevar];

81     Do[hmn[[i, 1]] = (i - 1.)
        *Hmax/(numberofsteps), {i,
        numberofsteps}];
82     hmn[[1;;(Length[StepsToHc] - 1), 2]] =
        Map[Flatten[FindRoot[dw[#,  $\theta$ ,
         $\psi$ valuevar] == 0., { $\theta$ , N[ $\theta$ s[ $\psi$ valuevar]

```

```

+ (Pi -  $\theta$ s[ $\psi$ valuevar])/2.],
 $\theta$ s[ $\psi$ valuevar], Pi}} /.Rule -> (#2 &)]
&, hmn[[1;;(Length[StepsToHc] - 1),
1]]];
83 hmn = Partition[Flatten[hmn], 2];
84 hmn[[ (Length[StepsToHc];;Length[hmn]),
2]] = hmp[[ (Length[StepsToHc]
;;Length[hmn]), 2]];
85 hmn[[1;;(Length[StepsToHc] - 1), 2]] =
Cos[hmn[[1;;(Length[StepsToHc]
- 1), 2]] -  $\psi$ valuevar];

87 hgesn = hmn;
88 hgesp = hmp;},
89 If[startvalue < endvalue, {
90 Do[ $\psi$ valuevar = k/180.0*N[Pi];
91 StepsToHc = Range[0, Hc[ $\psi$ valuevar],
Hmax/numberofsteps];
92 hmp = Table[0, {i, numberofsteps}, {j,
2}];
93 hmn = Table[0, {i, numberofsteps}, {j,
2}];
94 If[numberofsteps < Length[StepsToHc],
StepsToHc = hmp];

96 Do[hmp[[i, 1]] = (i - 1.)
*Hmax/numberofsteps, {i,
numberofsteps}];
97 hmp[[All, 2]] = Map[Flatten[FindRoot[
dw[#,  $\theta$ ,  $\psi$ valuevar] == 0., { $\theta$ ,
N[Pi/4.], 0, N[Pi/2.]}] /. Rule ->
(#2 &)] &, hmp[[All, 1]]];
98 hmp = Partition[Flatten[hmp], 2];
99 hmp[[All, 2]] = Magnetization[
startvalue, endvalue, hmp[[All, 2]],
 $\psi$ valuevar, stepsize];

```

```

101 Do[hmn[[i, 1]] = (i - 1.)
      *Hmax/(numberofsteps), {i,
      numberofsteps}];
102 hmn[[1;;(Length[StepsToHc] - 1), 2]] =
      Map[Flatten[FindRoot[dw[#,  $\theta$ ,
       $\psi$ valuevar] == 0., { $\theta$ ,
      N[ $\theta$ s[ $\psi$ valuevar] + (Pi -
       $\theta$ s[ $\psi$ valuevar])/2.],  $\theta$ s[ $\psi$ valuevar],
      Pi}} /.Rule -> (#2 &)] &,
      hmn[[1;;(Length[StepsToHc] - 1),
      1]]];
103 hmn = Partition[Flatten[hmn], 2];
104 hmn[[ (Length[StepsToHc];;Length[hmn]),
      2]] = hmp[[ (Length[StepsToHc]
      ;;Length[hmn]), 2]];
105 hmn[[1;;(Length[StepsToHc] - 1), 2]] =
      Magnetization[startvalue, endvalue,
      hmn[[1;;(Length[StepsToHc] - 1),
      2]],  $\psi$ valuevar, stepsize];
106 hgesn = hgesn + hmn;
107 hgesp = hgesp + hmp;
108 , {k, startvalue, endvalue,
      stepsize}}]]];

110 hgesn[[All, 1]] = hgesn[[All, 1]]
      *stepsize/(endvalue - startvalue +
      stepsize);
111 hgesp[[All, 1]] = hgesp[[All, 1]]
      *stepsize/(endvalue - startvalue +
      stepsize);
112 hgespPartSize[[All, 1]] = hgesp[[All, 1]];
113 hgesnPartSize[[All, 1]] = hgesn[[All, 1]];
114 ResultHgesp = hgesp~Extract~Position[#,
      Max@#] &@hgesp[[All, 2]];
115 hgespPartSize[[All, 2]] = hgesp[[All,
      2]]/ResultHgesp[[1, 2]];
116 hgesnPartSize[[All, 2]] = hgesn[[All,

```

```

2]]/Resulthgesp[[1, 2]];

118 }, {
119 If[ $\eta$  == diameterstartvalue, {
120   hgespPartSize = Table[0, {i,
121     numberofsteps}, {j, 2}];
122   hgesnPartSize = Table[0, {i,
123     numberofsteps}, {j, 2}];];];

123 hgesn = Table[0, {i, numberofsteps}, {j,
124   2}];
125 hgesp = Table[0, {i, numberofsteps}, {j,
126   2}];

126 If[startvalue == endvalue,
127   { $\psi$ valuevar = startvalue/180.0*N[Pi];
128   StepsToHc = Range[0, Hc[ $\psi$ valuevar,
129     Temperature, KeffSI, 10-9  $\eta$ ],
130     Hmax/numberofsteps];

130 hmp = Table[0, {i, numberofsteps}, {j,
131   2}];
132 hmn = Table[0, {i, numberofsteps}, {j,
133   2}];

133 Do[hmp[[i, 1]] = (i - 1.)
134   *Hmax/numberofsteps, {i,
135     numberofsteps}];
136 hmp[[All, 2]] = Map[Flatten[FindRoot[
137   dw[#,  $\theta$ ,  $\psi$ valuevar] == 0., { $\theta$ ,
138     N[Pi/4.], 0, N[Pi/2.]}] /. Rule ->
139     (#2 &)] &, hmp[[All, 1]]];
140 hmp = Partition[Flatten[hmp], 2];
141 hmp[[All, 2]] = Cos[hmp[[All, 2]] -
142    $\psi$ valuevar];

142 Do[hmn[[i, 1]] = (i - 1.)

```

```

      *Hmax/(numberofsteps), {i,
      numberofsteps}];
139   hmn[[1;;(Length[StepsToHc] - 1), 2]] =
      Map[Flatten[FindRoot[dw[#,  $\theta$ ,
       $\psi$ valuevar] == 0., { $\theta$ , N[ $\theta$ s[ $\psi$ valuevar]
      + (Pi -  $\theta$ s[ $\psi$ valuevar])/2.],
       $\theta$ s[ $\psi$ valuevar], Pi]} /.Rule -> (#2 &)]
      &, hmn[[1;;(Length[StepsToHc] - 1),
      1]]];
140   hmn = Partition[Flatten[hmn], 2];
141   hmn[[ (Length[StepsToHc];;Length[hmn]),
      2]] = hmp[[ (Length[StepsToHc]
      ;;Length[hmn]), 2]];
142   hmn[[1;;(Length[StepsToHc] - 1), 2]] =
      Cos[hmn[[1;;(Length[StepsToHc] - 1),
      2]] -  $\psi$ valuevar];

144   hgesn = hgesn + hmn;
145   hgesp = hgesp + hmp;},
146   If[startvalue < endvalue, {
147     Do[ $\psi$ valuevar = k/180.0*N[Pi];
148     StepsToHc = Range[0, Hc[ $\psi$ valuevar,
      Temperature, KeffSI, 10-9  $\eta$ ],
      Hmax/numberofsteps];
149     hmp = Table[0, {i, numberofsteps}, {j,
      2}];
150     hmn = Table[0, {i, numberofsteps}, {j,
      2}];
151     Do[hmp[[i, 1]] = (i - 1.)
      *Hmax/numberofsteps, {i,
      numberofsteps}];
152     hmp[[All, 2]] = Map[Flatten[FindRoot[
      dw[#,  $\theta$ ,  $\psi$ valuevar] == 0., { $\theta$ ,
      N[Pi/4.], 0, N[Pi/2.]}] /.Rule ->
      (#2 &)] &, hmp[[All, 1]]];
153     hmp = Partition[Flatten[hmp], 2];
154     hmp[[All, 2]] = Magnetization[

```

```

startvalue, endvalue, hmp[[All, 2]],
ψvaluevar, stepsize];

156 Do[hmn[[i, 1]] = (i - 1.)
      *Hmax/(numberofsteps), {i,
      numberofsteps}];
157 hmn[[1;;(Length[StepsToHc] - 1), 2]] =
      Map[Flatten[FindRoot[dw[#, θ,
      ψvaluevar] == 0., {θ,
      N[θs[ψvaluevar] + (Pi -
      θs[ψvaluevar])/2.], θs[ψvaluevar],
      Pi]} /.Rule -> (#2 &)] &,
      hmn[[1;;(Length[StepsToHc] - 1),
      1]]];
158 hmn = Partition[Flatten[hmn], 2];
159 hmn[[ (Length[StepsToHc] ;; Length[hmn]),
      2]] = hmp[[ (Length[StepsToHc]
      ;; Length[hmn]), 2]];
160 hmn[[1;;(Length[StepsToHc] - 1), 2]] =
      Magnetization[startvalue, endvalue,
      hmn[[1;;(Length[StepsToHc] - 1),
      2]], ψvaluevar, stepsize];
161 hgesn = hgesn + hmn;
162 hgesp = hgesp + hmp;
163 , {k, startvalue, endvalue,
      stepsize}}]]];

165 hgesn[[All, 1]] = hgesn[[All, 1]]
      *stepsize/(endvalue - startvalue +
      stepsize);
166 hgesp[[All, 1]] = hgesp[[All, 1]]
      *stepsize/(endvalue - startvalue +
      stepsize);

168 hgespPartSize[[All, 2]] =
      hgespPartSize[[All, 2]] + hgesp[[All,
      2]]*Piecewise[{{NIntegrate[PDF[

```

```

LogNormalDistribution[ $\mu$ ,  $\sigma$ ], x], {x,
diameterstartvalue, diameterstartvalue
+ 0.5 diameterstepsize}],  $\eta$  ==
diameterstartvalue}, {NIntegrate[PDF[
LogNormalDistribution[ $\mu$ ,  $\sigma$ ], x], {x,  $\eta$ 
- 0.5 diameterstepsize,  $\eta$  + 0.5
diameterstepsize}], (diameterendvalue -
diameterstepsize) >  $\eta$  >
diameterstartvalue}, {NIntegrate[
PDF[LogNormalDistribution[ $\mu$ ,  $\sigma$ ], x],
{x,  $\eta$  - 0.5 diameterstepsize,
diameterendvalue}],  $\eta$  >
(diameterendvalue -
diameterstepsize)}}];

170 hgesnPartSize[[All, 2]] =
hgesnPartSize[[All, 2]] + hgesn[[All,
2]]* Piecewise[{{NIntegrate[PDF[
LogNormalDistribution[ $\mu$ ,  $\sigma$ ], x], {x,
diameterstartvalue, diameterstartvalue
+ 0.5 diameterstepsize}],  $\eta$  ==
diameterstartvalue}, {NIntegrate[PDF[
LogNormalDistribution[ $\mu$ ,  $\sigma$ ], x], {x,  $\eta$ 
- 0.5 diameterstepsize,  $\eta$  + 0.5
diameterstepsize}], (diameterendvalue -
diameterstepsize) >  $\eta$  >
diameterstartvalue}, {NIntegrate[
PDF[LogNormalDistribution[ $\mu$ ,  $\sigma$ ], x],
{x,  $\eta$  - 0.5 diameterstepsize,
diameterendvalue}],  $\eta$  >
(diameterendvalue -
diameterstepsize)}}];

172 If[ $\eta$  > (diameterendvalue -
diameterstepsize), {
173 hgespPartSize[[All, 2]] =
hgespPartSize[[All, 2]]/Piecewise[

```

```

    {{NIntegrate[PDF[
    LogNormalDistribution[ $\mu$ ,  $\sigma$ ], x], {x,
    diameterstartvalue,
    diameterendvalue}], diameterstartvalue
    < diameterendvalue}, {1,
    diameterstartvalue ==
    diameterendvalue}}];
174 hgespPartSize[[All, 1]] = hgesp[[All,
    1]];
175 hgesnPartSize[[All, 2]] =
    hgesnPartSize[[All, 2]]/Piecewise[
    {{NIntegrate[PDF[
    LogNormalDistribution[ $\mu$ ,  $\sigma$ ], x], {x,
    diameterstartvalue,
    diameterendvalue}], diameterstartvalue
    < diameterendvalue}, {1,
    diameterstartvalue ==
    diameterendvalue}}];
176 hgesnPartSize[[All, 1]] = hgesn[[All,
    1]];

178 ResultHgesp =
    hgespPartSize~Extract~Position[#,
    Max@#] &@hgespPartSize[[All, 2]];
179 hgespPartSize[[All, 2]] =
    hgespPartSize[[All, 2]]
    /ResultHgesp[[1, 2]];
180 hgesnPartSize[[All, 2]] =
    hgesnPartSize[[All, 2]]
    /ResultHgesp[[1, 2]];
181 }]]]

183 , { $\eta$ , diameterstartvalue,
    diameterendvalue, diameterstepsize}];
    //AbsoluteTiming

185 ExportReadyData = Partition[Flatten[

```

```

Append[Append[Append[hgesnPartSize,
Reverse[hgespPartSize]], -hgesnPartSize],
-Reverse[hgespPartSize]], 2];
186 Export[ExportToThisPath, ExportReadyData];

188 ListPlot[{hgesnPartSize, -hgesnPartSize,
hgespPartSize, -hgespPartSize}, Joined ->
True, PlotRange -> {{-Hmax, Hmax}, {-1.1,
1.1}}, ImageSize -> Large, Frame -> True,
FrameLabel -> {"applied field H",
"reduced magnetization M/Msat"}, PlotStyle
-> {Blue}, GridLines -> Automatic,
GridLinesStyle -> Directive[Dashed]]

```

C.2. Fit of a Stoner-Wohlfarth hysteresis to experimental data

The code of the following *Mathematica* notebook  provides an interface to fit a STONER-WOHLFARTH hysteresis to experimental data by varying the subset of angles that are allowed. Although the order of the lines is different to the code shown in appendix C.1, only pieces that are sufficiently important are picked out and explained, the rest of the code should be clear if appendix C.1 has been read.

C.2.1. Calculation of the deviation of a simulated hysteresis compared to experimental data

The subsequent code defines the function `SWModel` which calculates the normalized magnetisation at the applied field values given by the experimental data. Note that the checks for $\zeta == 1$ respectively $\zeta == 2$ prevent time loss due to unnecessary calculations. The code in line 36 and line 47 calculates the squared deviation for the upper (line 36) respectively lower (line 47) branch of the simulated hysteresis with respect to the experimental data. The resulting values are exported in line 50 for later use. With the help of the explanations found in appendix C.1 the remaining code of this subsection should be straightforwardly comprehensible.

```

1  SWModel[startvalue_, endvalue_, stepsize_,
   ζ_, CompleteFileLocation_, Temperature_,
   Keff_, η_, diameterstartvalue_,
   diameterendvalue_, diameterstepsize_, μ_,
   σ_] := {

3  Do[
4    ψvaluevar = k/180.0*N[Pi];
5    StepsToHc = LengthWhile[Flatten[Sort[
   dataHvalues]], # < Hc[ψvaluevar,
   Temperature, Keff, η] &];

7    If[ζ == 1, hmp = Table[0., {i,
   numberofsteps}, {j, 2}];
8    If[k == startvalue, hgesp = Table[0,
   {i, numberofsteps}, {j, 2}], Null];
9    If[k == startvalue &&
   η == diameterstartvalue,
   hgespPartSize = Table[0, {i,
   numberofsteps}, {j, 2}], Null];
10   hmp[[All, 1]] = data[[All, 1]];
11   hmp[[All, 2]] = Map[Flatten[FindRoot[
   dw[#, θ, ψvaluevar] == 0.,
   {θ, N[Pi/4.], 0, N[Pi/2.]}]
   /. Rule -> (#2 &)] &, hmp[[All, 1]]];
12   hmp = Partition[Flatten[hmp], 2];
13   hmp[[All, 2]] = Magnetization[
   startvalue, endvalue, hmp[[All, 2]],
   ψvaluevar, stepsize, k];
14   Evaluate[hgesp = hgesp + hmp];];

16   If[ζ == 2,
17     hmn = Table[0., {i, numberofsteps},
   {j, 2}];
18     If[k == startvalue, hgesn = Table[0,
   {i, numberofsteps}, {j, 2}], Null];

```

```

19   If[k == startvalue &&
       $\eta$  == diameterstartvalue,
      hgesnPartSize = Table[0, {i,
        numberofsteps}, {j, 2}], Null];
20   hmn[[All, 1]] = data[[All, 1]];
21   hmn[[1;;(StepsToHc - 1), 2]] =
      Map[Flatten[FindRoot[
        dw[#,  $\theta$ ,  $\psi$ valuevar] == 0.,
        { $\theta$ ,  $\theta$ s[ $\psi$ valuevar] + (N[Pi]
          -  $\theta$ s[ $\psi$ valuevar])/2.,  $\theta$ s[ $\psi$ valuevar],
          N[Pi]}] /. Rule -> (#2 &)] &,
        hmn[[1;;(StepsToHc - 1), 1]]];
22   hmn[(StepsToHc;;Length[hmn]), 2]] =
      Map[Flatten[FindRoot[
        dw[#,  $\theta$ ,  $\psi$ valuevar] == 0.,
        { $\theta$ , N[Pi/4.], 0, N[Pi/2.]}]
        /. Rule -> (#2 &)] &,
        hmn[(StepsToHc;;Length[hmn]), 1]]];
23   hmn = Partition[Flatten[hmn], 2];
24   hmn[[All, 2]] = Magnetization[
      startvalue, endvalue, hmn[[All, 2]],
       $\psi$ valuevar, stepsize, k];
25   Evaluate[hgesn = hgesn + hmn];];

27   If[k > (endvalue - stepsize) &&  $\zeta$  == 1, {
28     hgesp[[All, 1]] = hgesp[[All, 1]]
      *stepsize/(endvalue - startvalue);
29     hgespPartSize[[All, 2]] =
      hgespPartSize[[All, 2]] +
      hgesp[[All, 2]]*Piecewise[{{
        NIntegrate[PDF[
          LogNormalDistribution[ $\mu$ ,  $\sigma$ ], x],
          {x, diameterstartvalue,
            diameterstartvalue +
              0.5*diameterstepsize}},
           $\eta$  == diameterstartvalue}, {
        NIntegrate[PDF[

```

```

LogNormalDistribution[ $\mu$ ,  $\sigma$ ], x],
{x,  $\eta - 0.5 \cdot \text{diameterstepsize}$ ,
 $\eta + 0.5 \cdot \text{diameterstepsize}$ }},
( $\text{diameterendvalue} - \text{diameterstepsize}$ )
>  $\eta$  >  $\text{diameterstartvalue}$ }, {
NIntegrate[PDF[
LogNormalDistribution[ $\mu$ ,  $\sigma$ ], x],
{x,  $\eta - 0.5 \cdot \text{diameterstepsize}$ ,
 $\text{diameterendvalue}$ ]],
 $\eta$  > ( $\text{diameterendvalue}$ 
-  $\text{diameterstepsize}$ )}}];}, Null];

31 If[k > ( $\text{endvalue} - \text{stepsize}$ ) &&  $\zeta == 1$ 
    &&  $\eta$  > ( $\text{diameterendvalue} -$ 
     $\text{diameterstepsize}$ ), {
32 hgespPartSize[[All, 2]] =
    hgespPartSize[[All, 2]]
    /NIntegrate[PDF[
    LogNormalDistribution[ $\mu$ ,  $\sigma$ ], x],
    {x,  $\text{diameterstartvalue}$ ,
     $\text{diameterendvalue}$ ]];
33 hgespPartSize[[All, 1]] =
    hgesp[[All, 1]];
34 ResultHgesp =
    hgespPartSize~Extract~Position[#,
    Max@#] &@ hgespPartSize[[All, 2]];
35 hgespPartSize[[All, 2]] =
    hgespPartSize[[All, 2]]
    /ResultHgesp[[1, 2]];
36 SquaredDeviation = Append[Append[Append[
    Evaluate[Total[(hgespPartSize -
    data)^2.]],  $\text{startvalue}$ ],  $\text{endvalue}$ ],
    hgespPartSize]], Null];

38 If[k > ( $\text{endvalue} - \text{stepsize}$ ) &&  $\zeta == 2$ , {
39 hgesn[[All, 1]] = hgesn[[All, 1]]
    *stepsize/( $\text{endvalue} - \text{startvalue}$ );

```

```

40   hgesnPartSize[[All, 2]] =
      hgesnPartSize[[All, 2]] +
      hgesn[[All, 2]]*Piecewise[{{
      NIntegrate[PDF[
      LogNormalDistribution[ $\mu$ ,  $\sigma$ ], x],
      {x, diameterstartvalue,
      diameterstartvalue +
      0.5*diameterstepsize}},
       $\eta$  == diameterstartvalue}, {
      NIntegrate[PDF[
      LogNormalDistribution[ $\mu$ ,  $\sigma$ ], x],
      {x,  $\eta$  - 0.5 diameterstepsize,
       $\eta$  + 0.5 diameterstepsize}},
      (diameterendvalue - diameterstepsize)
      >  $\eta$  > diameterstartvalue}, {
      NIntegrate[PDF[
      LogNormalDistribution[ $\mu$ ,  $\sigma$ ], x],
      {x,  $\eta$  - 0.5 diameterstepsize,
      diameterendvalue}},
       $\eta$  > (diameterendvalue
      - diameterstepsize)}}];}, Null];

42   If[k > (endvalue - stepsize) &&  $\zeta$  == 2
      &&  $\eta$  > (diameterendvalue -
      diameterstepsize), {
43   hgesnPartSize[[All, 2]] =
      hgesnPartSize[[All, 2]]
      /NIntegrate[PDF[
      LogNormalDistribution[ $\mu$ ,  $\sigma$ ], x],
      {x, diameterstartvalue,
      diameterendvalue}];
44   hgesnPartSize[[All, 1]] =
      hgesn[[All, 1]];
45   ResultHgesn =
      hgesnPartSize~Extract~Position[#,
      Max@#] &@ hgesnPartSize[[All, 2]];
46   hgesnPartSize[[All, 2]] =

```

```

    hgesnPartSize[[All, 2]]
    /Resulthgesn[[1, 2]];
47 SquaredDeviation = Append[Append[Append[
    Evaluate[Re[Total[(hgesnPartSize -
    data)^2.]], startvalue], endvalue],
    hgesnPartSize]], Null];

49 If[k > (endvalue - stepsize)
    && η > (diameterendvalue -
    diameterstepsize),
50 PutAppend[{SquaredDeviation},
    CompleteFileLocation], Null];

52 , {k, startvalue, endvalue, stepsize}]];

```

C.2.2. Final function / interface

This subsection contains a wrapper around the function defined in appendix C.2.1, consequently providing a function that serves as easily configurable interface. Until line 84 the initialisation, id est the calculation of the needed values and the definition of most of the necessary functions is completed. Thereafter, in the lines 85 and 86, files with the same name as the temporary output files get deleted. Be aware that thus no important files should have names identical to the temporary output files!

Subsequently, from line 87 to line 94, the data files containing the experimental data are loaded. They need to be in the format `data1.dat` (values of positive, upper branch) and `data2.dat` (values of positive, lower branch). Due to the inherently symmetric nature of theoretical STONER-WOHLFARTH hystereses the complete negative part is neglected.

Line 95 to line 98 contain the normalisation of the experimental data, M/M_{sat} . It is important to note that the lower branch *must not* contain higher values of M , as otherwise the upper and lower branch get normalised to different values. If the lower branch contains only *smaller* values the program automatically uses the largest value of the upper branch to normalise. As the data has to be in the right order to guarantee a trouble-free modulus operandi, the code in line 99 sorts the data accordingly.

To enable the program to automatically plot the best fit afterwards, the code in line 101 to line 106 saves the maximum values that are important if the plot should scale automatically.

The last two functions that complement the functions defined up to line 84 are implemented in line 108 and line 110.

A loop over the function from appendix C.2.1 iterating over the particle size, the start and end values of the angle subset is used to cover the considered parameter space, confer line 113.

The output that informs the user of the best (least squared) fit and the corresponding calculations can be found in line 115 to line 123, while line 125 finishes the definition of the final function. The next subsection concludes with an exemplary usage of the function defined in this subsection.

```

54 CompleteSWModelLoopFit[minval_,
    maxval_, stepsize_, FinenessOfLoop_,
    DataFileToUse_, FileLocation_,
    TemperatureInput_, KeffInput_,
    diameterstartvalue_, diameterendvalue_,
    diameterstepsize_,  $\mu$ _,  $\sigma$ _,
    latticeconstant_,  $\mu$ SaturationPerAtom_,
    Fcc_, Bcc_] := {

56 Ps = 1.;
57 kB = QuantityMagnitude@UnitConvert[
    Quantity["BoltzmannConstant"]];
58  $\mu$ B = QuantityMagnitude@UnitConvert[
    Quantity["BohrMagneton"]];
59  $\theta$ crossover = N[1/2*ArcCos[-2/Sqrt[5]]];
60 Temperature = TemperatureInput;
61 KeffSI = KeffInput;
62 KeffCGS = 10.*KeffSI;
63 VolumePerAtom = Piecewise[{{1./4.,
    Fcc == True}, {1./2., Bcc == True}}]
    *latticeconstant^3.;
64 MsatSI =  $\mu$ SaturationPerAtom/VolumePerAtom;
65 MsatCGS = MsatSI/10.^3.;

```

```

66   Hk = (2.*KeffSI)/MsatSI;

68   wk[θ_] := (KeffSI*Ps*Sin[θ]^2)/MsatSI;
69   wm[H_, θ_, ψ_] := -Ps*H*Cos[ψ - θ];
70   w[H_, θ_, ψ_] := wk[θ] + wm[H, θ, ψ];
71   dw[H_, θ_, ψ_] := D[w[H, θ, ψ], θ];
72   gfunc[ψ_] := (Sin[ψ]^(2./3.) +
      Cos[ψ]^(2./3.))^(−3./ 2.);
73   dspm[Temp_, Keffective_] :=
      2.*Surd[(6.*kB Temp)/Keffective, 3];
74   θs[ψ_] := N[Pi] - ArcTan[(Tan[ψ])^(1./3.)];

76   AreaSpinsOneStep[α_, stepsizevalue_, k_,
      startvaluevar_, endvaluevar_] :=
      N[Piecewise[{{N[π]*(2.*(Cos[α] - Cos[α +
      (stepsizevalue*N[π])/(2.*180.)))},
      k == startvaluevar}, {N[π]*(2.*(Cos[α -
      (stepsizevalue*N[π])/(2.*180.)] - Cos[α +
      (stepsizevalue*N[π])/(2.*180.)))},
      startvaluevar < k < endvaluevar},
      {N[π]*(2.*(Cos[α - (stepsizevalue*N[π])
      / (2.*180.)] - Cos[α])),
      k == endvaluevar}}]];

78   AreaSpinsTotal[startvaluevar_,
      endvaluevar_] :=
      AreaSpinsTotal[startvaluevar,
      endvaluevar] = N[π] (2.*(-Cos[(
      endvaluevar N[π])/180.] +
      Cos[(startvaluevar N[π])/180.]));

80   EasyAxisDistribution[ψvaluevar_,
      stepsizevalue_, startvaluevar_,
      endvaluevar_, k_] := AreaSpinsOneStep[
      ψvaluevar, stepsizevalue, k,
      startvaluevar, endvaluevar]
      /AreaSpinsTotal[startvaluevar,

```

```

    endvaluevar];

82  Magnetization[startvaluevar_,
    endvaluevar_, ResultOfSolveForθ_,
    ψvaluevar_, stepsizevalue_, k_] :=
    Cos[ResultOfSolveForθ - ψvaluevar]
    *EasyAxisDistribution[ψvaluevar,
    stepsizevalue, startvaluevar,
    endvaluevar, k];

84  Do[
85    If[ζ == 1, DeleteFile[FileLocation <>
    ToString[ζ] <> ".dat"]];
86    If[ζ == 2, DeleteFile[FileLocation <>
    ToString[ζ] <> ".dat"]];
87    If[ζ == 1,
88      dataInput = Import[DataFileToUse <>
    ToString[ζ] <> ".dat", "Table",
    "FieldSeparators" -> ", ", Null];
89    If[ζ == 2,
90      dataInput = Import[DataFileToUse <>
    ToString[ζ] <> ".dat", "Table",
    "FieldSeparators" -> ", ", Null];
91    data = dataInput[[All, {1, 2}]];
92    numberofsteps = Length[data];
93    dataHvalues = dataInput[[All, 1]];
94    dataMuvalues = dataInput[[All, 2]];
95    If[ζ == 1,
    NormDataYValue = Max[dataMuvalues]];
96    If[ζ == 2
    && NormDataYValue < Max[dataMuvalues],
97      NormDataYValue = Max[dataMuvalues]];
98    data[[All, 2]] = data[[All, 2]]
    /NormDataYValue;
99    data = Sort[data];

101  If[ζ == 1, {

```

```

102   MaxHvalue1 = Max[dataHvalues];
103   SaveDataForPlot = data;]];

105   If[ $\zeta$  == 2,
106     MaxHvalueForPlot = Piecewise[{{
      MaxHvalue1, MaxHvalue1 >
      Max[dataHvalues]}, {Max[dataHvalues],
      MaxHvalue1 <= Max[dataHvalues]}]];

108   HcNoAngularDependency[TemperatureInput2_,
      Keff_, diameter_] := Piecewise[{{
      1./2.*Hk*(1. - (dspm[TemperatureInput2,
      Keff]/diameter)^(3./2.)),
      diameter > dspm[TemperatureInput2,
      Keff]}, {0., diameter <=
      dspm[TemperatureInput2, Keff]}]];

110   Hc[ $\psi$ _, TemperatureInput2_, Keff_,
      diameter_] := Piecewise[{{
      HcNoAngularDependency[
      TemperatureInput2, Keff, diameter]
      *gfunc[ $\psi$ ],  $\psi$  <  $\theta$ crossover},
      {-HcNoAngularDependency[
      TemperatureInput2, Keff, diameter]
      *Cos[2.* $\psi$ ]/Sqrt[2.],  $\psi$  >  $\theta$ crossover}}]];

112   Do[{
113     SWModel[startvalue, endvalue, stepsize,
       $\zeta$ , FileLocation <> ToString[ $\zeta$ ] <>
      ".dat", TemperatureInput, KeffInput,
       $\eta$ , diameterstartvalue,
      diameterendvalue, diameterstepsize,  $\mu$ ,
       $\sigma$ ], {startvalue, minval, maxval -
      FinenessOfLoop, FinenessOfLoop},
      {endvalue, startvalue +
      FinenessOfLoop, maxval,
      FinenessOfLoop}, { $\eta$ ,

```

```

    diameterstartvalue, diameterendvalue,
    diameterstepsize});

115   If[ $\zeta$  == 2,
116     FirstFile = Flatten[ReadList[
    FileLocation <> ToString[1] <> ".dat",
    Expression], 1];
117     SecondFile = Flatten[ReadList[
    FileLocation <> ToString[2] <> ".dat",
    Expression], 1];
118     Result = Partition[Flatten[(
    FirstFile[[All, 1;;4]] +
    SecondFile[[All, 1;;4]])/2], 4];
119     hgespForPlot = Partition[Flatten[
    FirstFile[[All, 5]]
    ~Extract~Position[#, Min@#]
    &@ Result[[All, 2]]], 2];
120     hgesnForPlot = Partition[Flatten[
    SecondFile[[All, 5]]
    ~Extract~Position[#, Min@#]
    &@ Result[[All, 2]]], 2];
121     EndResult = Result~Extract~Position[#,
    Min@#] &@Result[[All, 2]];
122     Print["The best fit to the data was
    achieved using a starting value of "
    <> ToString[EndResult[[1, 3]]
    <> " and an ending value of "
    <> ToString[EndResult[[1, 4]]
    <> " The anisotropy field has the
    value " <> ToString[Hk]];
123     , Null],
125     { $\zeta$ , 1, 2, 1}]];

```

C.2.3. Exemplary usage

To give a practical example of the usage of the function defined in appendix C.2.2, see line 127. The values are partially taken from [79].

A plot of the result of the code in line 127 is coded in line 129, such that one can get a fast impression of how well the fit actually worked.

```

127 CompleteSWModelLoopFit[0., 90., 2., 10.,
    "D:/Data", "D:/Result", 2., 3.7*10^5, 5.,
    40., 5., 1.6, 1.0, 0.27*10^-9, 2.59 μB,
    True, False] // AbsoluteTiming

129 Show[ListPlot[{data, -data,
    SaveDataForPlot, -SaveDataForPlot},
    Joined -> True, PlotRange -> {{
    -MaxHvalueForPlot, MaxHvalueForPlot},
    {-1.05, 1.05}}, ImageSize -> Large,
    Frame -> True, PlotStyle -> {Red},
    PlotLegends -> Placed[{"Experimental
    data"}, {Left, Top}], FrameLabel ->
    {"applied field \!\(\*StyleBox[\\"H\",
    \nFontSlant->\\"Italic\\"\)}", "reduced
    magnetization \!\(\*StyleBox[\\"M\",
    \nFontSlant->\\"Italic\\"\)}",
    /\!\(\*SubscriptBox[\(M\), \(\text{sat}\)]\)\)},
    GridLines -> Automatic, GridLinesStyle ->
    Directive[Dashed], PlotMarkers ->
    Automatic], ListPlot[{hgespForPlot,
    -hgespForPlot, hgesnForPlot,
    -hgesnForPlot}, Joined -> True, PlotRange
    -> All, PlotStyle -> {{Blue, Dashed}},
    PlotLegends -> Placed[{"Extended Stoner
    Wohlfarth Model fit"}, {Left, Top}],
    PlotMarkers -> Automatic]]

```


D. Jiles-Atherton *Mathematica* code

D.1. Simulation of Jiles-Atherton hystereses

The code of the following *Mathematica* notebook  allows the simulation of a hysteresis according to the extended JILES-ATHERTON-model. The basic idea was taken from [83].

D.1.1. Required Formulæ

In this subsection is the code corresponding to the formulas needed for the calculation of the JA model hystereses shown. The meaning of the formulas is explained in more detail in section 4.3.1. Consequently shows table D.1 an overview of the correspondent equations and the *Mathematica* code.

As a reminder: Line 1 corresponds to the *effective* magnetic field, this is necessary to respect the occurring coupling between different ferromagnetic domains. Subsequently, in line 3 is the LANGEVIN function defined. An approximation is used for small values to avoid possible numerical problems, even though the function is well behaving for small values. Thereafter, in line 5, is the anhysteretic magnetisation defined, that is basically the LANGEVIN function multiplied with the saturation magnetisation. In line 7 is the only equation found, which is needed for the calculation of the hysteresis that is *not* shown in section 4.3.1. It represents the derivation of the LANGEVIN function with respect to the effective magnetic field H_{eff} . The following equations in line 9 and line 11 are needed to obtain physically meaningful

Table D.1.: Overview of the relations between *Mathematica* code lines and their corresponding equations.

line	1	3, 5	7	9	11	13
equation	4.23	4.24	—	4.27	4.26	4.25

curves, as they prevent a decrease in magnetisation with increasing applied field. Finally combines the equation in line 13 every »piece«, such that upon solving this equation the hysteresis loop emerges.

```

1  Heff[t_, M_, Hmax_, α_, ω_] := Hmax
   Sin[ω t] + α M

3  Langevinfct[t_, M_, Hmax_, α_, ω_, a_] :=
   Piecewise[{{(α M + Hmax Sin[ω t])
   /(3. a), Abs[α M + Hmax Sin[ω t]]
   /a < 1./100000.}, {Coth[(α M + Hmax
   Sin[ω t])/a] - a/(α M + Hmax Sin[ω t]),
   True}}]

5  Man[t_, M_, Hmax_, α_, ω_, a_, Ms_] := Ms
   Langevinfct[t, M, Hmax, α, ω, a]

7  DManDHeff[t_, M_, Hmax_, α_, ω_, a_] :=
   a/Heff[t, M, Hmax, α, ω]^2. -
   Csch[Heff[t, M, Hmax, α, ω]/a]^2./a

9  δ[t_, ω_] := Sign[Cos[ω t]]

11 δM[t_, M_, Hmax_, α_, ω_, a_, Ms_] :=
   Piecewise[{{0., (Cos[ω t] < 0. && Man[t,
   M, Hmax, α, ω, a, Ms] - M > 0.) ||
   (Cos[ω t] > 0. && Man[t, M, Hmax, α, ω,
   a, Ms] - M < 0.)}}, {1., True}}]

13 ExtendedJAModelEquation[t_, M_, Hmax_, α_,
   ω_, a_, Ms_, k_, c_, μ0_] := ((k δ[t, ω]
   c DManDHeff[t, M, Hmax, α, ω, a])/μ0 +
   δM[t, M, Hmax, α, ω, a, Ms] (Man[t, M,
   Hmax, α, ω, a, Ms] - M))/((k δ[t, ω])/μ0
   - δM[t, M, Hmax, α, ω, a, Ms] (Man[t, M,
   Hmax, α, ω, a, Ms] - M) α - (k δ[t, ω] c

```

```

 $\alpha$  DManDHeff[t, M, Hmax,  $\alpha$ ,  $\omega$ , a]/ $\mu 0$ 
Hmax  $\omega$  Cos[ $\omega$  t]

```

D.1.2. Implementation of the classical Runge-Kutta fourth-order method

The RUNGE-KUTTA method is one of the standard methods used to approximately solve ordinary differential equations (see exempli gratia [117]). As a consequence RK4 returns the solution of f with the startvalues t_0 and M_0 and step the amount of steps. t_n specifies the endvalue of t .

```

15  RK4[f_, {t_, t0_, tn_}, {M_, M0_}, steps_]
    := Block[{told = t0, Mold = M0, retlist =
      {{t0, M0}}, t, M, h}, h = N[(tn - t0)
      /steps];
16  Do[
17    tnew = told + h;
18    kOne = h*(f /. {t -> told, M -> Mold});
19    kTwo = h*(f /. {t -> told + h/2, M ->
      Mold + kOne/2});
20    kThree = h*(f /. {t -> told + h/2, M ->
      Mold + kTwo/2});
21    kFour = h*(f /. {t -> told + h, M -> Mold
      + kThree});
22    Mnew = Mold + Total[{kOne, 2. kTwo, 2.
      kThree, kFour}]/6. /. {M -> Mold};
23    retlist = Append[retlist, {tnew, Mnew}];
24    told = tnew;
25    Mold = Mnew, {steps}];
26  Return[retlist]

```

D.1.3. Final function and example

Lastly the function ExtendedJAModel is defined. Therein the RUNGE-KUTTA method is used to solve equation (4.25). It is crucial to note that the values of the

applied magnetic field and the values of the flux density are calculated separately, see line 32 and line 33. After that the calculated values are plotted.

```

28 ExtendedJAModel[t_, M_, tstart_, tend_,
   numberofsteps_, Ms_, a_, k_,  $\alpha$ _, c_,
    $\mu$ 0_, Hmax_,  $\omega$ ] := {
29 ExtendedJAModelSolved =
   RK4[ExtendedJAModelEquation[t, M, Hmax,
    $\alpha$ ,  $\omega$ , a, Ms, k, c,  $\mu$ 0], {t, tstart,
   tend}, {M, 0.}, numberofsteps];
30 BHCurve = Table[0, {i, numberofsteps}, {j,
   2}];
31 Ha = RK4[Hmax  $\omega$  Cos[ $\omega$  t], {t, tstart,
   tend}, {M, 0.}, numberofsteps];
32 Do[BHCurve[[i, 2]] =  $\mu$ 0 (Ha[[i, 2]] +
   ExtendedJAModelSolved[[i, 2]]), {i,
   numberofsteps}];
33 Do[BHCurve[[i, 1]] = Ha[[i, 2]], {i,
   numberofsteps}];
34 Print[ListPlot[BHCurve, Joined -> True,
   ImageSize -> Large, Frame -> True,
   FrameLabel -> {"applied magnetic field H
   in A/m", "flux density B in T"},
   GridLines -> Automatic, GridLinesStyle
   -> Directive[Dashed]]]

```

The following code exemplifies the use of ExtendedJAModel. Note that these simulations are sensible to the user provided values, such that it may not be easy at all to find the right ones.

```

36 ExtendedJAModel[t, M, 0.0001, 1.25, 1000.,
   1.2*10^6, 1100., 0.00306, 1.2 10^(-3),
   0.0889, N[4  $\pi$  10^(-7)], 10000., N[2  $\pi$ ]];

```